(12) INTERNATIONAL APPLICATION PUBLISHED UNDER THE PATENT COOPERATION TREATY (PCT)

(19) World Intellectual Property Organization
International Bureau

(43) International Publication Date
19 December 2019 (19.12.2019)

WIPO | PCT

(10) International Publication Number
WO 2019/241126 A1

(51) International Patent Classification:
G01N 21/33 (2006.01)

(21) International Application Number:
PCT/US2019/036335

(22) International Filing Date:
10 June 2019 (10.06.2019)

(25) Filing Language: English

(26) Publication Language: English

(30) Priority Data:
62/683,290 11 June 2018 (11.06.2018) US

(71) Applicant: **N5 SENSORS, INC.** [US/US]; 9610 Medical Center Dr., #200, Rockville, Maryland 20850 (US).

(72) Inventors: **DEBNATH, Ratan**; 9610 Medical Center Dr., #200, Rockville, Maryland 20850 (US). **THOMSON, Brian**; 9610 Medical Center Dr., #200, Rockville, Maryland 20850 (US). **MOTAYED, Abhishek**; 5800 Inman Park Circle, #200, Rockville, Maryland 20852 (US). **DIAGNE, Ibrahima**; 9610 Medical Center Dr., #200, Rockville, Maryland 20850 (US).

(74) Agent: **DUBOIS, Steven**; Patent Portfolio Builders, PLLC, P.O. Box 7999, Fredericksburg, Virginia 22404 (US).

(81) Designated States *(unless otherwise indicated, for every kind of national protection available)*: AE, AG, AL, AM, AO, AT, AU, AZ, BA, BB, BG, BH, BN, BR, BW, BY, BZ, CA, CH, CL, CN, CO, CR, CU, CZ, DE, DJ, DK, DM, DO, DZ, EC, EE, EG, ES, FI, GB, GD, GE, GH, GM, GT, HN, HR, HU, ID, IL, IN, IR, IS, JO, JP, KE, KG, KH, KN, KP, KR, KW, KZ, LA, LC, LK, LR, LS, LU, LY, MA, MD, ME, MG, MK, MN, MW, MX, MY, MZ, NA, NG, NI, NO, NZ, OM, PA, PE, PG, PH, PL, PT, QA, RO, RS, RU, RW, SA, SC, SD, SE, SG, SK, SL, SM, ST, SV, SY, TH, TJ, TM, TN, TR, TT, TZ, UA, UG, US, UZ, VC, VN, ZA, ZM, ZW.

(84) Designated States *(unless otherwise indicated, for every kind of regional protection available)*: ARIPO (BW, GH, GM, KE, LR, LS, MW, MZ, NA, RW, SD, SL, ST, SZ, TZ, UG, ZM, ZW), Eurasian (AM, AZ, BY, KG, KZ, RU, TJ, TM), European (AL, AT, BE, BG, CH, CY, CZ, DE, DK, EE, ES, FI, FR, GB, GR, HR, HU, IE, IS, IT, LT, LU, LV, MC, MK, MT, NL, NO, PL, PT, RO, RS, SE, SI, SK, SM, TR), OAPI (BF, BJ, CF, CG, CI, CM, GA, GN, GQ, GW, KM, ML, MR, NE, SN, TD, TG).

(54) Title: CARBON DIOXIDE SENSING DEVICE AND METHOD HAVING AN ARRAY OF SENSORS ON A SINGLE CHIP

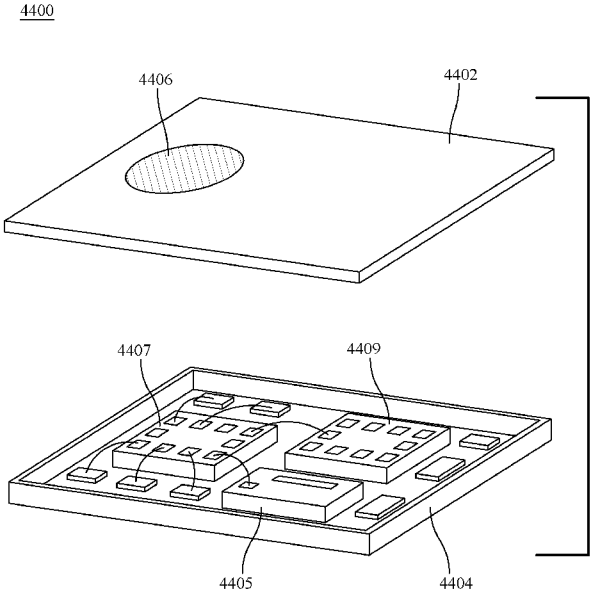


Figure 44

(57) Abstract: A carbon dioxide sensor package includes a housing having an opening. A filter membrane is mounted in the opening of the housing. A sensor is disposed within a cavity in the housing, the cavity being disposed beneath the opening, wherein the sensor is configured with first particles functionalizing an outer surface thereof to adsorb a target analyte in a presence of light, wherein the target analyte is carbon dioxide, and further configured to output data associated with a concentration of carbon dioxide sensed by the sensor. The package also includes an application specific integrated circuit disposed within the housing and configured to process data from the sensor and output processed data associated with the concentration of carbon dioxide. A light source is also disposed within the housing and configured to generate the light.

WO 2019/241126 A1

[Continued on next page]

Published:

— *with international search report (Art. 21(3))*

— *before the expiration of the time limit for amending the claims and to be republished in the event of receipt of amendments (Rule 48.2(h))*

CARBON DIOXIDE SENSING DEVICE AND METHOD HAVING AN ARRAY OF SENSORS ON A SINGLE CHIP

RELATED APPLICATION

[0001] This application relates to, and claims the benefit of priority of, U.S. Provisional Patent Application No. 62/683,290, filed on June 11, 2018, entitled "CARBON DIOXIDE SENSING DEVICE AND METHOD HAVING AN ARRAY OF SENSORS ON A SINGLE CHIP" to Debnath et al., the disclosure of which is incorporated here by reference.

TECHNICAL FIELD

[0002] The present invention relates to a carbon dioxide sensing device including a semiconductor nanostructure and at least one of metal or metal-oxide nanoparticles functionalizing the nanostructure and forming a hybrid sensor that enables light-assisted sensing of carbon dioxide.

BACKGROUND

[0003] Detection of chemical species in air, such as industrial pollutants, poisonous gases, chemical fumes, and volatile organic compounds (VOCs), is vital for the health and safety of communities around the world (see Watson J and Ihokura K (1999) *Special issue on Gas-Sensing Materials*, Mater. Res. Soc. Bull. 24:14). The development of reliable, portable gas sensors that can detect harmful gases in real-time with high sensitivity and selectivity is therefore extremely important (Wilson D M *et al.* (2001) "*Chemical Sensors for Portable, Handheld Field Instruments*," IEEE Sensors Journal 1:256-274; Eranna G *et al.* (2004) "*Oxide Materials for Development of Integrated Gas Sensors--A Comprehensive Review/Integrated Gas Sensors--A Comprehensive Review*," Critical Reviews in Solid State and Material Sciences 29:111-188).

[0004] Due to their small size, ease of deployment, and low-power operation, solid-state thin film sensors are favored over analytical techniques such as optical and mass spectroscopy, and gas chromatography for real-time environmental monitoring (Wilson D M *et al.* (2001), *supra*, IEEE Sensor Journal 1:256-274; Shimizu Y and Egashira M (1999)

"*Basic aspects and Challenges of Semiconductor Gas Sensors*," Mater. Res. Soc. Bull. 24:18; Sze S M (1994) Semiconductor Sensors 1st ed, Willey; New York). Selectivity, which is a sensor's ability to discriminate between the components of a gas mixture and provide detection signal for the component of interest, is an important consideration for the sensor's real-life applicability. Conventional metal-oxide based thin film sensors, despite decades of research and development (Brattain J B W H (1952) "*Surface properties of germanium*," Bell. Syst. Tech. Journal 32:1; Azad A M *et al.* (1992) "*Solid-State Sensors: A Review*," J. Electrochem. Soc. 139(12):3690-3704), still lack selectivity for different species and typically require high working temperatures (Meixner H and Lampe U (1996) "*Metal oxide sensors*," Sens. and Actuators B 33:198-202; Nicoletti S *et al.* (2003) "*Use of Different Sensing Materials and Deposition Techniques for Thin-Film Sensors to Increase Sensitivity and Selectivity*," IEEE Sensors Journal 3:454-459; Demarne V and Sanjines R (1992) Gas Sensors-Principles, Operation and Developments ed. G. Sberveglieri, Kluwer Academic, Netherlands). As such, the usability of such conventional sensors is severely limited and poses long-term reliability problems.

[0005] For a chemical sensor, the active surface area is an important factor for determining its detection limits or sensitivity. It is known that the electrical properties of nanowires (NWs) change significantly in response to their environments due to their high surface to volume ratio (Cui Y *et al.* (2001), *supra*, Science 293:1289-1292; Zhang D *et al.* (2004) "*Detection of NO_2 down to ppb levels using individual and multiple In_2O_3 nanowire devices*," Nano. Lett. 4:1919-1924; Kong J *et al.* (2000) "*Nanotube Molecular Wires as Chemical Sensors*," Science 287:622-625; Comini E *et al.* (2002) "*Stable and highly sensitive gas sensors based on semiconducting oxide nanobelts*," Appl. Phys. Lett. 81:1869). NWs are therefore well suited for direct measurement of changes in their electrical properties (*e.g.* conductance/resistance, impedance) when exposed to various analytes. Substantial research has demonstrated the enhanced sensitivity, reactivity, and catalytic efficiency of the nanoscale structures (Cui Y *et al.* (2001), *supra*, Science 293:1289; Li C *et al.* (2003) "*In_2O_3 nanowires as chemical sensors*," Appl. Phys. Lett. 8:1613; Wan Q *et al.* (2004) "*Fabrication and ethanol sensing characteristics of ZnO nanowire gas sensors*," Appl. Phys. Lett. 84:3654; Wang C *et al.* (2005) "*Detection of H_2S down to ppb levels at room temperature using sensors based on ZnO nanorods*," Sens. and Actuators B 113:320-323; Wang H T *et al.* (2005) "*Hydrogen-selective sensing at room*

temperature with ZnO nanorods," Appl. Phys. Lett. 86:243503; Raible I *et al.* (2005) "*V_2O_5 nanofibers: novel gas sensors with extremely high sensitivity and selectivity to amines*," Sens. and Actuators B 106:730-735; McAlpine M C *et al.* (2007) "*Highly ordered nanowire arrays on plastic substrates for ultrasensitive flexible chemical sensors*," Nat Mater 6:379-384).

[0006] There have been attempts to demonstrate sensors based on nanotube/nanowire decorated with nanoparticles of metal and metal-oxides. For example, Leghrib *et al.* reported gas sensors based on multiwall carbon nanotubes (CNTs) decorated with tin-oxide (SnO_2) nanoclusters for detection of NO and CO (see Leghrib R *et al.* (2010) "*Gas sensors based on multiwall carbon nanotubes decorated with tin oxide nanoclusters*," Sens. and Actuators B: Chemical 145:411-416). Using mixed SnO_2/TiO_2 included with CNTs, Duy *et al.* demonstrated ethanol sensing at a temperature of 250°C. (Duy N V *et al.* (2008) "*Mixed SnO_2/TiO_2 Included with Carbon Nanotubes for Gas-Sensing Application*," J. Physica E 41:258-263). Balázsi *et al.* fabricated hybrid composites of hexagonal WO_3 powder with metal decorated CNTs for sensing NO_2 (Balázsi C *et al.* (2008) "*Novel hexagonal WO_3 nanopowder with metal decorated carbon nanotubes as NO2 gas sensor*," Sensors and Actuators B: Chemical 133:151-155). Kuang *et al.* demonstrated an increase in the sensitivity of SnO_2 nanowire sensors to H_2S, CO, and CH_4 by surface functionalization with ZnO or NiO nanoparticles (Kuang Q *et al.* (2008) "*Enhancing the photon-and gas-sensing properties of a single SnO2 nanowire based nanodevice by nanoparticle surface functionalization*," J. Phys. Chem. C 112:11539-11544). ZnO NWs decorated with Pt nanoparticles were utilized by Zhang *et al.*, showing that the response of Pt nanoparticles decorated ZnO NWs to ethanol is three times higher than that of bare ZnO NWs (Zhang Y *et al.* (2010) "*Decoration of ZnO nanowires with Pt nanoparticles and their improved gas sensing and photocatalytic performance*," Nanotechnology 21:285501). Chang *et al.* showed that by adsorption of Au nanoparticles on ZnO NWs, the sensor sensitivity to CO gas could be enhanced significantly (Chang S-J *et al.* (2008) "*Highly sensitive ZnO nanowire CO sensors with the adsorption of Au nanoparticles*," Nanotechnology 19:175502). Dobrokhotov *et al.* constructed a chemical sensor from mats of GaN NWs decorated with Au nanoparticles and tested their sensitivity to N_2 and CH_4 (Dobrokhotov V *et al.* (2006) "*Principles and mechanisms of gas sensing by GaN nanowires functionalized with gold nanoparticles*," J. Appl. Phys 99:104302). GaN NWs

coated with Pd nanoparticles were employed for the detection of H_2 in N_2 at 300K by Lim *et al.* (Lim W *et al.* (2008) "*Room temperature hydrogen detection using Pd-coated GaN nanowires*," Appl. Phys. Lett. 93:072109).

[0007] Although such results demonstrate the potentials of the nanowire-nanocluster based hybrid sensors, fundamental challenges and deficiencies in such prior attempts remain. Most of the results provide for mats of nanowires. Although such mats may increase sensitivity, the complex nature of inter-wire conduction makes interpreting the results difficult. Also, room-temperature operation of such previous sensors has not been demonstrated, and the selectivity is shown for only a very limited number of chemicals. Conventional sensor devices require high operating temperatures (≥250°C) and large response times (more than 5 minutes). Indeed, such temperature-assisted sensors typically provide for an integrated heater for the device. Further, the reported sensitivities of such conventional devices were quite low even with long response times. Further, such conventional devices typically do not provide for air as the carrier gas. However, the ability of a sensor to detect chemicals in air is what ultimately determines its usability in real-life.

[0008] Thus, such demonstrations have resulted in poor selectivity of known chemical sensors, and therefore have not resulted in commercially viable gas sensors. For real-world applications, selectivity between different classes of compounds (such as between aromatic compounds and alcohols) is highly desirable. For example, the threat of terrorism and the need for homeland security call for advanced technologies to detect concealed explosives safely and efficiently. Detecting traces of explosives is challenging, however, because of the low vapor pressures of most explosives (Moore, D S (2004) "*Instrumentation for trace detection of high explosives*," Review of Scientific Instruments 75(8):2499-2512; Yinon J (2002) "*Field detection and monitoring of explosives*," TrAC Trends in Analytical Chemistry 21(4):292-301; Senesac L. and Thundat T G (2008) "*Nanosensors for trace explosive detection*," Materials Today 11(3):28-36. Moreover, the difficulty of explosive detection is aggravated by the noisy environment which masks the signal from the explosive, the potential for high false alarms, and the need to determine a threat quickly. As such, trained canine teams remain the most reliable means of detecting explosive vapors to date; however, dogs are expensive to train and tire easily.

[0009] An ideal chemical sensor would be able to distinguish between the individual analytes belonging to a particular class of compounds, *e.g.* detection of the presence of benzene or toluene in the presence of other aromatic compounds, detection of a particular explosive compound, detection of a particular alcohol, *etc.* This is extremely challenging as most semiconductor-based sensors use metal-oxides (such as SnO_2, In_2O_3, ZnO) as the active elements, which are limited due to the non-selective nature of the surface adsorption sites. The surface/adsorbate interactions of conventional sensor structures are limited and non-specific. Thus, conventional sensor devices lack the same selectivity as their bulk-counterpart devices.

[0010] U.S. Patent No. 9,476,862, the disclosure of which is incorporated here by reference and which has one or more common inventors with the present application, describes nanostructure sensor devices that address these deficiencies of conventional devices by providing a semiconductor nanostructure having an outer surface and at least one of metal or metal-oxide nanoparticle clusters functionalizing the outer surface of the nanostructure and forming a photoconductive nanostructure/nanocluster hybrid sensor enabling light-assisted sensing of a target analyte. The present application focuses on a specific application/implementation of the general type of sensor described in the '862 patent to a specific problem set--- specifically the sensing of carbon dioxide concentrations in real time to address and control, for example, ventilation issues in commercial buildings.

[0011] Currently, the requirements for minimum air change per hour (ACH) that are available for mechanical exchange of outside air in a commercial building are based on occupancy, floor area and number of occupants (International Mechanical Code, Chapter 4 or ASHRAE Standard 62.1). However, due to lack of cost-effective indoor air quality (IAQ) sensors (CO2 being the precise indicator of IAQ), building operators are forced to run HVAC systems at higher mechanical exchange rates resulting in energy wastage. Non-Dispersive Infrared sensors (NDIRs) have been mainstays for CO2 detection in the industry for a few decades now, with constant performance improvement and cost-reductions. However, there are two fundamental challenges to using NDIRs to address demand controlled ventilation (DCV) based on detected CO2 concentrations – 1) the cost associated with acquisition and installation of NDIRs and 2) NDIR calibration needs due to

drift, which also increases user intervention and maintenance cost. Both of these factors hinder the widespread adoption of the NDIR technology for DCV in commercial buildings.

[0012] Accordingly, it would be desirable to provide systems, methods and devices which address the deficiencies of, e.g., NDIR sensors used in DCV systems.

SUMMARY

[0013] According to an embodiment, a sensor package includes a housing including an opening; a filter membrane mounted in the opening of the housing; a sensor disposed within a cavity in the housing, the cavity being disposed beneath the opening, wherein the sensor is configured with first particles functionalizing an outer surface thereof to adsorb a target analyte in a presence of ultraviolet (UV) light, wherein the target analyte is carbon dioxide, and further configured to output data associated with a concentration of carbon dioxide sensed by said sensor; an application specific integrated circuit (ASIC) disposed within the housing and configured to process data from the sensor and output processed data associated with the concentration of carbon dioxide; and a UV light source disposed within the housing and configured to generate the UV light.

[0014] According to another embodiment, method for sensing carbon dioxide gas concentration includes the steps of filtering an ambient gas mixture through a filter membrane into a cavity; generating light onto a sensor disposed in said cavity; and sensing carbon dioxide in the ambient gas mixture using the sensor, wherein the sensor is configured with first particles functionalizing an outer surface thereof to adsorb a target analyte in a presence of light, wherein the target analyte is carbon dioxide, and further configured to output data associated with a concentration of carbon dioxide sensed by said sensor.

[0015] According to another embodiment, a carbon dioxide sensor includes a substrate on which oxide particles are deposited, wherein said oxide particles include one of: ZnO, In203, WO3 or Sn02 particles, and wherein said carbon dioxide sensor exhibits a response to a presence of carbon dioxide proximate the substrate.

BRIEF DESCRIPTION OF THE DRAWINGS

[0016] The patent or application file contains at least one drawing/photograph executed in color. Copies of this patent or patent application publication with color drawing(s) will be provided by the Office upon request and payment of the necessary fee.

[0017] **Figure 1, plates (a) and (b)**, are schematic representations of a GaN (Nanowire)-TiO_2 (Nanocluster) hybrid sensor according to the present invention. **Figure. 1, plate (a)** shows the sensor in the dark showing surface depletion of the GaN nanowire, and **Figure 1, plate (b)** shows the sensor under UV excitation with photodesorption of O_2 due to hole capture.

[0018] **Figure 2, plate (a)**, illustrates graphically the photoresponse of a hybrid device (diameter 300 nm) to 1000 ppm of benzene and toluene mixed in air and nitrogen. **Figure 2, plate (b)** illustrates the response of a hybrid device (diameter 500 nm) to different concentrations of water in air.

[0019] **Figure 3** is a schematic representation of depletion in the TiO_2 NC in the presence of oxygen and water, and its effect on the photogenerated charge carrier separation in GaN NW. Circles in valence band indicate holes and circles in conduction band indicate electrons.

[0020] **Figure 4** illustrates graphically the photo-response of the GaN/(TiO_2-Pt) device to 1000 μmol/mol of ethanol in air and nitrogen, and to 1000 μmol/mol of water in air. The devices did not respond to water in nitrogen. The air-gas mixture was turned on at 0 s and turned off at 100 s.

[0021] **Figure 5, plate (a)** illustrates graphically UV photo-response of the GaN/(TiO_2-Pt) hybrid device to 1000 μmol/mol (ppm) of methanol, ethanol, and water in air, and hydrogen in nitrogen. The air-gas mixture was turned on at 0 s and turned off at 100 s. **Figure 5, plate (b)** illustrates the cyclic response of the GaN/(TiO_2-Pt) hybrid device when exposed to 2500 μmol/mol (ppm) of hydrogen in nitrogen. The bias voltage for all the devices was 5 V.

[0022] **Figure 6, plate (a)** is a scanning electron microscope (SEM) image of the NW bridge structure according to the present invention. **Figure 6, plate (b)** shows ZnO nanoparticles on the facets of GaN NW. **Figure 6, plate (c)** illustrates graphically current-voltage (*I-V*) characteristics of the device before and after rapid thermal anneal (RTA). **Figure 6, plate (d)** is an x-ray diffraction (XRD) Ω--2Θ scan of a 300-nm-thick ZnO film.

[0023] **Figure 7** illustrates graphically device response to 500-μmol/mol (ppm) of methanol. The inset graph at the bottom left shows the sensitivity of two devices toward 500 μmol/mol (ppm) of each isomer of butanol (with Device 1 shown as the right bar above each isomer, and Device 2 shown as the left bar above each isomer). The inset graph at the bottom right shows the response to ethanol, acetone, benzene, and hexane. Sensitivity (S) is given by $(I_g - I_a) \times 100/I_a$, where I_g is the device current in the presence of an analyte in breathing air and I_a is the current in pure breathing air, both measured 300 s after the flow is turned on. Percentage standard deviation of the device sensitivity is 3.2% based on the five data points collected over a period of 3 days in response to the breathing air.

[0024] **Figure 8** illustrates graphically device response to different flow rates of breathing air (**plate (a)**) and nitrogen gas (**plate (b)**). The flow rates of the gas are denoted as a = 20 sccm, b = 40 sccm, c = 60 sccm, d = 80 sccm, and e = 100 sccm.

[0025] **Figure 9, plate (a)** is a schematic illustration of a nanostructured semiconductor-nanocluster hybrid gas sensor according to an embodiment of the present invention. The sensor works with low-intensity light from an LED. The emission wavelength is determined by the semiconductor and metal-oxide bandgaps. **Figure 9, plate (b)** illustrates schematically an exemplary thin-film device including a semiconductor backbone functionalized with TiO_2 on a sapphire substrate. The smoothness of the substrate and film after thermal processing is shown in **Figure 9, plates (c) and (d)**.

[0026] **Figure 10** is a schematic illustration of the mechanism of sensing using the disclosed nanocluster-functionalized semiconductor devices. The sensing is due to the effective separation of photogenerated charge carriers in the semiconductor backbone caused by surface potential modification of the backbone by the nanocluster upon adsorption of chemicals. The light produces electron-hole pairs in the semiconductor, and also surface defects on the cluster due to photo desorption of oxygen and water.

[0027] **Figure 11** illustrates schematically the epitaxial layer structure utilized in sensor device fabrication according to an embodiment of the invention.

[0028] **Figure 12** illustrates schematically sensor designs according to the present invention, including a sensor having serial architecture (**plate (a)**), and a sensor having parallel architecture (**plate (b)**).

[0029] **Figure 13** are schematic illustrations of a series architecture design of a sensor with four segments, including a top view (**plate (a)**) and a cross-section view taken along the dashed line (**plate (b)**). The sensor output is the voltage between the $+V_{sensor}$ and ground pads. The V_{cal} are the real-time calibration probes for baseline and temperature drift compensating.

[0030] **Figure 14** illustrates graphically a generic sensor calibration curve. Sensitivity S is defined as the slope of the sensor output response vs. analyte concentration plot. The sensor output may be a change in current, voltage, or resistance.

[0031] **Figure 15** is a schematic illustration of photoexcitation of both the metal-oxide cluster and the GaN backbone using 365 nm light.

[0032] **Figure 16** is a schematic illustration showing selectivity tuning using a multicomponent design of nanoclusters. As shown, the target analyte is NO_2 and the interfering chemical is CO_2.

[0033] **Figure 17** illustrates graphically depletion depth induced by Pt nanoclusters on GaN and TiO_2 (as calculated by Equation (12) below).

[0034] **Figure 18** is a schematic illustration of an integration scheme for standalone system, showing components at roughly their actual size.

[0035] **Figure 19** is a schematic illustration of a hybrid sensor fabrication process according to the present invention.

[0036] **Figure 20, plates (a-c)**, are field-emission scanning electron microscopy (FESEM) images of three different sputtered thickness of TiO_2 coatings: including 2 nm (**plate (a)**), 5 nm (**plate (b)**), and 8 nm (**plate (c)**) of TiO_2 sputtered on GaN nanowires.

[0037] **Figure 21** illustrates graphically an XRD Ω - 2Θscan of 150 nm thick TiO_2 film deposited on SiO_2/Si substrate at 300°C and annealed at 650°C for 45 s in RTA. All indices correspond to the anatase phase [PDF#84-1285].

[0038] **Figure 22** illustrates typical morphologies of a 20 nm thick TiO_2 film sputtered on n-GaN nanowires and annealed at 700°C for 30 s. **Figure 22, plate (a)** is a TEM image showing non-uniformly distributed 2 nm to 10 nm diameter individual TiO_2 particles, with some of the particles marked by white circles. **Figure 22, plate (b)** is a high-resolution transmission electron microscopy (HRTEM) image of an edge of the GaN nanowire with the sputtered TiO_2 film. The FFT pattern from the boxed area is shown in exploded view in the upper left inset, indicating 0.35 nm lattice fringes which are consistent with a (101) reflecting plane of anatase.

[0039] **Figure 23, plate (a)** is a BF-STEM image with 5nm to 10 nm TiO_2 nanoparticles barely visible near an edge of a GaN nanowire, with some of the nanoparticles marked by circles. **Figure 23, plate (b)** is an ADF-STEM image of a TiO_2-containing aggregate on the edge of a GaN nanowire. **Figure 23, plate (c)** is an X-ray spectrum of an individual 5 nm TiO_2 particle shown by circled portion 'A' in **plate (a)**. **Figure 23, plate (d)** is an EEL spectra recorded on position 1 (tip of the aggregate) and position 2 (edge of the GaN nanowire), as identified in **plate (b)**, respectively.

[0040] **Figure 24** illustrates I-V characteristics of a GaN NW two-terminal device in the dark at different stages of processing. The inset shows the nanowire device with length 5.35 μm and diameter 380 nm. The scale bar is 4 μm. The thickness of sputtered TiO_2 film was 8 nm.

[0041] **Figure 25, plate (a)** illustrates graphically the dynamic photocurrent of a bare GaN NW. **Figure 25, plate (b)** illustrates the dynamic photocurrent of a TiO_2 coated (8 nm deposit) GaN NW. The diameters of both nanowires were about 200 nm. The applied bias is 5 V in both cases.

[0042] **Figure 26** illustrates graphically the dynamic response of a single GaN-TiO_2 hybrid device to 1000 ppm of toluene. For each cycle, the gas exposure time was 100 s.

The inset shows the nanowire device with 8.0 μm length and diameter 500 nm. The scale bar is 5 μm.

[0043] **Figure 27, plate (a)** illustrates the response of a single nanowire-nanocluster hybrid sensor (inset shows nanowire with diameter 500 nm) to 1000 ppm benzene, toluene, ethylbenzene, chlorobenzene, and xylene in presence of UV excitation. **Figure 27, plate (b)** illustrates the response of a different sensor (inset shows nanowire with diameter 300 nm) to 200 ppb toluene, benzene, ethylbenzene, and xylene with UV excitation. The total flow in to the chamber was kept constant at 20 sccm. The response to air is also shown. The scale bars are 5 μm.

[0044] **Figure 28** illustrates graphically a hybrid sensor's photoresponse characteristics: **Figure 28, plate (a)** shows the characteristics of the device shown in **Figure 27, plate (a)** for 100 to 10000 ppm concentration range of toluene; **Figure 28, plate (b)** shows the characteristics of the device shown in **Figure 27, plate (b)** for 50 ppb to 1 ppm concentration range of toluene.

[0045] **Figure 29** illustrates sensitivity plots of a GaN-TiO_2 nanowire-nanocluster hybrid device (diameter 300 nm) for benzene, toluene, ethylbenzene, chlorobenzene, and xylene. The plot identifies the sensor's ability to measure wide range of concentration of the indicated chemicals.

[0046] **Figure 30** is an HRTEM image of a GaN NW with TiO_2 sputtered on them, with **plate (a)** showing the GaN NW before Pt and **plate (b)** showing after Pt deposition. Circled areas in **plate (a)** indicate partially aggregated polycrystalline TiO_2 particles on the NW surface and on the supporting carbon film. Arrows in **plate (b)** in the inset at the upper left mark Pt clusters decorating a 6 nm diameter particle of titanium. The TiO_2 particle exhibits 0.35 nm fringes corresponding to (101) lattice spacing of anatase polymorph. 2 nm to 5 nm thick amorphized surface film are indicated by black arrows.

[0047] **Figure 31** illustrate an HAADF-STEM of a GaN NW coated with TiO_2 and Pt., with **plate (a)** showing 1 nm to 5 nm bright Pt nanoparticles (shown by arrows) decorating surfaces of a polycrystalline TiO_2 island-like film and of a GaN nanowire. Medium grey aggregated TiO_2 particles (outlined by dashed line in **plate (a)**) are barely visible on a thin

carbon support near the edge of the nanowire. **Plate (b)** is a high magnification image of the supporting film near the edge of the nanowire exhibiting 0.23 nm to 0.25 nm (111) and 0.20 nm to 0.22 nm (200) fcc lattice fringes belonging to Pt nanocrystallites, with arrows indicating amorphous-like Pt clusters of 1 nm and less in diameter.

[0048] **Figure 32** illustrates I-V characteristics of the hybrid sensor device at different stages of processing. **Figure 32, plate (a)** shows GaN/(TiO_2-Pt) hybrids; **Figure 32, plate (b)** shows GaN/Pt hybrids. The inset image in **plate (b)** shows the plan-view SEM image of a typical GaN NWNC hybrid sensor. The scale bar in the inset is 4 μm.

[0049] **Figure 33** illustrates graphically depletion depth induced by Pt NCs on GaN and TiO_2 as calculated by equation 12.

[0050] **Figure 34** illustrates comparative sensing behavior of the three hybrids for 1000 μmol/mol (ppm) of analyte in air: light gray bar graphs (benzene, toluene, ethylbenzene, xylene, chlorobenzene) represent GaN/TiO_2 hybrids, patterned bar graphs (ethanol, methanol, and hydrogen) represent GaN/(TiO_2-Pt) hybrids, and white bar graph (hydrogen) represents GaN/Pt hybrids. Other chemicals which did not produce any response in any one of the hybrids are not included in the plot. The zero line is the baseline response to 20 sccm of air and N_2. For this plot the magnitude of the sensitivity is used. The error bars represent the standard deviation of the mean sensitivity values for every chemical computed for 5 devices with diameters in the range of 200 nm - 300 nm.

[0051] **Figure 35, plate (a)** illustrates graphically the photo-response of GaN/(TiO_2-Pt) hybrid device to different concentrations of methanol in air. **Figure 35, plate (b)** shows photo-response of the same device to different concentrations of hydrogen in nitrogen. The air-gas mixture was turned on at 0 s and turned off at 100 s.

[0052] **Figure 36, plate (a)** is a sensitivity plot of the GaN/(TiO_2-Pt) hybrid device to ethanol, methanol, and water in air and to hydrogen in nitrogen ambient. **Figure 36, plate (b)** shows graphically a comparison of the sensitivity of GaN/(TiO_2-Pt) and GaN/Pt devices to different concentrations of hydrogen in nitrogen.

[0053] **Figure 37** illustrates schematically an exemplary fabrication flow chart for semiconductor-nanocluster based gas sensors according to the present invention.

[0054] **Figure 38, plate (a)** is an image of large area etched nanostructures of GaN on silicon and sapphire substrate formed according to disclosed processes such as shown in **Figure 37**. **Figure 38, plate (b)** shows an image of a nanostructure of GaN on silicon and sapphire using ICP etching and post-etching surface treatment. This nanostructure forms the backbone of the disclosed sensors in disclosed embodiments.

[0055] **Figure 39** is an RTEM image of a GaN NW with TiO_2 sputtered on them. Circled portions indicate partially aggregated polycrystalline TiO_2 particles on the NW surface and on the supporting carbon film.

[0056] **Figure 40** illustrates graphically *I-V* characteristics of a GaN NW two-terminal device at different stages of processing.

[0057] **Figure 41, plate (a)** illustrates graphically response of a single, nanowire-nanocluster hybrid sensor to 100 ppb of benzene, toluene, nitrobenzene, nitrotoluene, dinitrobenzene, dinitrotoluene and trinitrotoluene in the presence of UV excitation. **Figure 41, plate (b)** shows the response of the device to different concentrations of trinitrotoluene.

[0058] **Figure 42** is a sensitivity plot of a GaN-TiO_2 nanowire-nanocluster hybrid device for benzene, toluene, nitrotoluene, nitrobenzene, DNT, DNB and TNT.

[0059] **Figure 43** illustrates sensitivity of two different nanowire-nanocluster hybrid sensors to 100 ppb of the different aromatic compounds.

[0060] **Figure 44** depicts a sensor package including a carbon dioxide sensor, an application specific integrated circuit (ASIC) and a light source according to an embodiment.

[0061] **Figure 45** depicts the relationship between the filter membrane and the C02 sensor die in the sensor package according to an embodiment.

[0062] **Figure 46** illustrates a block diagram of elements of an ASIC according to an embodiment.

[0063] **Figures 47, 48 and 49** illustrate an exemplary GANN architecture and algorithm according to embodiments.

[0064] **Figure 50** illustrates cost functions associated with the BPANN, GA and GANN algorithms.

[0065] **Figure 51** shows a typical variation of the signal drift.

[0066] **Figure 52** lists different techniques associated with drift correction.

[0067] **Figure 53** illustrates details of the CO2 sensor in the sensor package according to an embodiment.

[0068] **Figure 54** illustrates sensor performance associated with the CO2 sensor of Figure 53.

[0069] **Figure 55** is a flow diagram illustrating a method of sensing CO2 according to an embodiment.

DETAILED DESCRIPTION

[0070] The present invention is directed to sensor devices including a semiconductor nanostructure, such as a micro or nanodevice, or nanowire (NW), having a surface functionalized or decorated with metal or metal-oxide nanoparticles or nanoclusters. When metal/metal-oxide nanoparticles selected according to the disclosed methods are placed on the surface of a nanostructure, significant changes result in the physical properties of the system. The nanoparticles increase the adsorption of chemical species by introducing additional adsorption sites, thereby increasing the sensitivity of the resulting system.

[0071] The metal or metal-oxide nanoparticles may be selected to act as catalysts designed to lower the activation energy of a specific reaction, which produces active radicals by dissociating the adsorbed species. These radicals can then *spill-over* to a semiconductor structure (see Sermon P A and Bond G C (1973) "*Hydrogen Spillover*," Catal. Rev. 8(2):211-239; Conner W C *et al.* (1986) "*Spillover of sorbed species*," Adv. Catal. 34:1), where they are more effective in charge carrier transfer. Further, the selected nanoparticles modulate the current through the nanowire through formation of nanosized depletion regions, which is in turn a function of the adsorption on the nanoparticles. Nanoparticles or nanoclusters suitable for the present invention include virtually any metal-oxide and/or metal. Thus, it should be understood that the present invention is not limited to

the particular exemplary metal-oxides and/or metals disclosed in the various embodiments and examples herein.

[0072] According to one embodiment, nanowire-nanocluster hybrid chemical sensors were realized by functionalizing *n*-type (Si doped) gallium nitride (GaN) NWs with TiO_2 nanoclusters. The sensors selectively sense benzene and related aromatic environmental pollutants, such as toluene, ethylbenzene, and xylene (sometimes referred to as BTEX). GaN is a wide-bandgap semiconductor (3.4 eV), with unique properties (Morkoç H (1999) *Nitride Semiconductors and Devices*, Springer series in Materials Science, Vol. 32, Springer, Berlin). Its chemical inertness and capability of operating in extreme environments (high-temperatures, presence of radiation, extreme pH levels) is thus suitable for the disclosed sensor design. TiO_2 is a photocatalytic semiconductor with a bandgap energy of 3.2 eV (anatase phase). Photocatalytic oxidation of various organic contaminants over titanium dioxide (TiO_2) has been previously studied (see Mills A and Hunte S L (1997) "*An overview of of semiconductor photocatalysis*," J. Photochem. Photobiol. A 108:1-35; Luo Y and Ollis D F (1996) "*Heterogeneous photocatalytic oxidation of trichloroethylene and toluene mixtures in air: Kinetic promotion and inhibition, time-dependent catalyst activity*," J. Catal. 163:1-11). The TiO_2 nanoclusters were thus selected to act as nanocatalysts to increase the sensitivity, lower the detection time, and enable the selectivity of the structures to be tailored to organic analytes.

[0073] The hybrid sensor devices may be developed by fabricating two-terminal devices using individual GaN NWs followed by the deposition of TiO_2 nanoclusters using radio frequency (RF) magnetron sputtering. The sensor fabrication process employed standard micro-fabrication techniques. X-ray diffraction (XRD) and high-resolution analytical transmission electron microscopy using energy-dispersive X-ray and electron energy-loss spectroscopies confirmed the presence of anatase phase in TiO_2 clusters after post-deposition anneal at 700°C.

[0074] A change of current was observed for these hybrid sensors when exposed to the vapors of aromatic compounds (*e.g.*, benzene, toluene, ethylbenzene, xylene, and chlorobenzene mixed with air) under UV excitation, while they had minimal or no response to non-aromatic organic compounds such as methanol, ethanol, isopropanol, chloroform,

acetone, and 1, 3-hexadiene. The sensitivity range for the noted aromatic compounds, except chlorobenzene, were from about 1% down to about 50 parts per billion (ppb) at room-temperature. By combining the enhanced catalytic properties of the TiO_2 nanoclusters with the sensitive transduction capability of the nanowires, an ultra-sensitive and selective chemical sensing architecture is achieved.

[0075] As discussed in further detail in Example 1 below, GaN-TiO_2 (nanowire-nanocluster) hybrid sensors demonstrated a response to specific volatile organic compounds mixed with air at ambient temperature and humidity. In the presence of UV light (*e.g.*, having a wavelength in the range of about 10 nm to about 400 nm), these hybrid sensor devices exhibited change in the photocurrent when exposed to benzene, toluene, ethylbenzene, xylene, and chlorobenzene mixed in air. However, gases like methanol, ethanol, isopropanol, chloroform, acetone, and 1, 3-hexadiene exhibited little or no change in the electrical characteristics of the devices, thus demonstrating the selective response of these sensors to the aromatic compounds. Benzene, toluene, ethylbenzene, and xylene were detected by the disclosed sensors at a concentration level as low as 50 ppb in air. In addition, the disclosed sensor devices are highly stable and able to sense aromatic compounds in air reliably for a wide range of concentrations (*e.g.*, 50 ppb to 1%).

[0076] In addition, the disclosed sensors demonstrated highly sensitive and selective detection of traces of nitro-aromatic explosive compounds. As discussed in further detail in Example 5 below, GaN/TiO_2 nanowire-nanocluster hybrid sensors detected different aromatic and nitroaromatic compounds at room temperature. For example, the GaN/TiO_2 hybrids were able to detect trinitrotoluene (TNT) concentrations as low as 500 pmol/mol (ppt) in air and dinitrobenzene concentrations as low as 10 nmol/mol (ppb) in air in approximately 30 seconds. The noted sensitivity range of the devices for TNT was from 8 ppm down to as low as 500 ppt. The detection limit of dinitrotoluene, nitrobenzene, nitrotoluene, toluene and benzene in air is about 100 ppb with a response time of $\cong$75 seconds. Devices according to the present invention exhibited sensitive and selective response to TNT when compared to interfering compounds like toluene. Thus, the disclosed sensors are suitable for use as highly sensitive, selective, low-power and smart explosive detectors, which are relatively inexpensive to manufacture in larger quantities.

[0077] Based on structural analysis, an exemplary mechanism that qualitatively explains the hybrid sensor's response to different analytes is shown in **Figure 1**. With regard to the photocatalytic processes on the TiO_2 surface, the oxygen vacancy defects (Ti^{3+} sites) on the surface of TiO_2 are the active sites responsible for adsorption of species like oxygen, water, and organic molecules (see Yates Jr J T (2009) "*Photochemistry on TiO2: mechanisms behind the surface chemistry*," Surf. Sci. 603:1605-1612). Interestingly, a relatively defect free TiO_2 surface, generated by annealing in high-oxygen flux, is chemically inactive (Li M *et al.* (1999) "*Oxygen-induced restructuring of rutile TiO_2(110): formation mechanism, atomic models, and influence on surface chemistry*," Faraday Discuss. 114:245). Experimental studies and simulations reveal that molecular oxygen is chemisorbed on the surface vacancies (Ti^{3+} sites), acquiring a negative charge as shown in **Figure 1, plate (a)** (Anpo M *et al.* (1999) "*Generation of superoxide ions at oxide surfaces*," Top. Catal. 8:189-198; de Lara-Castells M P and Krause J L (2003) "*Theoretical study of the UV-induced desorption of molecular oxygen from the reduced TiO_2 (110) surface*," J. Chem. Phys. 118:5098). This is due to the presence of the localized electron density at or near exposed Ti^{3+} atoms on the TiO_2 surface (Henderson M A *et al.* (1999) "*Interaction of Molecular Oxygen with the Vacuum-Annealed TiO2(110) Surface: Molecular and Dissociative Channels*," J. Phys. Chem. B 103:5328-5337). Water may also be present on the TiO_2 cluster surface via molecular or dissociative adsorption, producing OH^- species on the defect sites (Lee F K *et al.* (2007) "*Role of water adsorption in photoinduced superhydrophilicity on TiO_2 thin films*," Appl. Phys. Lett. 90:181928; Bikondoa O *et al.* (2006) "*Direct visualization of defect-mediated dissociation of water on TiO_2 (110)*," Nat. Mater. 5:189-192).

[0078] Although most of the theoretical and experimental studies on oxygen and water adsorption are done for the (110) surface of rutile phase, there are studies that suggest that similar adsorption behavior is also expected for the anatase surface (Wahab H S *et al.* (2008) "*Computational investigation of water and oxygen adsorption on the anatase TiO_2 (100) surface*," J. Mol. Chem. Struct. 868:101-108). The GaN NW has a surface depletion region as shown in **Figure 1, plate (a)**, which determines its dark conductivity (Sanford N A *et al.* (2010) "*Steady-state and transient photoconductivity in c-axis GaN nanowires grown by nitrogen-plasma-assisted molecular beam epitaxy*," J. Appl. Phy. 107:034318).

[0079] In the presence of UV excitation with an energy above the bandgap energy of anatase TiO_2 (3.2 eV) and GaN (3.4 eV), electron-hole pairs are generated both in the GaN NW and in the TiO_2 cluster, as shown in Figure 1, plate (b). Photogenerated holes in the nanowire tend to diffuse towards the surface due to the surface band bending. This effect of separation of photogenerated charge carriers results in a longer lifetime of photogenerated electrons, which in turn enhances the photoresponse of the nanowire devices. On the TiO_2 cluster surface, however, the photogenerated charge carriers lead to a different phenomenon. In *n*-type semiconductor oxides such as TiO_2, the surface adsorption produces upward band-bending, which drives the photogenerated holes towards the surface. The chemisorbed oxygen molecule (O_2^-) and hydroxide ions (OH^-) can readily capture a hole and desorb as shown in **Figure 1, plate (b)** (Perkins C L and Henderson M A (2001) "*Photodesorption and Trapping of Molecular Oxygen at the TiO_2(110)--Water Ice Interface*," J. Phys. Chem. B. 105:3856-3863; Thompson T L and Yates J T Jr. (2006) "*Control of a surface photochemical process by fractal electron transport across the surface: O(2) photodesorption from TiO(2)(110)*," J. Phys. Chem. B 110:7431-7435). The decrease of photocurrent through these hybrid sensors when exposed to 20 sscm of air may be due to the increase in oxygen concentration at the surface of TiO_2 clusters, leading to an increase in trapping of photogenerated holes at the surface. This process results in increased lifetime of photogenerated electrons. As these nanowires are *n*-type, excess negative charge on the surface of the wire (on the TiO_2 clusters) reduces the nanowire current, thus providing a local-gating effect due to net negative charge accumulation in the TiO_2 clusters. Thus, the photoinduced oxygen desorption and subsequent capture of holes by organic adsorbate molecules on the surface of TiO_2 clusters produces the local-gating effect, which is responsible for the sensing action of the disclosed sensor devices. The adsorbed hydroxyl ions may also trap a hole forming $OH^{\cdot}$ species. Other effects such as diffusion of carriers between the clusters and the nanowire may also have a role in the sensing properties of the sensors.

[0080] Although some embodiments are described in term of excitation in the presence of UV light, it should be understood that excitation by radiation of other wavelengths may be more suitable for devices having other types of metal-oxide and/or metal nanoparticles. For example, excitation in the presence of visible light (*i.e.*, having a wavelength of between about 380nm and about 740 nm) is suitable for some embodiments.

[0081] The process noted above and shown in **Figure 1** also explains sensor response when exposed to N_2 flow, as shown in **Figure 2, plate (a)**. In the presence of 20 sccm of N_2 flow, the photocurrent in the sensors increases significantly in comparison with 20 sccm of air flow. In an N_2 environment, oxygen is desorbed from the surface vacancy sites by capturing photogenerated holes, but does not get re-adsorbed, resulting in significant reduction of hole capture. As such, the photogenerated electron-hole pairs recombine effectively in the cluster. Thus, the photocurrent through the nanowire/nanocluster hybrid sensor, which is otherwise increased due to the local-gating effect by the TiO_2 clusters, is absent in an N_2 environment.

[0082] In the presence of water in air, the photocurrent through these sensors recovers towards the level without air flow, as seen in **Figure 2, plate (b)**, indicating a reduction of the hole trapping due to adsorption of water on the TiO_2 surface. Water may be adsorbed as a molecule on the defect sites replacing O_2 (see Herman G S *et al.* (2003) "*Experimental Investigation of the Interaction of Water and Methanol with Anatase-TiO_2(101)*," J. Phys. Chem. B 107:2788-2795). With increasing water concentration, more defects are filled with water. If the adsorbed water dissociates and produces OH^- species, then it is possible that it will act as hole traps and decrease the photocurrent the same way the photodesorption of oxygen does. A competition between the molecular water adsorption (reducing hole capture) and dissociative water adsorption (increasing hole capture) is possible, with the dominant process ultimately determining the photocurrent level in the nanowires in the presence of water.

[0083] The presence of aromatic compounds such as benzene, ethylbenzene, chlorobenzene, and xylene in air reduced the photocurrent (e.g. see **Figure 2, plate (a)**). Organic molecules are known hole-trapping adsorbates (see Yamakata A *et al.* (2002) "*Electron-and hole-capture reactions on Pt/TiO_2 photocatalyst exposed to methanol vapor studied with time-resolved infrared absorption spectroscopy*," J. Phys. Chem. B 106:9122-9125). Most aromatic compounds show high affinity for electrophilic aromatic substitution. The exact mechanism of photooxidation of adsorbed organic compounds on TiO_2 is complex. However, it is believed that oxidation occurs by either indirect oxidation via the surface-bound hydroxyl radical (*i.e.*, a trapped hole at the TiO_2 surface) or directly via the valence-band hole before it is trapped either within the particle or at the particle surface

(see Nosaka Y *et al.* (1998) "*Factors governing the initial process of TiO2 photocatalysis studied by means of in situ electron spin resonance measurements*," J. Phys. Chem. B 102:10279-10283; Mao Y *et al.* (1991) "*Identification of organic acids and other intermediates in oxidative degradation of chlorinated ethanes on titania surfaces en route to mineralization: a combined photocatalytic and radiation chemical study*," J. Phys. Chem. 95:10080-10089). In the presence of air (with residual water) hydroxyl mediated hole transfer to adsorbates such as benzene, xylene is dominant, whereas in the N_2 environment direct transfer of valence band holes to aromatic adsorbates could be possible.

[0084] Irrespective of the hole transfer mechanism, the presence of additional hole traps reduces the sensor photocurrent, as observed in the presence of benzene mixed with N_2 and air as shown in **Figure 2, plate (a)**. The model disclosed herein qualitatively explains the observed trends for compounds tested, such as benzene, ethylbenzene, chlorobenzene, and xylene. However, toluene exhibits a different trend, which may be due to other second order effects other than or in addition to the hole trapping mechanism.

[0085] The disclosed mechanism is further validated when comparing ionization energies of various compounds tested with the responses generated when the sensors are exposed to them (see **Table I**). The effectiveness of the process of hole transfer to the adsorbed organic molecules relates to the compound's ability to donate an electron (*i.e.* the lower the ionization energy of a compound, the easier for it to donate an electron or capture a hole). The observed sensitivity trend for benzene (lowest sensitivity), ethylbenzene, and xylene (highest sensitivity) correlates with their ionization energies as shown in **Table I**, with benzene being the highest and xylene the lowest among the three.

Table I: Physical Properties of Various Compounds Tested

Organic Compound	Sensitivity	Ionization Potential (eV)
Chloroform	No	11.37
Ethanol	No	10.62
Isopropanol	No	10.16
Cyclohexane	Yes	9.98
Acetone	No	9.69
Benzene	Yes (Min)	9.25
Chlorobenzene	Yes	9.07
Toluene	Yes	8.82
Ethylbenzene	Yes	8.77
Xylene	Yes (Max)	8.52
1,3-Hexadiene	No	8.50

[0086] As shown in **Table I**, the sensitivity trend is consistent for aromatics, given 1,3-Hexadiene produced no response in the sensors. Although most functional groups with either a non-bonded lone pair or p-conjugation show oxidative reactivity towards TiO_2 (Hoffman M R *et al.* (1995) "*Environmental Applications of Semiconductor Photocatalysis*," Chem. Rev. 95:69-96), aromatic compounds are more easily photocatalyzed than aliphatic ones under the same conditions (Carp O *et al.* (2004) "*Photoinduced reactivity of titanium dioxide*," Prog. Solid St. Chem. 32:33-177).

[0087] Thus, the metal-oxide nanoclusters (TiO_2) on GaN NWs or nanostructures demonstrate the disclosed architecture for highly selective gas sensing. The exemplary sensors are capable of selectively sensing benzene and related aromatic compounds at nmol/mol (ppb) level in air at room-temperature under UV excitation.

[0088] According to another embodiment, the specific selectivity of the disclosed nanowire (or nanostructure)/nanocluster hybrid sensors may be tailored using a multi-component nanocluster design. For example, catalytic metals (*e.g.*, platinum (Pt), palladium (Pd), and/or any other transition metals) are deposited onto the surface of oxide photocatalysts in order to enhance their catalytic activity. Metal clusters on a metal-oxide catalyst alter the behavior of the metal-oxide catalyst by any one, or a combination of, the

following mechanisms: 1) changing the surface adsorption behavior as metals often have very different heat of adsorption values compared to the metal-oxides; 2) enabling catalytic decomposition of certain analytes on the metal surface, which otherwise would not be possible on the oxide surface; 3) transporting active species to the metal-oxide support by the spill-over effect from the metal cluster; 4) generating a higher degree of interface states, thus increasing reactive surface area reaction area; 5) changing the local electron properties of the metal clusters, such as workfunction, due to adsorption of gases; and 6) effectively separating photogenerated carriers in the underlying metal-oxide. The effect of transition metal loading such as iron (Fe), copper (Cu), Pt, Pd, and rhodium (Rh) onto TiO_2 has been evaluated for photocatalytic decomposition of various chemicals in both gas-solid and liquid-solid regimes.

[0089] In one implementation, the selectivity of the titanium dioxide (TiO_2) nanocluster-coated gallium nitride (GaN) nanostructure sensor device is altered by addition of platinum (Pt) nanoclusters. In another implementation, the sensor device includes Pt nanocluster-coated GaN nanostructure. The hybrid sensor devices may be developed by fabricating two-terminal devices using individual GaN NWs or nanostructures followed by the deposition of TiO_2 and/or Pt nanoclusters (NCs) using a sputtering technique, as described above.

[0090] The sensing characteristics of GaN/(TiO_2-Pt) nanowire-nanocluster (NWNC) hybrids and GaN/(Pt) NWNC hybrids is altered as compared to GaN/TiO_2 sensors. The GaN/TiO_2 NWNC hybrids show remarkable selectivity to benzene and related aromatic compounds with no measurable response for other analytes, as discussed above. However, the addition of Pt NCs to GaN/TiO_2 sensors dramatically alters the sensing behavior, making them sensitive only to methanol, ethanol, and hydrogen, but not to other chemicals tested, as discussed in further detail in Example 2 below.

[0091] The GaN/(TiO_2-Pt) hybrid sensors were able to detect ethanol and methanol concentrations of 100 nmol/mol (ppb) in air in approximately 100 seconds, and hydrogen concentrations from 1 μmol/mol (ppm) to 1% in nitrogen in less than 60 seconds. However, GaN/Pt hybrid sensors showed limited sensitivity only towards hydrogen and not towards any alcohols. All the hybrid sensors are operable at room temperature and are

photomodulated (*i.e.*, responding to analytes only in the presence of light, *e.g.*, ultra violet (UV) light). The selectivity achieved is significant from the standpoint of numerous applications requiring room-temperature sensing, such as hydrogen sensing and sensitive alcohol monitoring. The disclosed sensors therefore demonstrate tremendous potential for tailoring the selectivity of the hybrid nanosensors for a multitude of environmental and industrial sensing applications.

[0092] A qualitative understanding of the selective sensing mechanism of the disclosed sensors may be developed by considering how different molecules adsorb on the nanocluster surfaces, and determining the roles of intermediate reactions in the sensitivity of the sensors. While some of the embodiments, examples and explanation describe the invention in terms of NWs, it should be understood that other nanostructures or microstructures may be utilized. Accordingly, the present invention is not limited to sensors including NWs.

[0093] *The photocurrent in GaN/(TiO_2-Pt) hybrid sensors in the presence of air, nitrogen, and water:*

[0094] The oxygen vacancy defects (Ti^{3+} sites) on the surface of TiO_2 are the "active sites" for the adsorption of species like oxygen, water, and organic molecules (Yates Jr J T (2009) "*Photochemistry on TiO2: mechanisms behind the surface chemistry*," Surf. Sci. 603:1605-1612; Bikondoa O *et al.* (2006) "*Direct visualization of defect-mediated dissociation of water on TiO_2(110)*," Nat. Mater. 5:189-192). It has been observed that oxygen adsorption on photocatalyst powders such as TiO_2 and ZnO quenches the photoluminescence (PL) intensity, while adsorption of water produces an enhancement of the PL. Electron-trapping adsorbates, such as oxygen, increase the band-bending of TiO_2, which facilitates the separation of photogenerated electron hole pairs in the oxide. Subsequently, the PL intensity is decreased as the photogenerated charge carries cannot recombine efficiently. Conversely, in the case of water, the band bending is reduced, resulting in an increase in the PL intensity. In explaining the observed behavior of the hybrid sensors, the depletion effect induced by the TiO_2 clusters on GaN NW is considered. Considering an inverse relationship, *i.e.*, increase in depletion of the TiO_2 cluster leads to a

decrease in the depletion width in the GaN NW and vice versa, some of the observed sensing behavior is explained.

[0095] As shown in **Figure 3**, when oxygen is adsorbed on the TiO_2 NC surface, the depletion width in the NC increases, leading to a decrease in the depletion width in the NW. Adsorption of water, nitrogen, and alcohol produce the reverse effect: they decrease the depletion width of the TiO_2 NC, leading to an increase in the band-bending on the GaN NW. Increased band-bending in the GaN NW results in an effective separation of charge carriers, leading to an increase in photocurrent through the NW. This qualitatively explains the increase in the photocurrent when the hybrid sensor is exposed to water mixed with air or with pure nitrogen (see **Figure 4**). However, the increase in the photocurrent when exposed to 20 sccm of air flow is not fully explained. Under air flow, more oxygen should adsorb on the NCs, causing an increase in the depletion width of the cluster. This should have resulted in a decrease in the photocurrent based on our assumption; however, an increase in the photocurrent is exhibited (**Figure 4**) when 20 sccm of air is passed through the chamber.

[0096] In the absence of UV light, the absorption or desorption of chemicals from the cluster surfaces cannot modulate the dark current through the nanowire. In the dark, the surface depletion layer of the GaN NW is thicker compared to under UV excitation (see Mansfield L M *et al.* (2009) "*GaN nanowire carrier concentration calculated from light and dark resistance measurements*," Journal of Electronic Materials 38:495-504). The minority carrier (hole) concentration is also significantly lower. Thus the NCs are ineffective in modulating the dark current through the NW.

[0097] *Mechanism of sensing of alcohols and hydrogen by GaN/(TiO_2-Pt) NWNC sensors*

[0098] Adsorption of alcohols (RCH_2-OH) on the TiO_2 surface leads to their oxidation (Kim K S and Barteau M A (1989) "*Reaction of Methanol on TiO_2*," Surface Science 223:13-32). Although there are various mechanisms of oxidation of adsorbed alcohols on TiO_2 surface, focus is on the oxidation of alcohols by photogenerated holes. The process is described by the following reactions:

$$RCH_2\text{-}OH\ (g) \rightleftharpoons RCH_2\text{-}OH\ (ads) \qquad \text{(Equation 1)}$$

$$RCH_2\text{-}OH(ads) + h^+\ (\text{photogenerated hole}) \rightleftharpoons RCH_2\text{-}OH^+(ads) \qquad \text{(Equation 2)}$$

$$RCH_2\text{-}OH^+(ads) \rightleftharpoons RCH\text{-}OH^*(ads) + H^+(ads) \qquad \text{(Equation 3)}$$

$$RCH\text{-}OH^*(ads) \rightleftharpoons RCHO(ads) + H^+(ads) + e^- \qquad \text{(Equation 4)}$$

where (ads) and (g) represent adsorbed and gas phase species, respectively. For Equation 4 to proceed in the forward directions, the H^+ species should be removed effectively. It is possible that from TiO_2 NCs the H^+ species can spill-over on to Pt clusters nearby, where they can be reduced to form H_2:

$$2\,H^+(ads) + 2\,e^- \rightleftharpoons H_2\ (g) \qquad \text{(Equation 5)}$$

[0099] As H^+ reduction and hydrogen-hydrogen recombination is weak on the bare TiO_2 surface (Fujishima A *et al.* (2008) "*TiO_2 photocatalysis and related surface phenomena*," Surf. Sci. Rep. 63:515-582), the rate of alcohol oxidation to aldehyde might be affected by the H^+ reduction and hydrogen-hydrogen recombination on the Pt NCs. Adsorption of alcohols and their subsequent oxidation due to trapping of photogenerated holes leads to a decrease in the band bending of TiO_2 NCs. As shown in **Figure 3**, this leads to an increase in the NW photocurrent, which is observed for the GaN/(TiO_2-Pt) sensors when exposed to methanol and ethanol (**Figure 4**). It is likely that the production of H.sub.2 on Pt is the key for sensing alcohols by GaN/(TiO_2-Pt) sensors. Additionally, H_2 on Pt surface can dissociate and diffuse to the Pt/TiO_2 interface. Atomic hydrogen is shown to produce an interface dipole layer, which reduces the effective work-function of Pt (Du X *et al.* (2002) "*A New Highly Selective H2 Sensor Based on TiO2/PtO-Pt Dual-Layer Films*," Chem. Mater. 14:3953-3957). Effective reduction of Pt workfunction also reduces the depletion width in TiO_2, which according to the model in **Figure 4**, also leads to an increase in the photocurrent when these sensors are exposed to alcohols. In the presence of hydrogen in nitrogen, the workfunction change of Pt NCs due to hydrogen adsorption is the likely cause for the sensing behavior of these sensor hybrids.

[00100] *Selectivity of GaN/(TiO_2-Pt), GaN/Pt, and GaN/TiO_2NWNC hybrid sensors*

[00101] A significant finding of the present invention is the change in the selectivity of GaN/TiO_2 hybrid sensors due to the addition of Pt NCs. The observed selectivity behavior of the three hybrids can be qualitatively explained if the heat of adsorption of the analytes on TiO_2 and Pt surfaces is considered as shown in **Table II** and their ionization energies presented in **Table III**.

Table II: Heat of Adsorption for Methanol, Benzene, and Hydrogen on Pt and TiO_2 (Anatase*)

Surface	Hydrogen (kJ/mol)	Methanol (kJ/mol)	Benzene (kJ/mol)
TiO_2	Negligible	92	64
Pt	100	48	117

*The heat of absorption values for TiO2 rutile surfaces are comparable

Table III: Ionization Energy of the Analytes (CRC Handbook of Chemistry and Physics, 84th ed.; CRC Press: Boca Raton, FL., 2003):

Organic Compound	Ionization Energy (eV)
Methanol	10.85
Hydrogen	13.5
Benzene	9.25

[00102] Referring to **Table II**, benzene has a higher heat of adsorption on Pt than on TiO_2. Therefore, benzene will preferentially adsorb on Pt in the TiO_2-Pt cluster. Now, in the absence of Pt, when the benzene is adsorbed on TiO_2 it can interact with the photogenerated charge carriers resulting in the sensing behavior of GaN/TiO_2 devices. However, if benzene is adsorbed on Pt (such as in the case of TiO_2-Pt and Pt nanoclusters on GaN) then benzene molecules cannot interact with photogenerated charge carriers in TiO_2, and therefore are ineffective in producing any current modulation in the nanowire. Thus, benzene is detected by GaN/TiO_2 sensor devices, but not by GaN/(TiO_2-Pt) and GaN/Pt sensor devices.

[00103] Further, methanol is detected by GaN/(TiO_2--Pt) sensors only, and not by GaN/TiO_2 and GaN/Pt sensors. From **Table III**, methanol (unlike benzene) effectively adsorbs on TiO_2, whether Pt is present or absent (as the heat of adsorption of methanol is higher on TiO_2 than Pt). It is believed that methanol on TiO_2 in the absence of Pt does not participate in photogenerated carrier trapping as efficiently as benzene and other aromatic compounds on the TiO_2 nanoclusters. Referring to **Table III**, the ionization energy of methanol, hydrogen, and benzene is shown. The effectiveness of the process of hole transfer to the adsorbed organic molecules is related to the compound's ability to donate an electron (*i.e.* the lower the ionization energy of a compound, the easier for it to donate an electron or capture a hole). However, in the presence of Pt nanoclusters nearby, methanol adsorption on TiO_2 ultimately leads to formation of H^+ through photo-oxidation of methanol, and eventually H_2, which is the key molecule for sensing of methanol by (TiO_2-Pt) NCs on GaN NW. A similar mechanism applies for ethanol sensing by the GaN/(TiO_2--Pt) hybrids.

[00104] Hydrogen is detected by GaN/(TiO_2-Pt) and GaN/Pt hybrids, and not by GaN/TiO_2 NWNC sensors, and GaN/(TiO_2-Pt) sensors have a higher response to hydrogen than to alcohols. From **Table II**, hydrogen has negligible heat of adsorption on TiO_2, thus GaN/TiO_2 devices are not sensitive to hydrogen. However, in the presence of Pt NCs on TiO_2, hydrogen can adsorb on the Pt NCs. Once adsorbed, hydrogen can modify the workfunction of Pt, resulting in a change in the photocurrent through the nanowire. However, this is not the only mechanism, as that would imply that GaN/Pt hybrids should be equally sensitive to H_2. It is believed that when hydrogen is adsorbed on the TiO_2-Pt NC, it also reduces the TiO_2 surface. Thus, in the presence of only Pt on GaN, workfunction modification of Pt solely produces change in the photocurrent in the NW. However, in the presence of Pt and TiO_2 NCs, hydrogen adsorption leads to the modulation of the photocurrent in GaN NW, through modulation of Pt workfunction together with the change in the depletion layer of the TiO_2 NCs, resulting in a larger change of the photocurrent, thus higher sensitivity.

[00105] The faster and larger response of GaN/(TiO_2-Pt) towards H_2 compared to the alcohols (as shown in **Figure 5**) is due to the fact that in the case of alcohols, hydrogen is produced after photo-oxidation of the adsorbed alcohols, which is a two-step process with lower yield. In the case of H_2 in nitrogen, there is a direct availability of H_2 molecules.

[00106] GaN/(TiO_2-Pt) sensors are not sensitive to high carbon-containing (C>2) alcohols such as propanol and butanol. In this regard, it has been shown that the hydrogen production from the photocatalytic oxidation of alcohols on TiO_2/Pt surface is related to the polarity of the alcohols (*i.e.*, the higher the polarity of the alcohol the greater the yield of photocatalytic hydrogen production) (see Yang Y Z *et al.* (2006) "*Photo-Catalytic Production of Hydrogen Form Ethanol over M/TiO2 Catalysts (M=Pd, Pt or Rh)*," Applied Catalysis B: Environmental 67:217-222). The polarity (Y) is defined as $Y = (\varepsilon_s - 1)/(\varepsilon_s + 2)$, where ε_s is the relative permittivity of the solvent. **Table IV** lists the polarity of various alcohols tested.

Table IV: Solvent Polarity of Various Alcohols

Solvent	Polarity
Methanol	0.91
Ethanol	0.89
n-Propanol	0.86
i-Propanol	0.85
Butanol	0.84

[00107] The relative difficulty of producing hydrogen from higher carbon-containing alcohols (C > 2) is believed to be the cause of the GaN/(TiO_2-Pt) sensor's inability to detect alcohols with C greater than 2. The sensor's greater response to methanol than ethanol (at least for concentrations above 500 μmol/mol) is also consistent with the polarities of the alcohols.

[00108] The GaN/(TiO_2-Pt) hybrid sensors are operable at room-temperature sensing of hydrogen, and thus are suitable for various applications (*e.g.*, industrial production facilities, oil refineries, hydrogen monitoring in hydrogen-powered vehicles, alcohol monitoring systems for industrial and law-enforcement purposes, *etc.*). The disclosed mechanisms and methods may be implemented for achieving other multicomponent NWNC based sensors. Through combinations of metal and metal-oxides available, a library of sensors may be produced, each with precisely tuned selectivity, on a single chip for detecting a wide variety of analytes in many different environments.

[00109] Thus, an inactive semiconductor nanostructure (*e.g.*, NW) surface may be functionalized with selected analyte-specific active metal-oxide nanoparticles. For example, another embodiment of the present invention provides for alcohol sensors using gallium nitride (GaN) nanowires (NWs) functionalized with zinc oxide (ZnO) nanoparticles. The disclosed sensors operate at room temperature, are fully recoverable, and demonstrate a response and recovery time on the order of 100 seconds or less. The sensing is assisted by ultraviolet (UV) light within the 215-400 nm band and with the intensity of 375 nW/cm^2 measured at 365 nm.

[00110] As discussed above, the conductivity model of GaN nanostructure is comprised of a conducting channel surrounded by a surface depletion region, where modulation in the width of the depletion region induces a change in the conductivity of the NW. Similarly, ZnO nanoparticles have a surface depletion layer, which enhances upon exposure to air due to electron capture by surface-adsorbed oxygen. When UV light is turned on, the photogenerated holes in ZnO assist in removing the adsorbed oxygen, thus releasing the electrons captured by surface oxygen back into ZnO. The photoinduced excess of electrons in the ZnO nanoparticles promotes photogenerated charge separation in the GaN nanostructure, thereby resulting in increased conductivity. Conversely, there is a reduction in the number of free electrons in the ZnO nanoparticles when exposed to air, leading to a reduced conductivity. As seen in **Figure 6**, this effect increases with increasing flow rate of air due to enhanced coverage of the device surface with adsorbed oxygen.

[00111] The device response to alcohols may be explained by the following generic reaction occurring on the surface of ZnO:

$$2CH_3OH + O^-_2 \text{(adsorbed)} \longrightarrow 2HCHO + 2H_2O + e^- \quad \text{(Equation 6)}$$

[00112] As shown in **Figure 7**, the exposure to alcohol vapors leads to increased device conductivity due to the removal of adsorbed oxygen. In the case of exposure to N_2, although there is no surface reaction, N_2 assists in desorption of the oxygen, thus restoring the conductivity, as shown in **Figure 8**.

[00113] The disclosed hybrid GaN nanostructure/ZnO nanoparticle devices are suitable for UV-assisted alcohol sensing at room temperature. These devices are a suitable

candidate for making nanosensor arrays because of their tunable selectivity, ability to detect the pbb level of analytes, and fast response and recovery time.

[00114] The disclosed hybrid chemiresistive architectures utilizing nanoengineered wide-bandgap semiconductor backbone functionalized with multicomponent photocatalytic nanoclusters of metal-oxides and/or metals are particularly suitable for larger scale manufacturing techniques, such as for commercial applications. The sensors operate at room-temperature via photoenabled sensing. A substantial benefit of the disclosed sensors is the utilization of all standard microfabrication techniques, thus resulting in economical, multianalyte single-chip sensor solution. By combining the "designer" adsorption properties of multicomponent nanoclusters together with sensitive transduction capability of nanostructured semiconductor backbones, photoenabled, room temperature, ultra-sensitive, and highly selective chemical sensors are achieved.

[00115] The sub-micron structures may be formed on an epitaxial thin-film grown on non-conductive/semi-insulating substrate using deep UV lithography and a combination of plasma etching and wet-etching. Such structures are functionalized with multicomponent nanoclusters of metal-oxides and metals using reactive-sputter deposition, as noted above.

[00116] Referring to **Figure 9**, an exemplary structure of a semiconductor-nanocluster hybrid sensor is illustrated. Referring to **Figure 9, plate (a)**, the sensor may comprise a two-terminal sub-micron wide semiconductor backbone, functionalized with nanoclusters of metal-oxides and/or metals. For example, the sensor may include a lightly-doped 0.8-0.25 μm wide semiconductor two-terminal structure on a non-conductive substrate (*e.g.* sapphire) formed using traditional deep UV photolithography and plasma etching. Functionalization is a discontinuous layer of multicomponent nanoclusters (*e.g.*, each nanocluster comprising one or more photocatalytic metal-oxide nanoclusters (diameter 20 nm and smaller) and smaller metal nanoparticles (5 nm and smaller) deposited on top of it). The multicomponent design may include more than one oxide and metal types in the nanoclusters, and exhibits tailored adsorption properties by virtue of the multicomponent design. The functionalization layer is deposited using reactive sputtering technique followed by thermal treatment - all standard semiconductor microfabrication processes. The sensors work with low-intensity light, such as from an LED. The emission wavelength is determined

by the semiconductor and metal-oxide bandgaps. **Figure 9, plate (b)** illustrates schematically an exemplary thin-film device including a semiconductor backbone functionalized with TiO_2 on a sapphire substrate. The smoothness of the substrate and film after thermal processing is shown in **Figure 9, plates (c) and (d)**.

[00117] Surface defects of metal-oxides are the active sites for adsorption of various chemicals. However, at room-temperature the adsorbed oxygen and water are very stable. This necessitates heating in traditional metal-oxides sensors. Most metal-oxides are well-known photocatalysts, with photoexcitation wavelengths in the range of ultraviolet to visible, corresponding to the material bandgap. A disclosed approach uses dynamic surface-defects generation in the metal-oxide cluster through illumination, which allows for efficient photodesorption of adsorbed water and oxygen. This has at least two benefits: 1) low-power, room-temperature operation, which also increases the lifetime of the sensors, and 2) real-time dynamic range modulation by changing the intensity of light (for ppt level detection the intensity of the LED can be increased as compared to ppm level detection).

[00118] The sensor architecture provides for the combination of a crystalline top-down fabricated semiconductor backbone with a discontinuous nanocluster surface layer. In metal-oxide gas sensors, the resistance changes due to diffusion and adsorption of gases along the grain boundaries. As the present architecture uses a discontinuous, nano-island like metal-oxide layer, the bottleneck of gas diffusion through grain boundaries, as in traditional metal-oxide sensors, is not present. This makes the disclosed sensors respond relatively fast as compared to conventional sensors, and operable at room-temperature. Unlike traditional metal-oxide sensors, the disclosed design provides that the current is carried by the high-quality, high mobility semiconductor backbone, which makes the sensor fast. Also, the absence of conduction in the nanocluster layer makes the active layer inherently stable as compared to traditional metal-oxide thin film sensors (*e.g.*, grain boundary motion, defect generation and propagation, and reduction of the metal-oxide layer is not possible due to the absence of a "closed-circuit").

[00119] Due to the nanocluster layer of the disclosed sensors, designed with a specific adsorption profile, they are extremely efficient in adsorbing target analytes. This enables the design of highly-selective sensors. Two component, three component, four

component, or five or more component cluster designs are possible for unprecedented selectivity tailoring.

[00120] Most semiconductors have depletion regions associated with them. The surface band bending, which is a consequence of the surface depletion, facilitates the diffusion of the photogenerated holes to the surface. This separation of carriers effectively suppresses their recombination. The degree of separation is determined by the surface potential modification by the clusters. Such separation of photocarriers increases their lifetimes, leading to higher photocurrent and thus sensitivity towards such surface potential modifications. The processes that enable sensing of different adsorbed molecules with the disclosed multicomponent nanocluster functionalization is shown schematically in **Figure 10**.

[00121] Assuming typical values of the response/recovery times for 500 ppt of NO_2, from the kinetic theory of gases the flux F of NO_2 arriving on a surface is given by the formula:

$$F = \frac{N_A P_{partial}}{\sqrt{2\pi MRT}} \qquad \text{(Equation 7)}$$

[00122] where N_A is the Avagadros' number, M is the average molar weight of the molecule, P is the pressure, T is the temperature, and R is the gas constant.

[00123] For 500 ppt concentration of NO_2 in air, three molecules of NO_2 are impinging on a 20 nm diameter metal-oxide cluster per second. Now, the residence time τ of an adsorbate at temperature T on a surface is given by the relation $\tau = \tau 0 \ exp\ (\Delta H_{ads}/RT)$, where ΔH_{ads} is the heat of adsorption, and $\tau 0$ is correlated with surface atom vibration (roughly 10^{-12} s). Thus, at 298 K the residence time for NO_2 molecule on WO_3 nanocluster is approximately 15 seconds (considering ΔH_{ads} for NO_2 on WO_3 to be 18 kcal/mol). Considering roughly 10^{21} cm^{-3} of defect density for typical metal oxides, results in roughly 300 adsorption sites on a 20 nm diameter nanocluster. Assuming sticking coefficient of 1, by 110 seconds the surface defects are saturated. Thus, response time may be estimated to be in the order to 100 seconds, and recovery time in the order to 15-30 seconds.

Although the design of the nanocluster is described from pure thermodynamic standpoint, other surface kinetics (such as diffusion, desorption) may also be considered.

[00124] For fabricating the sensor backbone, un-doped (1×10^{16} cm^{-3}) to lightly doped (1×10^{17} cm^{-3}) semiconductor epitaxial layer (1 μm thick) on sapphire/insulating/semi-insulating substrates may be utilized, as shown in **Figure 11**. Lower doping is needed for the sensors to be photo enabled. The thickness of buffer layer controls the defects arising from lattice and thermal mismatch. Ideally suited layer structures require a relatively thin buffer layer (*e.g.*, about 250 nm) to suppress the parasitic conduction in the buffer layer. Similar designs may also be provided with other direct gap semiconductors, such as ZnO, InN, AlGaN and virtually any other direct gap semiconductor material.

[00125] The design of submicron semiconductor backbone including physical layout and geometry is described with reference to **Figure 12**. Both serial and parallel architectures for the semiconducting resistive backbone have unique advantages and disadvantages as the chemiresistor backbone. Serial architecture has higher resistance which results in lower-power operation, whereas parallel architecture produces more robust devices insensitive to material quality variation in the individual sections. However, the calculation will show that the response R is the same for both serial and parallel architecture:

$$R = \frac{R_{analyte} - R_{air}}{R_{air}} \qquad \text{(Equation 8)}$$

wherein $R_{analyte}$ and R_{air} are the resistances in presence of analyte and in air, respectively. However, the resolution of the sensor (*i.e.,* smallest change in concentration it can measure as required for proposed large dynamic range sensors) is greater in a serial architecture.

[00126] The series sensor element provides for a meander shape, with integrated passive sections as real-time calibration elements. An exemplary design is shown in **Figure 13, plate (a)**. The surface area-volume ratio for this structure is roughly 3.1. The sidewalls of the backbone may be intentionally angled, such as at 85° as shown in **Figure 13, plate (b)**. This ensures uniform coverage of the nanoclusters on the sidewalls of the structure, and also ensures uniform photoexcitation of the semiconductor backbone. The device is

biased by a standard three dc voltage source (two AA batteries in series) and the sensor output is the voltage measured between the pads $+V_{sensor}$ and ground. The design provides various benefits including: 1) high sensitivity and resolution; 2) low-power consumption; 3) simplified interface circuit; and 4) ability for real-time base-line drift calibration and temperature compensation even in presence of analytes.

[00127] Using circuit analysis, it can be shown that Sensitivity S (as defined in **Figure 14**) may be simplified considering $R_L << R$ as:

$$S = \frac{R_L \times V_{dc}}{NR} \left[\frac{1}{\frac{R}{\Delta R} + 1} \right] \qquad \text{(Equation 9)}$$

wherein R_L is the external low-noise precision load resistance (*e.g.*, see **Figure 13, plate (a)**), N is the number of segments, R is the resistance without analyte of single segment, and ΔR is the resistance change of the single segment in presence of the analyte, and V_{dc} is the dc source voltage.

[00128] Thus for higher sensitivity, N should be small, and R_L and V_{dc} should be large. However, resolution of a sensor is the smallest change in concentration of the analyte it can measure (it is different from lowest detection limit), and is often limited by the noise. Considering only thermal noise current in the total sensor, the output sensor voltage noise can be expressed as:

$$V_{sensor}(noise) = R_L \sqrt{\frac{4k_B T \Delta f}{NR}} \qquad \text{(Equation 10)}$$

wherein k_B is the Boltzmann Constant, T is the temperature, and Δf is the bandwidth. Considering both Equations 9 and 10, the tradeoff between high sensitivity and resolution is clear. The effect of N (*i.e.*, number of segments) on the sensor performances such as sensitivity, detection limits, and resolution, may be investigated.

[00129] Referring again to **Figure 13, plate (a)**, the resistance of the active sensor area may be computed using the formula, neglecting the bends:

$$R \approx \frac{\rho \times (4 \times L_s)}{h \times (W_s + W_0)/2} \qquad \text{(Equation 11)}$$

wherein $\rho = 1/(nq\mu)$, ρ is the resistivity, n is the carrier concentration, and μ is the mobility (see also dimensions shown in **Figure 13, plate (b)**).

[00130] For example, for the GaN backbone with dimensions shown in **Figure 13**, the active-area photoresistance under 365 nm excitation from LED is ≈ 60 kΩ, assuming a mobility of 300 cm^2V^{-1} s^{-1} and electron concentration of 1 × 10^{17} cm^{-3}. The device is considered to be excited by low-intensity (10 μW/cm^2) 365 nm LED. The GaN absorption coefficient α=10^5 cm^{-1} for the 365 nm photon is assumed. If the sensor is biased with 3 V dc and with an external 10 KΩ resistor, the power dissipation is approximately only 40 μW. The sensor power dissipation when in offstate (LED turned off and the sensor has only dark current) is even lower. The total power requirement for the sensor must also include the power required for LED operation. There are several low-power UV (365 nm) LEDs (FOX GROUP) that could be run by LED drivers. Power dissipation for the LED could be low as 0.5 mW, if we drive the LED for very low intensity. Using a LED driver to control the intensity has an added benefit of the real-time dynamic range configuration.

[00131] The simplified chemiresistive architecture lends itself easily to integration with interface devices as compared to more complex devices such as metal-oxide-semiconductor field-effect transistors (MOSFETs). The nano-watt operation amplifier (OP-Amp) TS1001 from Touchstone Semiconductor is identified, which can provide a gain of 100 when operated in single-input voltage amplifier configuration. The Op-Amp operated from a single AA battery dissipated about 1 μW.

[00132] In one implementation, a feature of the present design is the inclusion of the voltage probes (V_{cal}) for calibration of base line drift of the photoresistance of the total structure. As the area under the calibration probes is encapsulated with thick SiO_2, the voltage drop (V_{cal}) for a fixed intensity of illumination through the entire structure will enable compensation for drift in the baseline photoresistance arising from persistence photoconductivity or temperature-induced drift.

[00133] Another feature of the present design is the "tailored" adsorption profile through the multicomponent nanocluster design, as described above. The design provides for suppressing the competitive adsorption of an interfering chemical on a surface with two different adsorption profiles, which is achieved using a primary and a secondary component.

[00134] In this regard, **Figure 16** illustrates an exemplary multicomponent design for the target analyte of NO_2 and for the interfering chemical of CO_2. Adsorption profile for another target analyte or set of analytes along with a set of interfering chemicals may alternatively be provided utilizing a similar configuration. The primary metal-oxide component is chosen so that the heat of adsorption of NO_2 on its surface is large compared to CO_2. The secondary component (e.g., the metal) is chosen with the heat of adsorption for CO_2 larger than the metal-oxide. Thus NO_2 and CO_2 preferentially adsorb on the metal-oxide and the metal, respectively. When NO_2 is adsorbed on the metal-oxide, it interacts with the photogenerated charge carriers, producing modulation of the semiconductor backbone photocurrent, as explained above. However, when CO_2 is adsorbed on the metal, due to the large concentration of electrons, there is minor change in the cluster potential. Consideration of other effects, such as catalytic decomposition on the metal, spill-over from the metal to metal-oxide, and change of metal-work function due to adsorption of gases, may also be appropriate.

[00135] Due to the highly dispersed nature of the metal phase, even if there is a change in the physical properties of the metals, it has only marginal impact on the cluster properties. Although the general design principles are described, the specific designs of the appropriate clusters may be fine-tuned for optimal performance and selectivity. For example, **Table V** below demonstrates possible cluster designs for NO_2 and benzene sensing. Considering the heat of adsorption of NO_2 on WO_3 and Pt, bigger WO_3 clusters with much smaller and dispersed phase of Pt may be favorable. Although, adsorption energy for NO_2 is comparable on both WO_3 and Pt, due the higher surface area of metal-oxide clusters, most of NO_2 will adsorb on the WO_3, whereas CO_2 will mostly adsorb on the Pt. For BTEX sensing, the TiO_2/Fe is favorable.

Table V: Heat of adsorption on different candidates for the multicomponent cluster design.

Possible Cluster Designs for NO_2 sensing:		
Metal-Oxide/Metals	NO_2 (kcal/mol)	CO_2 (kcal/mol)
MgO	9.0	3.5
TiO_2	21.0	29
WO_3	18.4	negligible
Fe(111)	64.5	69
Pt(111)	19	40.5
Possible Cluster Designs for Benzene sensing:		
Metal-Oxide/Metals	Benzene (kcal/mol)	CO_2 (kcal/mol)
TiO_2	15.2	29
Fe (111)	22	69

[00136] Note that the values in **Table V** are average adsorption energies at room temperature for low adsorbate coverage. The values are collected from experimental results (temperature programmed desorption and calorimetric studies) and theoretical calculations (such as density function theory). The values shown are for common and stable oxide surfaces. Experimental heat of adsorption values are dependent on various factors, including the morphology and crystal orientation of the surface.

[00137] Other design considerations for the nanoclusters include:

1) **Bandgap of the oxide:** as single wavelength excitation is used for both photodesorption of surface oxygen and hydroxyl species, and for creating photocarriers in the semiconductor (e.g. GaN), the bandgap of the oxide should be lower or equal to GaN bandgap (as shown in **Figure 15**). Candidates are shown in **Table VI** below.

TABLE VI: Bandgaps of Common Metal Oxides

Metal-Oxides	Bandgap (eV)
MgO	7.1
TiO_2	**3.2**
WO_3	**2.8**
Fe_2O_3	**2.1**
V_2O_5	**2.3**
NiO	3.6
Al_2O_3	7.0

Candidates are in bold and underlined, $E_g < 3.4$ eV.

2) Nature of surface defect types: surface defects (*i.e.* the active adsorption sites) of metal-oxides are of three types: bronstead, lewis-acid/base sites, and redox sties. Organic compounds such as benzene predominantly adsorb by dehydgrogenetion (*i.e.*, removal of H+) requiring surface lewis sites. On the other hand, NO_2 predominantly adsorbs as surface nitrate (NO_3^-), requiring base sites. Most metal-oxide surfaces at room-temperature are hydroxylated, and thus photoexcitation will increase the concentration of one type of predominant defects.

3) Redox potentials of the oxide: redox potentials of oxides indicate the ability of photogenerated carriers to oxidize or reduce any adsorbed molecule. Depending on whether molecules will be oxidized or reduced on the surface, they interact with charge carriers differently in the clusters.

4) Stability of the adsorbates: Stability of the adsorbed species is an important consideration, as it determines the recovery time, and ultimately usability of the sensors. As can be seen for Fe, where the very high adsorption energy might produce very stable NO adsorbed species on the surface, rendering the nanoclusters inactive after exposure to high concentrations of NO_2.

5) Nature of the adsorbed species (molecular or dissociative): nature of the adsorbed species determines the photochemical reaction pathways and ultimately

the sensitivity. Additional multicomponent nanocluster designs for NO_2 and BTEX sensing are shown in **Table VII**.

TABLE VII: Possible designs of nanoclusters

Metal-Oxides/Metal	Target Analyte
WO_3/Pt	NO_2
TiO_2/Fe	BTEX

[00138] The use of heterogeneous metal-oxide supported metal catalysts in industrial production, abatement, and remediation for the past few decades has been extensive, and generated an exhaustive body of literature that may be readily utilized for nanocluster designs according to the present invention. Indeed, some of the systems are well-understood, so that a desired selectivity outcome may be readily predicted. The well-known strong metal/support interactions (SMSI) effects in heterocatalysts are different, as the metals are not reduced on the oxides in the disclosed devices.

[00139] Computing the size and coverage of the clusters is an important consideration, given the size and coverage of the NCs ultimately determines the overall sensitivity of the device. Thus, determination of the most effective size and coverage of the clusters is desirable. It is known that the surface area and relative particle size has a significant effect on the catalytic properties of metals and metal oxides. However, due to the presence of metals on the metal-oxide clusters, there will be significant depletion of the metal-oxide clusters. Thus, overly small metal-oxide clusters would be substantially depleted and hamper effectiveness, whereas overly large clusters would also result in lower sensitivity. Consideration of the nature of the depletion regions formed by such nano-sized metal clusters on a semiconductor is therefore prudent.

[00140] The classical Schottky model depletion theory cannot predict accurately the zero-bias depletion width produced by metallic nanoclusters on a semiconductor. According to Zhdanov's model, the depletion depth associated with such metal nanoclusters on a semiconductor can be estimated by the following relationship:

$$w_d = \left(\frac{3 r_c V_{bi}}{2\pi q^2 N_d} \right)^{1/3} \qquad \text{(Equation 12)}$$

wherein w_d is the depletion width, r_c is the radius of the nanocluster, V_{bi} is the built-in voltage for the junction, q is the elementary charge, and N_d is the dopant concentration in the semiconductor.

[00141] The plot in **Figure 17** demonstrates the depletion width of TiO_2 clusters due to Pt particles. It is clear that 4 nm of Pt clusters on 20 nm diameter TiO_2 clusters would produce depletion of about 5 nm in the TiO_2.

[00142] Coverage of the metal-oxide nanocluster functionalization is determined by the limit of formation of continues metal-oxide film. The coverage is dependent on various parameters such as metal-oxide wetting of the semiconductor, morphology of phases formed after thermal treatment, *etc.*, and may be verified by SEM imaging. The metal coverage should be sparse to ensure only partial depletion of the clusters.

[00143] With regard to fabrication, techniques such as wet chemical etching may not be suitable for etching nanoscale, high aspect-ratio nanostructures due to undercutting of the mask and sloped sidewalls. Hence, the development of a dry etching process with relatively less low damage and precise-depth control capability is preferred for the fabrication of nanostructures. Such etching of semiconductor nanostructures is described in further detail in Example 4 below.

[00144] Referring to **Figure 18**, the components for an exemplar interface circuit is illustrated. The LED intensity may be controlled by the microcontroller (MAXQ3213, with a LED driver). By relatively simple design change of a selected multicomponent cluster, different applications are readily provided. In addition, using wide bandgap material as a backbone enables the sensor to work at elevated temperatures, and in presence of radiation and other harsh environmental conditions.

[00145] As shown in **Table VIII** below, the possible designs of the multi-component nanoclusters are virtually unlimited, resulting in the ability to provide sensors for numerous applications.

TABLE VIII: Exemplary Designs of Multicomponent Nanoclusters

Semiconductor	Nanocluster Components: Metal Oxide:	Metal:
GaN InN AlGaN	Titanium Oxide	Titanium
	Tin Oxide	Nickel
	Iron Oxide	Chromium
	Magnesium Oxide	Cobalt
	Vanadium Oxide	Ruthenium
	Nickel Oxide	Rhodium
ZnO InAs	Zirconium Oxide	Gold
	Aluminum Oxide	Silver
	Copper Oxide	Platinum
	Zinc Oxide	Palladium
	Strontium Oxide	Vandium

[00146] Thus, in accordance with the disclosed methodologies, sensor devices suitable for a wide range of applications are achieved. Further, the particular architecture of the sensor devices may be readily tailored for the desired application and associated conditions, as well as one or multiple active sensor elements configured for sensing particle targets.

[00147] Thus, the disclosed sensor devices may comprise various active sensor elements and passive elements for formation of on-chip circuits. Multiple active elements may be provided with a combination of different functionalization to detect multiple gases in a single chip. The chip may include precise passive elements (elements which have the same semiconductor backbone but passivated from the environment), for calibration on the same chip, which has the same temperature coefficient for current as the active sensor element. Thus, any change due to the temperature or aging can be a calibrated out using the on-chip calibration element(s). Using such on-chip components, bridge circuits may be provided directly on the chip, allowing for sensor devices with high resolution.

[00148] Although the sensor devices may comprise a micro-heater element as noted above, such element is not required. The disclosed sensor devices do not need to be heated for sensing, and are capable of sensing a host of gases at room temperature. Total power consumption is extremely low (e.g., an exemplary 8 active sensor element device

provided for a total power consumption about 10 microwatts. Further, the disclosed sensor devices are stable and recoverable even in the presence of corrosive gases (e.g, HCN, CL_2, HCl, *etc*), and capable of withstanding very high gas concentrations. The sensor devices are also capable of operating in oxygen rich or relatively lean conditions.

[00149] In accordance with disclosed embodiments, the active sensor(s) elements are designed by first selecting a nanoclusters and/or a layer of a base photocatalytic metal oxide (e.g., TiO_2, V_2O_5, Cr_2O_3, Fe2O3, CoO, NiO, CuO, ZnO, ZrO_2, WO_3, MoO_3, SnO_2). Nanoclusters of a catalytic metal (e.g., Ti, V, Cr, Fe, Co, Ni, Cu, Al, Zr, Nb, Mo, Ru, Rh, Pd, Ag, Hf, Ta, W, Re, Ir, Pt, Au) are then applied on top of the base photocatalytic metal oxide nanoclusters. Alternatively in other embodiments, nanoclusters of a second photocatalytic metal oxide different than the base metal oxide are applied on top of the base metal oxide, providing for dual metal oxide functionalizations. Thus, the sensor element comprises a base layer or nanoclusters of a first metal-oxide, and nanoclusters of a second metal oxide or metal. The selection of the particular metal oxide and metal provides for the desired selectively.

[00150] A summary of operational and performance specifications of sensing devices in accordance with disclosed embodiments is set forth in **Table IX** below:

Analyte	Range of Detection	Response (%) = (R_{gas}-R_{air}/R_{air})
Ammonia	1 – 100 ppm	15
Chlorine	0.5 – 10 ppm	212
Hydrogen chloride	1 – 100 ppm	74
Hydrogen cyanide	1 – 100 ppm	10
Hydrogen sulphide	10 – 1000 ppm	20
Hydrogen	0.5 – 10 %	500
Oxygen	10 – 30 %	40
Carbon dioxide	01. – 1 %	2
Carbon monoxide	10 – 300 ppm	15
Nitrogen dioxide	100 – 500 ppm	2
Nitric oxide	5 – 1000 ppm	2.6
Methane	50 – 5000 ppm	9

[00151] The disclosed devices are suitable for environmental monitoring, hazmat, large-scale industrial monitoring and control, explosive threat detection, and other markets where rapid detection of gases and chemicals in air is desired. Compared to conventional sensors, the disclosed sensors of the present invention are extremely small (*e.g.*, 4 mm × 4 mm, or 2.5 mm × 2.5 mm, or smaller) and inexpensive, exhibit low power consumption (*e.g.*, less than 100 microwatts, and in some embodiments less than about 10 microwatts), but capable of sensing a large dynamic range (*e.g.*, 100 parts per billion to >2%), detect a variety of chemicals under various conditions with no cross-sensitivity (thus minimizing false positives), and exhibit a long operating life. In addition, the disclosed sensors of the present invention may be manufactured using the same manufacturing methodologies utilized for producing conventional integrated circuits.

[00152] The disclosed sensor devices may be installed in residential and commercial buildings for on-demand ventilation control, resulting in a decrease in energy consumption. The sensors can detect the presence of harmful VOCs (Benzene, Xylene, and formaldehyde), which are often emitted by building materials, paints, and furniture, and are also associated with human metabolism. After detecting an increase in the levels of

targeted harmful chemicals, the ventilation system may be adjusted for safety, comfort and health of the occupants. Alternatively or in addition, the sensors could monitor CO levels and gas leaks in buildings for safety. Thus, the disclosed sensor technology may be readily implemented in indoor monitoring systems, thereby generating large cost savings in terms of energy efficiency, health of the occupants, and low-maintenance costs.

[00153] In case of accidental release of chemicals, the disclosed sensors are suitable for use by first-responders to detect the presence of chemicals and associated hazards. Thus, the challenges of a disaster may be managed more safely and efficiently. The disclosed hybrid sensor technology may be implemented in ultra-small, handheld units, which identify multiple hazardous materials with low power consumption. Such devices would be ideal for first responders.

[00154] The disclosed sensors are also suitable for industrial monitoring applications. For example, the sensors may be used for monitoring different gases for process control in industrial facilities such as oil refineries, manufacturing plants, etc. They may be installed at various points throughout an industrial facility for point detection for leaks of toxic chemicals. The may also be implemented in personal monitoring devices for recording personal exposure levels for compliance purposes with state and federal maximum exposure level regulations. The disclosed technology therefore promises unlimited control over the sensor design, thus having the ability to produce sensors for various different industries and processes.

[00155] Implementations of the disclosed technology for law enforcement and safety applications are also provided. For example, the disclosed sensors may be utilized in breath analyzers for law-enforcement and individual use. The hybrid sensors may also be integrated into hand-held devices (*e.g.*, cell phones) as plug-in modules to existing devices. For example, the disclosed sensor may be integrated into a hand-held device to enable a user to check his or her blood alcohol level.

[00156] Implementations of the disclosed sensor technology are also suitable for defense and security applications. The sensors may be used for safety monitoring in public places such as subway/rail stations, airports, public buildings, and in transit systems. For example, the sensors may be utilized to monitor and detect deliberate release of harmful

chemicals and explosives, thus protecting civilians from attacks. They may also be integrated into equipment carried or worn by soldiers for detection of harmful chemicals, explosives, or other terrorist elements.

[00157] Having generally described the invention, the same will be further understood through reference to the following additional examples, which are provided by way of illustration and are not intended to be limiting of the present invention unless specified.

EXAMPLES

EXAMPLE 1

[00158] Nanowire-nanocluster hybrid chemical sensors were realized by functionalizing gallium nitride (GaN) nanowires (NWs) with titanium dioxide (TiO_2) nanoclusters for selectively sensing benzene and other related aromatic compounds.

Materials and Methods

[00159] C-axis, *n*-type, Si-doped GaN grown by catalyst-free molecular beam epitaxy on Si (111) substrates were utilized. For details of NW growth, see Bertness K A *et al.* (2008) "*Mechanism for spontaneous growth of GaN nanowires with molecular beam epitaxy*," J. Crystal Growth 310(13):3154-3158). An exemplary process of sensor fabrication is shown in **Figure 19**. Post-growth device fabrication was done by dielectrophoretically aligning the nanowires on 9 mm × 9 mm sapphire substrates (see Motayed A *et al.* (2006) "*Realization of reliable GaN nanowire transistors utilizing dielectrophoretic alignment technique*," J. Appl. Phy. 100:114310). The device substrates had 12 nm thick Ti alignment electrodes of semi-circular geometry with gaps between them ranging from 4 μm to 8 μm. After the alignment of the nanowires, the samples were dried at 75°C for 10 min on a hot plate for evaporation of the residual solvent. This was followed by a plasma enhanced chemical vapor deposition (PECVD) of 50 nm of SiO_2, at a deposition temperature of 300°C. This passivation layer was deposited to ensure higher yield for the fabrication process.

[00160] After the oxide deposition, photolithography was performed to define openings for the top contact. The oxide in the openings was etched using reactive ion

etching (RIE) with $CF_4/CHF_3/O_2$ (50 sccm/ 25 sccm/ 5 sccm) gas chemistry. The top contact metallization was deposited in an electron-beam evaporator with base pressure of 10^{-5} Pa. The deposition sequence was Ti (70 nm)/ Al (70 nm)/ Ti (40 nm)/ Au (40 nm). The oxide layer over the nanowires between the end contacts was then etched in buffered HF etching solution for 15 seconds. A negative resist was used to protect the end metal contacts from the etching solution.

[00161] The TiO_2 nanoclusters were deposited on the exposed GaN NWs using RF magnetron sputtering. The deposition was done at 325°C with 50 sccm of Ar flow, and 300 W RF power. The deposition rate was about 0.2 Å/s. Thermal annealing of the complete sensor devices (GaN NW with TiO_2 nanoclusters) was done at 650°C to 700°C for 30 seconds in a rapid thermal processing system with 6 slpm (standard liter per min) flow of ultrahigh purity Ar. A relatively slow ramp rate of 100°C per min was chosen to reduce the stress in the metal-nanowire contact area during heating. The anneal step was optimized to facilitate Ohmic contact formation to the GaN NWs and also to induce crystallization of the TiO_2 clusters. Additional lithography was performed to form thick metal bond pads with Ti (40 nm) and Au (160 nm).

[00162] The crystallinity and phase analysis of the sputtered TiO_2 films were assessed by X-ray diffraction (XRD). The XRD scans were collected on a Bruker-AXS D8 scanning X-ray micro-diffractometer equipped with a general area detector diffraction system (GADDS) using Cu-Kα radiation. The two-dimensional 2Θ-χ patterns were collected in the 2Θ = 23° to 51° range followed by integration into conventional Ω -Θ scans. The microstructure and morphology of the sputtered TiO_2 films used for fabrication of sensors were characterized by high-resolution analytical transmission and scanning transmission electron microscopy (HRTEM/STEM) and cold field-emission scanning electron microscopy (FESEM). GaN nanowires with sputtered TiO_2 were deposited onto a lacey carbon films supported by Cu-mesh grids and analyzed in a 300 kV TEM/STEM microscope. The instrument was equipped with an X-ray energy dispersive spectrometer (XEDS) and an electron energy-loss spectrometer (EELS) as well as bright-field (BF) and annular dark-field (ADF) STEM detectors to perform spot and line profile analyses.

[00163] The device substrates, *i.e.*, the sensor chips, were wire-bonded on a 24 pin ceramic package for the gas sensing measurements. The device characterization and the time dependent sensing measurements were done using an Agilent B1500A semiconductor parameter analyzer. Each sensor chip was placed in a custom-designed stainless steel test chamber of volume 0.73 cm^3 with separate gas inlet and outlet. The test chamber had a quartz window on top for UV excitation provided by a 25 W deuterium bulb (DH-2000-BAL, Ocean Optics) connected to a 600 μm diameter optical fiber cable with a collimating lens at the end for uniform illumination over the sample surface. The operating wavelength range of the bulb was 215 to 400 nm. The intensity at 365 nm measured using an optical power meter was 375 nW cm^{-2}. For all the sensing experiments regular breathing air (< 9 ppm of water) was used as the carrier gas. A wide range of concentrations from 1% to as low as 50 parts per billion (ppb) of various organic compounds were achieved with a specific arrangement of bubbler and mass flow controllers (MFCs). During the sensor measurements, the net flow (air + VOC mix) into the test chamber was set to a constant value of 20 sccm. After the sensor devices were exposed to the organic compounds, they were allowed to regain their baseline current with the air-chemical mixture turned-off, without purging or evacuating the test-chamber.

Results

[00164] **Figure 20** shows GaN nanowires with three different nominal thicknesses of TiO_2 coatings sputtered on them: 2 nm **(Figure 20, plate (a)**); 5 nm **(Figure 20, plate (b)**); and 8 nm **(Figure 20, plate (c)**). Rather sparse, well-defined clusters can be seen for both the 5 nm and 8 nm area-averaged sputtered coatings of TiO_2. The average size of these large clusters was about 15 nm. For the 8 nm sputtered coating, the coverage of the TiO_2 clusters is much denser. However, TEM studies revealed the presence of clusters with much smaller diameter (less than about 4 nm) on the nanowire surface.

[00165] Detection of XRD signal from the TiO_2 decorated GaN NWs was difficult due to the minuscule size and total volume of TiO_2 nanoclusters. We therefore prepared a 150 nm thick TiO_2 film by sputtering it onto a SiO_2 coated Si substrate at 300°C followed by anneal at 650°C for 45 s in argon. The processing conditions produced an identical morphology as in the TiO_2 decorated NW case. Referring to **Figure 21**, we identified from

the XRD that TiO_2 is in the single-phase anatase form. As-deposited TiO_2 films were found to be amorphous.

[00166] The XRD results agree with the TEM analysis on TiO_2 decorated GaN NWs, which revealed that upon annealing at 700°C for 30 s, the TiO_2 islands became partially crystalline, as shown in **Figure 22**. Three most common phases of TiO_2 are anatase, rutile, and brookite. Thermodynamic calculations predict that rutile is the most stable TiO_2 phase in the bulk state at all temperatures and atmospheric pressure (see Norotsky A *et al.* (1967) "*Enthalpy of Transformation of a High-Pressure Polymorph of Titanium Dioxide to the Rutile Modification*," Science 158:338; Jamieson J C and Olinger B (1969) "*Pressure-temperature studies of anatase, brookite, rutile, and TiO_2 (II); A discussion*," Am. Min. 54:1477-1480). However, comparative experiments with particle size showed that the phase stability might reverse with decreasing particle size, possibly due to the influence of surface free energy and surface stress (Zhang H Z and Banfield J. F (2000) "*Understanding polymorphic phase transformation behavior during growth of nanocrystalline aggregates: insights from TiO_2*," J. Phys. Chem. B 104:3481-3487). Anatase is the most stable phase when the particle size is less than about 11 nm, whereas rutile is most stable at sizes greater than about 35 nm. Although both rutile and anatase TiO_2 are commonly used as photocatalyst, anatase form shows greater photocatalytic activity for most reactions (Linsbigler A L *et al.* (1995) "*Photocatalysis on TiO_2 Surfaces: Principles, Mechanisms, and Selected Results*," Chem. Rev. 95:735-7; Tanaka K *et al.* (1991) "*Effect of crystallinity of TiO2 on its photocatalytic action*," Chem. Phys. Lett. 187:73-76). This is one consideration for sputtering nominally 8 nm of TiO_2 for the sensor fabrication.

[00167] Although we have sputtered 8 nm of TiO_2 for fabricating the hybrid sensors, for the TEM studies 20 nm of TiO_2 coating was utilized. The thick GaN nanowires prevented acquisition of any TEM diffraction from thinner TiO_2 coatings. The TEM results presented for 20 nm thick TiO_2 was representative of the clusters formed for 8 nm deposited TiO_2 in actual sensors. Typical morphologies of a 20 nm thick TiO_2 film sputtered on n-GaN nanowires and annealed at 700°C for 30 seconds are illustrated by TEM data in **Figure 22**. The TEM image in **Figure 22, plate (a)** shows 2 nm to 10 nm diameter individual TiO_2 particles non-uniformly distributed on the surface of a GaN nanowire. Some of the particles are identified by circles. Crystallinity of some nanoparticles observed is shown in the

HRTEM image in **Figure 22, plate (b)** with nanocrystallites on the edge of a GaN nanowire with the sputtered TiO_2. The FFT pattern from the boxed area is seen in exploded view in the upper left inset image, showing 0.35 nm lattice fringes which are consistent with a (101) reflecting plane of anatase but not available in hexagonal wurtzite-type GaN crystals.

[00168] Referring to **Figure 23, plate (a)**, a BF-STEM image shows 5 to 10 nm TiO_2 nanoparticles barely visible against the GaN nanowire. An ADF-STEM image of a TiO_2 island on a GaN nanowire is shown in **Figure 23, plate (b)**. The presence of TiO_2 was confirmed by analysis of selected areas as well as of individual particles using XEDS and EELS and nanoprobe capabilities. Referring to **Figure 23, plate (c),** the X-ray spectrum of an individual 5 nm TiO_2 particle (identified by the marked circle "A" in **Figure 23, plate (a)**) exhibits the TiKα peak at 4.51 keV and the weak Okα peak at 0.523 keV. The NKα peak at 0.39 keV and gallium lines (the GaL series at 1.0 keV to 1.2 keV) and the CKα peak at 0.28 keV are also identified. EEL spectrum acquired at Position "1" marked in **Figure 23, plate (b)** (the tip of a TiO_2-containing aggregate) exhibits the TiL edge at 456 eV and the OK edge at 532 eV and also the CK edge at 284 eV. A reference spectrum recorded at Position 2 marked in **Figure 23, plate (b)** (an edge of the GaN nanowire) reveals traces of titanium and oxygen with the NK edge at 401 eV and the GaL edge at 1115 eV, respectively.

[00169] **Figure 24** shows the current-voltage (I-V) characteristics of a GaN NW two-terminal device at different stages of processing. The I-V curves of the as-deposited devices were non-linear and asymmetric. The current decreased when the SiO_2 layer over the NW was etched. However, the current increased with the deposition of TiO_2 nanoclusters. Oxygen adsorption on the bare GaN nanowire surface can introduce surface states (Zywietz *et al.* (1999) "*The adsorption of oxygen at GaN surfaces*," Appl. Phys. Lett. 74:1695), resulting in the decrease of the nanowire conductivity. The devices annealed at 700°C for 30 seconds showed significant changes in their I-V characteristics with a majority of the devices exhibiting linear I-V curves. This is consistent with the fact that low resistance ohmic contacts to the nitrides require annealing at 700°C to 800°C (see Motayed A *et al.* (2003) "*Electrical, thermal, and microstructural characteristics of Ti/Al/Ti/Au multilayer ohmic contacts to n-type GaN*," J. Appl. Phys. 93(2):1087-1094).

[00170] **Figure 25** shows the photoconductance of a bare GaN NW device and the TiO_2 coated GaN NW device. The NW devices with TiO_2 nanoclusters showed almost two orders of magnitude increase in the current when exposed to UV light as compared to the similar diameter bare NW devices. Increase of photoconductance due to surface functionalization has been observed in ZnO nanobelts coated with different polymers (Lao C S *et al.* (2007) "*Giant Enhancement in UV Response of ZnO Nanobelts by Polymer Surface-Functionalization*," J. Am. Chem. Soc. 129:12096-12097). This enhancement of photoconductance is often attributed to the separation of photogenerated charge carriers by a surface depletion field, thereby increasing the lifetime of the photogenerated carriers. After the light is turned off, the photo current decays rapidly, but not to the dark current value, which is likely due to the persistent photoconductivity of the NWs (see Sanford N A *et al.* (2010) "*Steady-state and transient photoconductivity in c-axis GaN nanowires grown by nitrogen-plasma-assisted molecular beam epitaxy*," J. Appl. Phy. 107:034318).

[00171] The current through the bare GaN NW devices did not change when exposed to different VOCs mixed in air, even for concentrations as high as few percents. On the other hand, the TiO_2 coated hybrid devices responded even to the pulses of 20 sccm airflow. This is expected, considering that the conduction in most metal-oxides is affected by the presence of oxygen. The response of the TiO_2 nanocluster-GaN nanowire hybrid sensor to 1000 ppm of toluene in air is illustrated in **Figure 26**. Exposure to the VOC in the dark had no effect on the hybrid device. However, in presence of UV excitation, when 1000 ppm of toluene (mixed in air) was introduced into the gas chamber, the sensor photocurrent decreased dramatically to approximately 2/3 of its base value. After 100 seconds of gas exposure, the gas flow is turned off and the sensor is allowed to recover at room temperature without any additional purging. The repeatability of the sensing action of these hybrid sensors is evident from **Figure 26**.

[00172] Interestingly, the hybrid sensors did not respond when exposed to methanol, ethanol, isopropanol, chloroform, acetone, and 1,3-hexadiene, even for concentrations as high as several percent. Also, the photocurrent for these sensors increased with respect to air when exposed to toluene vapors, whereas for every other aromatic compound, the photocurrent decreased relative to air, as shown in **Figure 27, plate (a)**. More than twenty sensor devices were tested, with all exhibiting the same trend. In addition, the use of

toluene from different sources resulting in the same sensor behavior. **Figure 27, plate (b)** shows the response of a different device for 200 ppb concentrations of the same chemicals. It is clear that even for toluene concentration as low as 200 ppb, the relative change in photocurrent is the reverse of that observed with other chemicals. If the photocurrent in the presence of air for these sensors is used as their baseline calibration, then we can distinctly identify toluene from other aromatic compounds present in air using our hybrid devices. The response time is defined as the time taken by the sensor current to reach 90% of the response (I_f-I_0) when exposed to the analyte. The I_f is the steady sensor current level in the presence of the analyte, and I_0 is the current level without the analyte, which in our case is in the presence of air. The recovery time is the time required for the sensor current to recover to 30% of the response (I_f-I_0) after the gas flow is turned off (Garzella C *et al.* (2000) "*TiO_2 thin films by a novel sol-gel processing for gas sensor applications*," Sens. and Actuators B: Chemical 68:189-196). The response and recovery times for ppm levels of BTEX concentrations were ≈ 60 seconds and ≈ 75 seconds, respectively. The response and recovery times for ppb levels of concentrations were ≈ 180 seconds and ≈ 150 seconds, respectively. In contrast, conventional nanowire/nanotube sensors reported in the literature as working at room-temperatures had much longer response times in minutes (Leghrib R *et al.* (2010) "*Gas sensors based on multiwall carbon nanotubes decorated with tin oxide nanoclusters*," Sens. and Actuators B: Chemical 145:411-416; Balazsi C *et al.* (2008) "*Novel hexagonal WO3 nanopowder with metal decorated carbon nanotubes as NO2 gas sensor*," Sensors and Actuators B: Chemical 133:151-155; Kuang Q *et al.* (2008) "*Enhancing the photon- and gas-sensing properties of a single SnO2 nanowire based nanodevice by nanoparticle surface functionalization*," J. Phys. Chem. C 112:11539-11544; Lim W *et al. (*2008) "*Room temperature hydrogen detection using Pd-coated GaN nanowires*," Appl. Phys. Lett. 93:072109). Fast response and recovery times indicate fast adsorption and desorption, which is attributed to the enhanced reactivity of the nanoscale TiO_2 clusters.

[00173] The responses of two hybrid devices to different concentrations of toluene in air are shown in **Figure 28**. **Figure 28, plate (a)** shows the change of photocurrent of a 234 nm diameter device when exposed to toluene concentrations from 10000 ppm down to 100 ppm. **Figure 28, plate (b)** shows the photocurrent of a sensor device with 170 nm diameter wire for toluene concentrations from 1 ppm to 50 ppb.

[00174] Sensitivity is defined as $(R_{gas}-R_{air})/R_{air}$, where R_{gas}, R_{air} are the resistances of the sensor in the presence of the chemical-air mixture and in the presence of air, respectively. The sensitivity plots of a hybrid device for different VOCs tested are shown in **Figure 29**. The sensitivity plot emphasizes the ability of these hybrid sensors to reliably detect BTEX (benzene, toluene, ethylbenzene, chlorobenzene, and xylene), which are common indoor and outdoor pollutants with wide detection range (50 ppb to 1%).

EXAMPLE 2

[00175] The sensing behavior of three NWNC based hybrid sensors was compared: 1) GaN NW coated with TiO_2 NCs (hereafter referred to as GaN/TiO_2 NWNC hybrids); 2) GaN NW coated with TiO_2 and Pt multicomponent NCs (*i.e.*, GaN/(TiO_2-Pt) NWNC hybrids); and 3) GaN NW coated with Pt NCs (*i.e.*, GaN/Pt NWNC hybrids). It was found that sensors with TiO_2-Pt multicomponent NCs on GaN NW were only sensitive to methanol, ethanol, and hydrogen. Higher carbon-containing alcohols (such as n-propanol, iso-propanol, n-butanol) did not produce any sensor response. These sensors had the highest sensitivity towards hydrogen. Prior to the Pt deposition, the GaN/TiO_2 NWNC hybrids did not exhibit any response to alcohols, however they detected benzene and related aromatic compounds such as toluene, ethylbenzene, xylene, and chlorobenzene mixed with air. The GaN/Pt hybrids only showed sensitivity to hydrogen and not to methanol or ethanol. The sensitivity of GaN/Pt hybrids towards hydrogen was lower compared to the GaN/(TiO_2-Pt) hybrids.

Materials and Methods

[00176] GaN NWs utilized for this study were *c*-axis, *n*-type (Si-doped), grown by catalyst-free molecular beam epitaxy as described by Bertness K A *et al.* (2008), *supra*, J. Crystal Growth 310(13):3154-3158. Post-growth device fabrication was done by dielectrophoretically aligning the nanowires on 9 mm × 9 mm sapphire substrates. The details of the device fabrication are set forth in Example 1. After fabrication of two-terminal GaN NW devices, the TiO_2 NCs were deposited on the GaN NW surface using RF magnetron sputtering. The deposition was done at 325°C with 50 standard cubic centimeters per minute (sccm) of Ar flow, and 300 W RF power. The nominal deposition rate was about 0.24 Å/s. Thermal annealing of the complete sensor devices (GaN NW with

TiO_2 nanoclusters) was done at 700°C for 30 seconds in a rapid thermal processing system. For TiO_2-Pt composite NCs, the Pt was sputtered using DC sputtering after annealing of the TiO_2 clusters on GaN NW. The Pt sputtering was done with an Ar flow of 35 sccm, at a pressure of 1.3 Pa and power of 40 W for 10 seconds. For the Pt/GaN devices Pt was sputtered on bare GaN NWs after annealing the ohmic contacts at 700°C for 30 seconds. Additional lithography was performed to form thick metal bond pads with Ti (40 nm) and Au (200 nm). The device substrates, *i.e.*, the sensor chips, were wire-bonded on a 24 pin ceramic package for the gas sensing measurements.

[00177] The microstructure and morphology of the sputtered TiO_2 films used for the fabrication of the sensors were characterized by high-resolution transmission and scanning transmission electron microscopy (HRTEM/STEM), selected-area electron diffraction (SAED), and field-emission scanning electron microscopy (FESEM). For the TEM characterization, the GaN NWs were dispersed on 10 nm thick carbon films supported by Mo-mesh grids, followed by the deposition of TiO_2 NCs and annealing, and subsequent Pt deposition. The samples were analyzed in a FEI Titan 80-300 TEM/STEM microscope operating at 300 kV accelerating voltage and equipped with S-TWIN objective lenses, which provided 0.13 nm (STEM) and 0.19 nm (TEM) resolution by points. The instrument also had a Gatan CCD image acquisition camera, bright-field (BF), ADF and high-angle annular dark-field (HAADF) STEM detectors to perform spot, line profile, and areal compositional analyses using an EDAX 300 kV high-performance Si/Li X-ray energy dispersive spectrometer (XEDS).

[00178] The as-fabricated sensors were placed in a custom designed gas chamber for gas exposure measurements. The device characterization and the time dependent sensing measurements were done using an Agilent B1500A semiconductor parameter analyzer. The gas sensing experiments have been performed by measuring the electrical conductance of the devices upon exposure to controlled flow of air/chemical mixture in presence of UV excitation (25 W deuterium bulb operating in the 215 nm to 400 nm range). For all the sensing experiments with chemicals, breathing air (< 9 μmol/mol of water) was used as the carrier gas. For the hydrogen sensing we used high-purity nitrogen as the carrier gas. After the sensor devices were exposed to the organic compounds and

hydrogen, they were allowed to regain their baseline current with the air-chemical mixture turned-off, without purging or evacuating the test-chamber.

Results

Morphological and Structural Characterization of NWNC Hybrids

[00179] It was challenging to measure the sizes and shapes of small TiO_2 and Pt particles on the surfaces GaN NWs from greyscale TEM images due to: a) 270 nm to 300 nm thickness of the NWs used in the devices and variations of thickness and curvature across the structure; b) diffraction contrast induced particularly by bending of the wires - even similar particles could appear as having different intensities, while local thickness variations of the carbon support film could result in variable contrast affecting the mean intensity values of the particles; c) overwhelming domination of electron diffraction in SAED from the GaN NW over the diffraction from TiO_2 and Pt nanoparticles. To overcome these problems, TEM imaging was conducted under minimal beam intensity conditions close to the Scherzer defocus at highest available accelerating voltage of 300 kV using both stationary beam (bright-field TEM/SAED, phase-contrast high-resolution TEM) and scanning beam (STEM/XEDS) modes. Areas for analyses were selected near the wire's edges and on the amorphous carbon support film in the vicinity of the NWs.

[00180] **Figure 30** shows HRTEM micrographs of a GaN NW on a thin amorphous carbon support films with TiO_2 coating, before and after the Pt deposition. The deposited TiO_2 layer formed an island-like film, where 10 nm to 50 nm partially aggregated particles (see **Figure 30, plate (a)**) were often interconnected into extended two-dimensional networks. This was consistent with SAED and compositional analyses of deposited TiO_2 films indicating a mixture of polycrystalline anatase and rutile and of the same mixture plus fcc Pt nanoparticles (**Figure 30, plate (b)**), respectively. Pt crystalline particles with 1 to 5 nm size were randomly distributed on the surfaces of TiO_2 islands and sometimes were partially coalesced forming elongated aggregates. In the latter case, significant thickness of the GaN NWs made it difficult to visualize TiO_2 deposits due to the limited contrast difference between TiO_2 and GaN and presence of multiple heavy Pt particles. In spite of these limitations, detailed HRTEM and HR-STEM observations revealed 0.35 nm (101) hcp lattice fringes belonging to anatase (see **Figure 30, plate (b)**, upper left inset) and 0.23 nm

to 0.25 nm (111) and 0.20 nm to 0.22 nm (200) fcc lattice fringes belonging to Pt nanocrystallites, respectively, as well as amorphous-like Pt clusters with diameters around 1 nm or less (see **Figure 31, plates (a) and (b)**).

[00181] In the **Figure 31**, HAADF-STEM image shows 1 nm to 5 nm diameter bright Pt nanoparticles and barely visible TiO_2 islands (medium grey) randomly distributed near the edge of the nanowire. The presence of both TiO_2 and Pt nanocrystallites was confirmed by the analysis of selected areas using XEDS nanoprobe capabilities.

Current-Voltage (I-V) Characteristics of NWNC Hybrids in Dark

[00182] **Figure 32** shows the I-V characteristics of the GaN/(TiO_2-Pt) and GaN/Pt hybrid sensor devices at different stages of processing. A plan-view SEM image of an exemplary sensor device is shown in the inset of **Figure 32, plate (b)** for representation purposes. The I-V curves of the as-fabricated GaN NW two-terminal devices were non-linear and asymmetric. A small increase in the positive current after the deposition of TiO_2 nanoclusters (curve 2) can be attributed to decreased surface depletion of the GaN NW due to passivation of surface states, and/or the high temperature deposition (325°C) of the nanoclusters initiating ohmic contact formation. The devices annealed at 700°C for 30 s after the deposition of TiO_2 NCs showed significant change in their I-V characteristics with a majority of the devices exhibiting linear I-V curves. Interestingly, Pt NC deposition on TiO_2 coated GaN NWs further increased the conductivity of the nanowire. This is due to the fact that the Pt clusters depleted the TiO_2 clusters by removing free electrons. Increased depletion in the TiO_2 clusters due to Pt would decrease TiO_2 induced depletion in the GaN NW, leading to an increase in the NW current. With the Pt/GaN hybrids, the current decreases followed by the deposition of Pt (see **Figure 32, plate (b))** as expected due to the depletion region formed in the NW under the metal clusters.

[00183] The nature of the depletion region formed by the nano-sized metal clusters on a semiconductor may be determined by Zhdanov's model. **Figure 33** shows the calculated zero-bias depletion depth produced in GaN and TiO_2 respectively, as a function of the Pt cluster radius according to Equation (1). For calculating the depletion depth we assumed the effective conduction band density of states in TiO_2 as 3.0×10^{21} cm^{-3} and point-defect

related donor concentration as 1.0×10^{18} cm^{-3} [43,44]. The electron concentration in the GaN NWs was measured to be 1×10^{17} cm^{-3} in a separate experiment.

[00184] **Figure 33** indicates that even a single Pt NC of 2 nm radius can significantly deplete a 10 nm (average size) TiO_2 cluster. The effect of TiO_2 depletion on GaN NW is difficult to determine as it could be influenced by numerous factors including interface states and particle geometry. Given the very high density of TiO_2 clusters on the NW surface (see **Figure 31, plate (b)**), it is clear that the Pt particles mostly reside on the surfaces of TiO_2 NCs. However, from **Figure 33** we can see that when Pt NCs are directly on GaN, they deplete the carriers in an even larger region in the GaN NW. This qualitatively explains the relatively larger change in current observed when Pt NCs were deposited on bare GaN NWs as compared to the change in current when Pt NC were deposit on the TiO_2 -coated NWs.

Comparative Sensing Behavior of GaN/(TiO_2-Pt), GaN/Pt and GaN/TiO_2 NWNC Hybrid Sensors

[00185] The photocurrent through the bare GaN NW devices did not change when exposed to different chemicals mixed in air, even for concentrations as high as 3%. In contrast, the TiO_2-coated hybrid devices responded even to the pulses of 20 sccm airflow in the presence of UV excitation. The response of the TiO_2 NC-coated GaN nanowire hybrid sensors to different concentrations of benzene, toluene, ethylbenzene, chlorobenzene, and xylene in air is discussed above. The GaN/TiO_2 hybrids showed no response when exposed to other chemicals such as alcohols, ketones, amides, alkanes, nitro/halo-alkanes, and esters.

[00186] Remarkably, after the deposition of Pt nanoclusters on the GaN/TiO_2 hybrids, the sensors were no longer sensitive to benzene and other aromatic compounds, but responded only to hydrogen, methanol, and ethanol. In addition, the GaN/(TiO_2-Pt) hybrids showed no response when exposed to higher carbon-containing (C>2) alcohols such as n-propanol, iso-propanol, and n-butanol. **Figure 5** shows the change of photocurrent of a GaN/(TiO_2-Pt) sensor in the presence of 20 sccm air flow of air mixed with 1000 μmol/mol (ppm) of methanol, ethanol, and water, respectively, and 20 sccm of nitrogen flow mixed with 1000 μmol/mol (ppm) hydrogen. The change in the photocurrent of the sensor when

20 sccm of breathing air is flowing through the test chamber serves as a reference for calculating the sensitivity of the sensors. The sensitivity is defined as $(R_{gas}-R_{air})/R_{air}$, where R_{gas} and R_{air} are the resistances of the sensor in the presence of the analyte-air mixture and in the presence of air only, respectively (R_{air} is replaced with $R_{nitrogen}$ for hydrogen sensing experiments).

[00187] The GaN/TiO_2 hybrids without Pt showed no response to hydrogen and the alcohols. Interestingly, when Pt NC-coated GaN NW hybrids (GaN/Pt) with the same nominal thickness were tested, they showed very limited sensitivity only to hydrogen and not to any alcohols. The comparative summary of the sensing behavior of the three different hybrids are presented in **Figure 34**.

[00188] The response of the GaN/(TiO_2-Pt) NWNC sensor to different concentrations of methanol in air is shown in **Figure 35, plate (a)**. **Figure 35, plate (b)** shows the response to different concentrations of hydrogen in nitrogen for the same GaN/(TiO_2-Pt) NWNC sensor device. The sensor response is much higher for hydrogen compared to methanol and ethanol. The response time is also much shorter for hydrogen as compared to methanol, and the sensor photocurrent saturates after initial 20 s exposure.

[00189] The response time was defined as the time taken by the sensor current to reach 90% of the response (I_f-I_0) when exposed to the analyte. The I_f is the steady sensor current level in the presence of the analyte, and I_0 is the current level without the analyte, which in our case is in the presence of 20 sccm of air flow. The recovery time is the time required for the sensor current to recover to 30% of the response (I_f-I_0) after the gas flow is turned off (see Garzella C *et al.* (2000) Sensors and Actuators B: Chemical 68:189-196). The response time for hydrogen was ≈ 60 seconds, whereas the response time for ethanol and methanol was ≈ 80 seconds. The sensor recovery time for hydrogen was ≈ 45 seconds and the recovery times for ethanol, methanol was ≈ 60 seconds and ≈ 80 seconds, respectively. For comparison, Wang *et al.* demonstrated a conventional ZnO NW-based hydrogen sensor with a response time of 10 minutes for 4.2% sensitivity (Wang H T *et al.* (2005) "*Hydrogen-selective sensing at room temperature with ZnO nanorods*," Appl. Phys. Lett. 86:243503).

[00190] The sensitivity plot of a GaN/(TiO_2-Pt) hybrid device for the various analytes tested is shown in **Figure 36, plate (a)**. Note that the lowest concentration detected for methanol and hydrogen (1 ppm or μmol/mol) is not the sensor's detection limit, but a system limitation. It can be seen that the sensor is more sensitive to methanol than ethanol for concentrations ≥1000 μmol/mol (ppm), and the relative sensitivity switches for concentrations of 500 μmol/mol (ppm) and below. Similar behavior is observed with twenty unique devices, possibly due to difference in surface coverage of the different alcohols over the concentration range. **Figure 36, plate (b)** is a comparative plot showing the sensitivity of GaN/(TiO_2-Pt) and GaN/Pt hybrid sensors to hydrogen in nitrogen. The GaN/Pt hybrid devices showed relatively low sensitivity with detection limit of 50 μmol/mol (ppm), below which the devices stopped responding. The gas exposure time was also increased to 200 seconds for the GaN/Pt devices to obtain increased response compared to 100 seconds for the GaN/(TiO_2-Pt) GaN devices. The sensitivity of the GaN/(TiO_2-Pt) sensors was greater for alcohols and hydrogen when compared with the same concentrations of water in air, which thus enables their use in high-humidity conditions.

[00191] **Table X** and **Table XI** compare the performance of the sensor devices of the present invention with sensors disclosed in the most recent literature in terms of operation temperature, carrier gas, lower detection limit, and response/recovery times. The comparison indicates that the sensors devices of the present invention exhibit an excellent response to very low concentrations of analytes (100 ppb for ethanol and 1 ppm for hydrogen) at room temperature, with air as the carrier gas. The testing conditions closely resembled real-life conditions, which underlines the significance of the disclosed sensors. The response and recovery times were also lower for the disclosed sensors compared to the other conventional sensors, as shown in **Tables X** and **XI**.

TABLE X: Performance of GaN/(TiO_2-Pt) NWNC hybrid sensors to ethanol in comparison with conventional sensors

	Response/ Recovery Time	Lower Detection Limit	Carrier Gas	Testing Temperature
Sensor of Present Invention	**80 s / 75 s**	**100 ppb with 1% sensitivity[4]**	**air**	**Room temperature (RT)**
CNT[1]/SnO_2 core shell nanostructures	1 s / 10 s	10 ppm	air	300°C
MWCNTs[2]/ $NaClO_4$/ polypyrrole	20s / 20s	18,000 ppm	air	RT
Metal-CNT hybrids	~2 min / (recovery time not reported)	500 ppb with sensitivity < 1%	N_2 in a vacuum test chamber	RT
V_2O_5 nanobelts	50s / 50s	5 ppm	air	150°C - 400 °C
ZnO nanorods	3.95 min / 5.3 min	10 ppm	Synthetic air	125°C -300 °C
ZnO nanowires	10s / 55s	1 ppm	air	220°C
ITO[3] nanowires	2 s / 2 s	10 ppm	air	400°C
SnO_2 nanowires	2 s / 2 s	10 ppm	air	300°C

[1] Carbon nanotubes
[2] Multiwall carbon nanotubes
[3] Indium tin oxide
[4] Sensitivity values for sensors with lowest limit similar to disclosed results were compared.

TABLE XI: Performance of GaN/(TiO_2-Pt) NWNC hybrid sensors to hydrogen in comparison with conventional sensors

	Response/recovery times	Lower detection limit	Testing Temperature
Sensor of Present Invention	**60 s / 45 s**	**1 ppm with sensitivity of 4%**	**RT**
CNT films	5 min / 30 s	10 ppm	RT
SWCNT/ SnO_2	2 s / 2 s	300 ppm	250 °C
Pd/CNTs	5 min / 5 min	30 ppm with sensitivity of 3%	RT
Pd/ Si NWs	1 hr / 50 min	3 ppm	RT
Pt doped SnO_2 NWs	2 min / 10 min	100 ppm	100 °C

[00192] The present results indicate the unique ability to tailor the selectivity of NWNC chemical sensors. With infinite combinations of metal and metal-oxide composite clusters available, there is a huge potential for sensor designs targeted for a multitude of applications.

EXAMPLE 3

[00193] Alcohol sensors using gallium nitride (GaN) nanowires (NWs) functionalized with zinc oxide (ZnO) nanoparticles are demonstrated. These sensors operate at room temperature, are fully recoverable, and demonstrate a response and recovery time on the order of 100 seconds. The sensing is assisted by UV light within the 215-400-nm band and with the intensity of 375 nW/cm^2 measured at 365 nm. The ability to functionalize an inactive NW surface, with analyte-specific active metal-oxide nanoparticles, makes this sensor suitable for fabricating multianalyte sensor arrays.

Methods and Materials

[00194] Si-doped *c*-axis n-type GaN NWs were grown using catalyst-free molecular beam epitaxy on Si (III) substrate as described in Bertness K A *et al.* (2008), *supra, J. Cryst. Growth* 310(13):3154-3158. The NW diameter and length were in the ranges of 250-350 nm and 21-23 μm, respectively. The GaN NWs were detached from the substrate by sonication in isopropanol and dielectrophoretically aligned across the pre-patterned

electrodes. The electrodes were fabricated using photolithography followed by deposition of a metal stack of Ti (40 nm)/Al (420 nm)/Ti (40 nm). Thick bottom electrodes ensure the free suspension of the NWs. For the formation of ohmic contacts to the NW ends, the top metal contacts were fabricated using a metal stack of Ti (70 nm)/Al (70 nm)/Ti (40 nm)/Au (40 nm), as described in A. Motayed *et al.* (2003), *supra, J. Appl. Phys.* 93(2):1087-1094. Rapid thermal anneal (RTA) was performed at 700°C for 30 seconds in argon atmosphere to promote the formation of ohmic contacts and to reduce the stress in the thick bottom electrodes. Finally, ZnO nanoparticles were sputter deposited on the NW device with an RF power of 300 W in 60 standard cubic centimeters per minute (sccm) of oxygen and 40 sccm of argon gas flow at room temperature. Deposition time of 160 seconds was found to be optimal for the formation of uncoalesced oxide nanoparticles.

[00195] The microstructure of the devices was characterized using a scanning electron microscope (SEM) and X-ray diffraction (XRD). Due to the small size of the nanoparticles, the XRD signal from ZnO was not detected. Thus, the analysis was performed on a 300-nm-thick ZnO film sputter deposited on Si (111) substrate with the assumption that the ZnO crystallinity is similar for nanoparticles and for thin films deposited at the identical conditions. Current-voltage characteristics of the devices were also measured to determine the nature of the NW-metal contacts.

[00196] For the gas sensing measurements, a device was placed inside the stainless steel chamber with an inlet and an outlet for the analyte vapors. The chamber, with a volume of 0.73 cm^3, has a quartz window on the top to facilitate exposure of the device to UV light. The wavelength of the light bulb was confined to the range of 215-400 nm; the intensity recorded at 365 nm was 3.75 nW/cm^2. The sensor baseline was established at a constant flow of 40 sccm of breathing air under illumination. For sensing experiments, 40 sccm of the mixture of the breathing air and analyte vapor was passed through the chamber. All sensing measurements were performed in the presence of UV light and 5-V dc voltage bias applied across the device terminals. Negligible or no chemiresistive response was observed for all the chemicals in the absence of the illumination.

Results and Properties

[00197] **Figure 6, plate (a)** shows a SEM image of a device with a single GaN NW suspended across the metal electrodes. **Figure 6, plate (b)** shows the ZnO nanoparticles on the facets of a GaN NW. The current-voltage characteristics of the device measured before and after RTA are shown in **Figure 6, plate (c)**. As shown in **Figure 6, plate (d),** XRD reveals that the sputter-deposited ZnO is crystalline and highly (0002) textured.

[00198] Referring to **Figure 8** sensor response to air and nitrogen was evaluated. **Figure 8, plate (a)** shows the device response to the different flow rates of breathing air. As seen therein, device conductance decreases upon exposure to the breathing air, and the decrease is proportional to the flow rate. Opposite behavior (*i.e.*, an increase in conductivity) is observed when the device is exposed to nitrogen gas as seen in **Figure 8, plate (b)**.

[00199] Referring to **Figure 7**, sensor response to alcohols and other analytes was evaluated. When exposed to alcohol vapors (methanol, ethanol, *n*-propanol, isopropanol, *n*-butanol, and isobutanol), the devices showed an increase in conductivity with maximum sensitivity toward methanol. **Figure 7** shows the device response to 500-μmol/mol (ppm) methanol vapor in breathing air.

[00200] For the isomers of an alcohol, the sensitivity decreases with branching in the carbon chain. Hence, as shown in **Figure 7** (inset, bottom left), the sensitivity toward isobutanol is less than that toward n-butanol. As shown in **Figure 7** (inset, bottom right), the devices show a negligible response to possible interfering chemicals such as benzene and hexane, whereas the sensitivity toward 100 μmol/mol (ppm) of ethanol is similar to the sensitivity toward 1000 μmol/mol (ppm) of acetone. Ethanol vapor concentration down to 100 nmol/mol (ppb) was successfully detected, and the detection of even lower concentrations is possible with alternative measurement setup.

EXAMPLE 4

[00201] A hybrid chemiresistive architecture, utilizing nanoengineered wide-bandgap semiconductor backbone functionalized with multicomponent photocatalytic nanoclusters of

metal-oxides and metals was demonstrated. These sensors operated at room-temperature via photoenabled sensing.

Etching of Semiconductor Nanostructures

[00202] For real-time nanosensors, successful etching of semiconducting nanostructures, which is characterized by smooth surfaces with minimal sub-surface damage and appropriate side-wall profiles, is desired. This requires overcoming the strong chemical bond energy in widegap semiconductors, and also adjusting the process conditions to overcome inherent defects in epitaxially grown films on non-native substrates using heteroepitaxy. Otherwise, an un-optimized etching process may result in surface morphologies that include pits and/or pillars.

[00203] An Inductively Coupled Plasma-Reactive Ion Etching (ICP-RIE) process with $Cl_2/Ar/N_2$ chemistry is provided, with an etch rate of about 100 nm/min for GaN. The dry etching process may be optimized using X-ray photoelectron spectroscopy (XPS), scanning electron microscopy (SEM), photoconductivity measurements, and photoluminescence (PL) measurements.

Fabrication Detail

[00204] Prior to dry etching, semiconductor wafer surfaces are treated with standard RCA cleaning procedures. As a mask for selective etching, a 500-nm-thick SiO_2 film is deposited by standard plasma-enhanced chemical vapor deposition (PECVD). Etching patterns are defined by deep UV lithography using a proximity aligner capable of generating 300 nm feature sizes. Electron beam deposition of Ni (~20 nm) followed by lift-off is carried out to complete the formation of mask for the SiO_2 etch.

[00205] Direct metal-masking of the semiconductor is not done in order to avoid un-intentional doping of the metal during the etch process. The ICP-RIE etching is performed using the following procedure. GaN etch is accomplished using ICP etching with a $Cl_2/N_2/Ar$ (25:5:2) gas mixture under a pressure of 5 mTorr with varying ICP etching power and radio frequency (RF) power. For nitrides, Chlorine-based etches are used because it has been shown to produce vertical sidewalls due to the ion assisted etching mechanism with smooth

profiles. Temperature of the etch is a parameter that provides control of the sidewall angle. With low-temperature etch, the sub-surface damage may also be controlled.

[00206] Each sample is treated with a standard RCA clean before the activation annealing, the etching, and the measurements. Etching profile and surface morphology may be investigated by SEM. The surface chemical properties of semiconductor after the etch is characterized using an XPS system and PL measurements performed at room temperature. The electrical properties of etched semiconductor backbone are characterized photocurrent measurements. Photocurrent intensity is a direct measure of the surface recombination, *i.e.*, higher photocurrent intensity will indicate less surface defect non-radiative recombination, hence less sub-surface damage. For GaN, Ti/Al/Ti/Au (70 nm/70 nm/50 nm/50 nm) ohmic electrodes are formed at both ends of the backbone nanostructures and then annealed at temperatures from 500C to 800C for ~1 min. The nanodevices are then functionalized with different metal and metal-oxide nanoclusters using reactive sputtering.

[00207] A schematic representation of an exemplary fabrication flow for semiconductor-nanocluster based gas sensors according to the present invention is shown in **Figure 37**. As shown, the fabrication flow provides for parallel architecture, with multiple parallel sections. The multi-analyte arrays can be created on one single chip (10 mm × 10 mm) by depositing clusters of different components on different micro-scale devices. This is possible due to low-temperature sputtering process used for the cluster deposition. An array of multiple sensors (*e.g.* for detecting NO_x, SO_x, CO_x, NH_3, and H_2O) may be fabricated all on one single chip. **Figure 38** shows exemplary inter-digitated GaN devices on Si and sapphire substrates formed using top-down processes (e.g., such as shown in **Figure 37**).

EXAMPLE 5

[00208] Protection against explosive-based terrorism may be achieved by large-scale production of nano-sensor arrays that are inexpensive, highly sensitive and selective with low response and recovery times. In this study, the selective response of GaN nanowire/TiO_2 nanocluster hybrids to nitroaromatic explosives, including trinitrotoluene (TNT), dinitrotoluene (DNT), nitrotoluene (NT), dinitrobenzene (DNB) and nitrobenzene

(NB) at room temperature is demonstrated. The sensors detected between 0.5 ppb and 8 ppm TNT with good selectivity against interfering compounds such as toluene. The sensitivity of 1 ppm of TNT is ≅10% with response and recovery times of ≅30 seconds.

[00209] *N*-type (Si doped) GaN nanowires functionalized with TiO_2 nanoclusters were utilized for selectively sensing nitro-aromatic explosive compounds. GaN is a wide-bandgap semiconductor (3.4 eV) with unique properties. Its chemical inertness and capability of operating in extreme environments (high-temperatures, presence of radiation, extreme pH levels) is highly desirable for sensor design. TiO_2 is a photocatalytic semiconductor with bandgap energy of 3.2 eV (anatase phase). The TiO_2 nanoclusters were selected to act as nanocatalysts to increase the sensitivity, lower the detection time, and enable the selectivity of the structures to be tailored to a target analyte (*e.g.*, the most common explosives, trinitrotoluene (TNT) and other nitro-aromatics).

Materials and Methods

[00210] GaN nanowires were grown by Molecular Beam Epitaxy method as described in Bertness K A *et al.* (2008), *supra*, J. Crystal Growth 310(13):3154-3158. The nanowires are aligned on a pre-patterned substrate using dielectrophoresis. Details of the device fabrication are reported in Aluri G S *et al.* (2011) "*Highly selective GaN-nanowire/ TiO_2-nanocluster hybrid sensors for detection of benzene and related environment pollutants*," Nanotechnology 22(29):295503. After fabrication of two-terminal GaN NW devices, the TiO_2 NCs were deposited on the GaN NW surface using RF magnetron sputtering. The deposition was done at 325°C with 50 standard cubic centimeters per minute (sccm) of Ar flow, and 300 W RF power. The nominal deposition rate was about 0.24 Å/s. Thermal annealing of the complete sensor devices (GaN NW with TiO_2 nanoclusters) was done at 700°C for 30 seconds in a rapid thermal processing system. The device substrates, *i.e.*, the sensor chips, were wire-bonded on a 24 pin ceramic package for the gas sensing measurements.

[00211] The microstructure and morphology of the sputtered TiO_2 films used for the fabrication of the sensors were characterized by high-resolution transmission and scanning transmission electron microscopy (HRTEM/STEM), selected-area electron diffraction (SAED), and field-emission scanning electron microscopy (FESEM). For the TEM

characterization, the GaN NWs were dispersed on 10 nm thick carbon films supported by Mo-mesh grids, followed by the deposition of TiO_2 NCs and annealing and subsequent Pt deposition. The samples were analyzed in a FEI Titan 80-300 TEM/STEM microscope operating at 300 kV accelerating voltage and equipped with S-TWIN objective lenses, which provided 0.13 nm (STEM) and 0.19 nm (TEM) resolution by points. The instrument also had a Gatan CCD image acquisition camera, bright-field (BF), ADF and high-angle annular dark-field (HAADF) STEM detectors to perform spot, line profile, and areal compositional analyses using an EDAX 300 kV high-performance Si/Li X-ray energy dispersive spectrometer (XEDS).

[00212] The as-fabricated sensors were placed in a custom designed gas chamber for gas exposure measurements. Detailed description of the experimental setup and experimental conditions is provided in Aluri G S *et al.* (2011), *supra*, Nanotechnology 22(29):295503. The device characterization and the time dependent sensing measurements were done using an Agilent B1500A semiconductor parameter analyzer. The gas sensing experiments were performed by measuring the electrical conductance of the devices upon exposure to controlled flow of air/chemical mixture in presence of UV excitation (25 W deuterium bulb operating in the 215 nm to 400 nm range). For all the sensing experiments with chemicals, breathing air (<9 μmol/mol of water) was used as the carrier gas. After the sensor devices were exposed to the aromatic compounds, they were allowed to regain their baseline current with the air-chemical mixture turned-off, without purging or evacuating the test-chamber.

Results

Morphological and Structural Characterization of NWNC Hybrids

[00213] TEM imaging was conducted under minimal beam intensity conditions close to the Scherzer defocus at highest available accelerating voltage of 300 kV using both stationary beam (bright-field TEM/SAED, phase-contrast high-resolution TEM) and scanning beam (STEM/XEDS) modes. Areas for analyses were selected near the wire's edges and on the amorphous carbon support film in the vicinity of the NWs. **Figure 39** shows HRTEM micrographs of a GaN NW on a thin amorphous carbon support films with TiO_2 coating. The deposited TiO_2 layer formed an island-like film, where 10 nm to 50 nm

partially aggregated particles (circled areas in **Figure 39**) were often interconnected into extended two-dimensional networks. This was consistent with SAED and compositional analyses of deposited TiO_2 films indicating a mixture of polycrystalline anatase and rutile phases. Despite the limited contrast difference between TiO_2 and GaN, detailed HRTEM and HR-STEM observations revealed 0.35 nm (101) hcp lattice fringes belonging to anatase.

Current-Voltage (I-V) Characteristics of NWNC Hybrids

[00214] Referring to **Figure 40**, I-V characteristics of a GaN NW two-terminal device at different stages of processing are shown. The I-V curves of the as-deposited devices were non-linear and asymmetric (with a low current of 35 nA). However, the current increased (to a 100 nA) with the deposition of TiO_2 nanoclusters. This may be attributed to decreased surface depletion of the GaN NW due to passivation of surface states, and/or the high temperature deposition (325°C) of the nanoclusters initiating ohmic contact formation. The devices annealed at 700°C for 30 seconds showed significant changes in their I-V characteristics with a majority of the devices exhibiting linear I-V curves. This is consistent given low resistance ohmic contacts to the nitrides require annealing at 700°C-800°C.

Sensing Behavior of GaN/TiO_2 NWNC Hybrid Sensors

[00215] The photocurrent through the bare GaN NW devices did not change when exposed to different chemicals mixed in air, even for concentrations as high as 3%. In contrast, the TiO_2-coated hybrid devices responded even to the pulses of 20 sccm airflow in the presence of UV excitation. The response of the TiO_2 NC-coated GaN nanowire hybrid sensors to different concentrations of benzene, toluene, ethylbenzene, chlorobenzene, and xylene in air is discussed above. The GaN/TiO_2 hybrids showed no response when exposed to other chemicals such as alcohols, ketones, amides, alkanes, nitro/halo-alkanes, and esters.

[00216] The response of the TiO_2 coated hybrid devices when exposed to a concentration of 100 ppb of the aromatics and nitro-aromatics in air can is shown in **Figure 41, plate (a)**. The photocurrent for these sensors increased with respect to air when

exposed to toluene vapors, whereas for every other aromatic compound the photocurrent decreased relative to air. The response is observed to increase with the increase in the number of nitro groups attached to the aromatic compound. The response of the hybrid device to different concentrations of TNT in air from 8 ppm down to as low as 500 ppt is shown in **Figure 41, plate (b)**. The response time is defined as the time taken by the sensor current to reach 90% of the response (I_f-I_0) when exposed to the analyte. The I_f is the steady sensor current level in the presence of the analyte, and I_0 is the current level without the analyte, which in this case is in the presence of air. The recovery time is the time required for the sensor current to recover to 30% of the response (I_f-I_0) after the gas flow is turned off. The response and recovery times of the nano-devices to different concentrations of TNT are ≅30 seconds. The response and recovery times of the rest of the compounds varied from ≅60 seconds to ≅75 seconds.

[00217] The sensitivity is defined as (R_{gas}-R_{air})/R_{air}, where R_{gas} and R_{air} are the resistances of the sensor in the presence of the chemical-air mixture and in presence of air, respectively. The sensitivity plot of a hybrid device for the different aromatics and nitro-aromatics tested is shown in **Figure 42**. The sensitivity ((R_{gas}-R_{air})/R_{air}) for 1 ppm of TNT is ≅10%. The devices exhibit a very highly sensitive and selective response to TNT when compared to interfering compounds like toluene. Toluene shows an increase in response with respect to air, whereas TNT shows a decrease when compared to air. The plot identifies the sensor's ability to sense wide concentration ranges of the indicated chemicals. The sensitivity of two different devices (device 1--D1; device 2--D2) to the different aromatic compounds can be seen in **Figure 43**.

[00218] As discussed above, oxygen vacancy defects (Ti^{3+} sites) on the surface of TiO_2 are the "active sites" for the adsorption of species like oxygen, water, and organic molecules. In the presence of UV excitation with an energy above the bandgap energy of anatase TiO_2 (3.2 eV) and GaN (3.4 eV), electron-hole pairs are generated both in the GaN NW and in the TiO_2 cluster. Photogenerated holes in the nanowire tend to diffuse towards the surface due to surface band bending. This effect of separation of photogenerated charge carriers results in a longer lifetime of photogenerated electrons, which in turn enhances the photoresponse of the nanowire devices in general. Since the nitro-aromatic compounds are highly electronegative, they tend to attract electrons from other molecules

through charge transfer. This charge transfer between the adsorbed species on the TiO_2 nanocluster, and the nitro groups in the nitro-aromatic compounds increases the width of the depletion region in the nanowire device, reducing the current.

[00219] The potential of the disclosed nanostructure-nanocluster hybrids for next-generation nano-sensors having the capability to detect explosive compounds quickly and reliably is clearly demonstrated. The GaN/ TiO_2 nanowire nanocluster hybrid devices tested detected trace amounts of aromatic and nitro-aromatic compounds in air at room temperature with very low response and recovery times (≅ 30 seconds). The nitro-aromatic explosives like TNT are selectively detectable even for concentrations as low as 500 ppt.

Digital C02 Sensor On Chip

[00220] Sensing of carbon dioxide can be challenging as, unlike other active species, activation and splitting of the CO2 molecule on an oxide surface at typical room temperatures are challenging. As CO2 is nonpolar and has two double bonds, its activation generally requires high temperature/pressure conditions and/or active reductants, such as hydrogen. Solid-state bases, such as alkaline earth metals and alkaline earth metal oxides, and numerous studies on the formation of 'bent' CO2δ– configurations on their surfaces have been reported. However, formation of these CO2δ– species alone does not lead to CO2 splitting. As mentioned above in the Background section, NDIR based CO2 sensors have issues with cost and calibration.

[00221] Alternatively, according to the embodiments described below, CO2 can be activated under ambient conditions with the help of a solid-state catalyst, the role of which is to adsorb CO2 molecules and facilitate electron transfer to them. Applicants have tested various combinations of catalysts for use in a C02 sensor die which are described below with respect to **Figure 54** and **Tables XII** and **XIII**.

[00222] The nanoparticle CO2 sensor can be packaged together with an application specific integrated circuit (ASIC), which is designed to implement one or more calibration algorithms to calibrate the sensed CO2 concentrations detected by the sensor. According to an embodiment, the sensor and the ASIC can be packaged together as shown in **Figure 44**.

[00223] Therein, a C02 sensor package 4400 includes a housing having a top portion 4402 and a bottom portion 4404. In practice, the top and bottom portions of the housing can be integrally formed together or connected together, however they are shown as separated in the exploded view of **Figure 44** to enable viewing of the components within the bottom portion 4404 of the housing. The top portion 4402 of the housing includes a filter membrane 4406 which is disposed in an opening in the top portion 4402 of the housing and configured to permit C02 to enter the housing 4401. As discussed in more detail below, the filter membrane 4406 is configured to enable C02 molecules to enter the housing, but also to inhibit other, potentially interfering, types of molecules or particles from entering the housing. C02 sensor package 4400 also includes an ultraviolet (UV) light source 4405 for generating UV light which, as described above, is used to excite the C02 sensor, e.g., by reflecting the UV light from a bottom of the top portion 4402. The UV light source 4405 can, alternatively, be mounted on top of the sensor die 4407 in an orientation such that the UV light can either be reflected from the top of the bottom portion of the housing 4402 back onto the sensor die or, instead, can be flipped over such that the light generated by the UV light source 4405 directly impacts sensor die 4407. The C02 package 4400 also includes a nanoparticle-based C02 sensor die 4407 attached to an interior surface of the housing 4401 for generating sensed C02 concentration values based on the level of C02 which has entered the housing via filter membrane 4406. Additionally, the CO2 sensor package 4400 includes an ASIC 4409 which is attached to an interior surface of the housing 4401 and configured to calibrate the sensed C02 concentration values received from the sensor 4407. Each of these components will now be discussed in more detail below.

[00224] **Figure 45** depicts the relationship between the filter membrane 4406 and the C02 sensor die 4407 in the sensor package 4400. Encapsulation of the sensing element 4407 by a CO_2-selective filter membrane 4406 (connected to the top portion 4402 housing 4401 via gas tight sealing elements (not shown) in this embodiment) is intended to eliminate or reduce interference and/or degradation of harmful species in the environment which impacts the CO_2 sensing element, e.g., the region 4500 between the filter membrane 4406 and the C02 sensing element 4407 inside the housing. For example, water droplets, oil droplets, organic vapors, and water vapors can have detrimental impacts on the CO2 sensing sensitivity and stability. In the embodiment of **Figure 45**, the CO2 sensing element

4407 is protected by the filter membrane 4406 that allows CO_2 and air to permeate through while blocking all or most of the particulates (solid or liquid), larger molecules, and minimizing water vapor permeation. The filter membrane 4406 can have sufficiently high CO_2 permeance so that the addition of the filter membrane 4406 to the sensor package 4400 has little impact on the sensing dynamics, i.e., it does not block a sufficient amount of C02 from entering the detection zone 4500 to significantly skew the concentrations of C02 detected by sensor 4407 relative to the actual concentrations of C02 found outside the sensor package 4400.

[00225] According to an embodiment, the structures and techniques described in U.S. Patent Publication No. 2015/0265975A, entitled "THIN-SHEET ZEOLITE MEMBRANE AND METHODS FOR MAKING THE SAME" to Wei Lui et al., the disclosure of which is incorporated here by reference, can be used to fabricate a suitable membrane 4406 for sensor package 4400. Among other things, this patent publication describes how to make zeolite membrane sheets for separation of mixtures containing water. Thin, but robust, zeolite membrane sheets having an inter-grown zeolite crystal film directly on a thin, less than 200 microns thick, porous support sheet free of any surface pores with a size above 10 microns are described. The zeolite membrane film thickness is less than about 10 microns above the support surface and less than about 5 microns below the support surface. Methods of preparing the membrane are disclosed which include coating of the support sheet surface with a seed coating solution containing the parent zeolite crystals with mean particle sizes from about 0.5 to 2.0 microns at loading of 0.05-0.5 mg/cm2 and subsequent growth of the seeded sheet in a growth reactor loaded with a growth solution over a temperature range of about 45 degrees C to about 120 degrees C.

[00226] Alternatively, the filter membrane 4406 can be made from one or more of a plurality of materials including Polytetrafluoroethylene (PTFE), silicone, polyamide, ion-track etched membranes, and metal mesh. The membrane 4406 has a plurality of pores through which ambient air can enter the cavity. Also, the filter membrane can be treated to make them hydrophobic or oleophobic or both for various applications.

[00227] Turning now to the ASIC 4409, as mentioned above this component of the sensor package is used to, among other things, calibrate the C02 concentration values

which are generated by CO2 sensor 4407. ASIC 4409 can be designed to implement machine learning algorithms suitable for classifying and calibrating the sensor 4407 based on the measurement data received from the sensor 4407, some of which are described in more detail below. A block diagram of elements of an ASIC 4409 according to an exemplary embodiment is illustrated in **Figure 46,** as well as other elements within the sensor package 4400 which interact with the ASIC 4409.

[00228] For example, the C02 gas sensor block 4407 can provide inputs related to sensed levels of C02 to the ASIC 4409. These inputs can be conditioned by analog signal conditioning block 4602 to, for example, compensate the C02 level inputs for sensor bias. The conditioned inputs are then provided to a microcontroller core 4604 which processes the conditioned C02 inputs to generate accurate numerical data related to the sensed, ambient C02 levels outside of the sensor package 4400, which processing is discussed in more detail below. The microcontroller 4604 can also receive inputs from other sensors including, for example, temperature (T), relative humidity (RH) and pressure (P) sensors 4606. In some embodiments, microcontroller core 4604 can provide all of the processing and control functionality to generate C02 level output data. In other embodiments, some of the processing and/or control programming for the sensor package 4400 can be provided by an external controller 4608 which provides programming to the sensor package 4400 and receives addressing and data from the sensor package 4400, via a communication interface 4610. The ASIC 4409 also includes a peripheral driver block to, e.g., drive the UV LED which excites the C02 gas sensor block 4407. All of the elements shown in **Figure 46** are powered by a power management module 4614. Additionally, as will be described below, under certain circumstances it may be desirable to heat the sensors using one or more heating elements 4616 to improve the detection of C02 for certain sensor analytes, as discussed in more detail with respect to Table XII.

[00229] While the provision of the filter membrane 4406 and the target functionalized C02 sensor 4407 provide a first layer of protection against signals which interfere with the detection of C02 by sensor package 4400, e.g., interfering signals associated with the detection of condensation, other particles and large molecules, those interfering signals which remain can be compensated algorithmically by ASIC 4409. Gas sensing algorithms according to these embodiments are designed to both discern the desired signal (CO2)

from multiple correlated sources with more environmental signal sources (molecules) than sensing elements (inputs). Additionally, issues such as signal drift and dynamic behavior should be compensated for by the gas sensing algorithm implemented in ASIC 4409.

[00230] According to an embodiment such gas sensing algorithms are generated using a backpropagation artificial neural network (BPANN) with multilayer perceptron (MLP) coupled with a genetic algorithm to form a hybrid algorithm referred to here as the genetic algorithm neural network (GANN), which will be used for the identification and detection of CO_2. An exemplary GANN architecture and algorithm is illustrated in **Figures 47, 48 and 49**.

[00231] While the backpropagation artificial neural network can backpropagate the error and update the weights of the neural network, the BPANN algorithm is very slow in finding the optimal solution of the neural network. One way of addressing this challenge is to combine the genetic algorithm with the BPANN, which will accelerate the convergence rate of the search algorithm by using an optimization algorithm different from the gradient descent, therefore improving the training phase of the artificial neural network. In this specific case CO2 is the main analyte to detect. But other interferents such as CO and volatile organic compounds (VOCs) can be also present in the environment and need to be taken into consideration by the detection algorithm by minimizing the cross-sensitivity of the other gases which are present in the detection environment besides CO2. Consider the visualization of a neural network shown in **Figures 47 and 48,** as well as the more detailed functional description of the compensation algorithm according to an embodiment illustrated in the flow diagram of **Figure 49**.

[00232] Therein, the pattern recognition involves the gas mixture of three different analytes including CO2, CO and VOCs but, as will be appreciated by those skilled in the art, this pattern recognition can be extended to different mixtures of gases. The different stages of the GANN are respectively the training phase, the testing phase, and the recognition phase. The objective of the GANN algorithm is to minimize the sum squared error between the desired output and the computed output. The mathematical expression to be minimized is given in equation (13) as:

	$E = \sum_{r=1}^{q} \sum_{k=1}^{m} (y_k^r - O_k^r)^2$	(13)

where m is the number of output layer neurons, q is the number of learning samples; y_k^r is the desired output at node k and O_k^r is the actual output at node k. This error function is minimized by finding the optimal weights of the network. The population (the weights) of the genetic algorithm are represented by the chromosome while its infants are the genes.

[00233] Each gene can be coded using the 32-bit IEEE 754 floating point format. The different steps of the algorithm are the following:

The crossover and mutation operators are defined respectively by

$$p_c = \begin{cases} p_{c1} - \dfrac{(p_{c1} - p_{c2})(f' - \bar{f})}{(f_{opt} - \bar{f})} & f' \\ & > \bar{f} \\ p_{c1} & f' \leq \bar{f} \end{cases} \quad (14)$$

$$p_m = \begin{cases} p_{m1} - \dfrac{(p_{m1} - p_{m2})(f - \bar{f})}{(f_{opt} - \bar{f})} & f \\ & > \bar{f} \\ p_{m1} & f \leq \bar{f} \end{cases} \quad (15)$$

where f_{opt} is the optimal fitness function; f' is the best fitness function in every group; $\bar{f}$ and f are the average and single fitness function, respectively.

[00234] The genetic operation is based on the principle of a so-called “roulette wheel” type simulation where each individual chromosome is associated with a probability of being selected defined as $p_i = \frac{f_i}{\sum_{j=1}^{N} f_j}$ where N is the number of individuals in the population. Hence, the crossover and mutation operators are computed as equations (2) and (3). The

best parameters are retained and are used to update the weights and thresholds of the neural network.

[00235] The steps of the algorithm according to an embodiment are described below and also illustrated in the flow diagram 4900 of **Figure 49.** Therein, at step 4902, the initial Artificial Neural Network Architecture (ANN) structure is defined based on the by the input and output parameters and the number of neurons in the hidden layer. At step, 4904, the neural network parameters are randomly initialized (i.e., weights and bias values are updated randomly). At step 4906, the mean square error is calculated, where the error is the target output minus the actual output. If the error is greater than the predefined minimum error, then the genetic algorithm loop is followed in steps 4910 and 4912 until the minimum error is found. The genetic algorithm applied in step 4910 is used to optimize the weights and threshold of the network. The fitness value is calculated using the fitness function. The best fitness value corresponds to the individual with the help of mutation, crossover and selection. Training ends in step 4914 when the error is less than the minimum error threshold.

[00236] An advantage of using GANN as part of the algorithm implemented by ASIC 4409 to detect CO2 based on the output of sensor 4407 according to this embodiment lies in its ability to deal with non-linear hypotheses, especially during transient conditions where non-linearities play an important role. Another advantage of the GANN algorithm is its ability to (i) discriminate the target gas CO_2, from other interfering gases (e.g., VOCs, CO.) that might be present, hence minimizing the cross-sensitivity of the CO_2 sensor and (ii) avoid the problem of overfitting which can degrade the performance of the GANN algorithm when predicting unknown CO_2 concentrations. Another advantage of the GANN algorithm is its ability to find optimal solutions of the cost function much faster than the BPANN and GA, as shown in **Figure 50**. According to some embodiments, drift compensation of the output sensor 4407 data can be implemented using the orthogonal signal (OSC) method. In the OSC method, drift is defined as an aperiodic temporal variation of the sensor output signal when it is exposed to the same analyte under identical conditions. The causes associated with the drift concept are inherent to the sensor material used to functionalize sensor 4407 which degrades over time due to aging. A typical variation of the signal drift is shown in **Figure 51**, albeit for N02 as an analyte rather than C02. Therein, the spectral

analysis of the time-domain signal reveals high and low frequency components of the signal. The high frequency components are associated with noise whereas the low frequency are the drift components. The time-domain signal sensor output signal x(t) can be expressed as:

$$x(t) = x_r(t) + x_n(t) + x_d(t) \quad (16)$$

where $x_r(t)$ is the real component of the signal, $x_n(t)$ is the high frequency component of the signal and $x_d(t)$ is the low frequency drift component of the signal.

[00237] Different techniques associated with drift correction algorithms are listed in **Figure 52**. There are four major areas: sensor signal preprocessing, periodic calibrations, attuning methods, and adaptive methods. Preprocessing techniques such as baseline correction help to filter the noisy part of the signal in addition in taking care of the drift. The automatic baseline correction algorithm falls under this category and is widely used in industry for drift correction. Typical application of automatic baseline correction is in non-dispersive infrared (NDIR) sensors to improve signal stability due to drift. It has been shown that when baseline correction is coupled with orthogonal signal methods (OSC), the stability of the output signal is improved. The idea behind the algorithm is to remove the components from the gas array responses that account for the major variation of the signal but which are not important factors for the computation of the analyte concentrations, in this embodiment CO2.

[00238] Turning now to the details of the CO2 sensor 4407 in sensor package 4400 according to an embodiment, the sensor can be manufactured as described above with a functionalization layer that is selected for C02 adsorption, e.g., using SnO_2 and SnO_2-CuO nanoparticles as shown in **Figure 53**. A resulting sensor performance is shown in **Figure 54**. However, those skilled in the art will appreciate that these embodiments are not limited to using those specific types of nanoparticles in the CO2 sensor and that other types of nanoparticles can be selected and used. Indeed Applicants have tested a number of oxide and metal/metal oxide particle combinations for suitability with respect to their ability to detect CO2 when manufactured in accordance with the foregoing embodiments examples are provided below with respect to Tables XII and XIII.

Oxides	RTA	Metals	0.5% CO2/20% O2/N2		0.5% CO2/30% O2/N2	
			20% O2/N2		30% O2/N2	
			dry	50% RH	dry	50% RH
3%Mg-1%Al-ZnO	400 C, 300s, 2K Ar	Bare	R=0 for 20% 02 R<1% for 10% 02	R=0	R=0	R<1%
		Pd-Ag	R=0 for 20% 02 R<1% for 10% 02	R=0	R=0	R<1%
		Pd	R=0 for 20% 02 R<1% for 10% 02	R=0	R=0	R<1%
		Cu	R=0 for 20% O2 R<1% for 10% 02	R=0	R=0	R<1%
	400 C, 300s, 1.8K Ar + 200 O2	Pt	R=0 for 20% 02 R<1% for 10% 02	R=0	R<1%	R<1%
In2O3	400 C, 300s, 1.8K Ar + 200 O2	Pd-Ag	R<1%	R<1%	--	R=0 at RT +@70C
		Pd	R<1%	R<1%	R=0	R=0 at RT +@70C
		Ag	R<1%	R<1%	R=0	R=0 at RT R<1%@70C
		Au	R<1%	R<1%	R<1%	R<1%
		Pt	R<1%	R<1%	--	R=0 at RT R<1%@70C
		Ni	R<1%	R<1%	R<1%	R<1%
		Cu	R<1%	R<1%	R<1%	R<1%
10% Pd-SnO2	700 C, 60s, 2K Ar	Bare	R=0	R=0	R<1%	R<1%
		Pd-Ag	R=0	R<1%	R<1%	R<1%
		Pd	R=0	R<1%	R<1%	R<1%
		Cu	R=0	R=0	R<1%	R<1%
3%Ca-1%Al-ZnO	400 C, 300s, 2K Ar	Bare	R<1%	R<1%	--	R<1%
		Pd-Ag	R<1%	R<1%	-- 1%<R<5%	R<1%
		Pd	R<1%	R<1%	-- 1%<R<5%	R=0
		Cu	R<1%	R<1%	+ 5%<R<10%	R<1%

Table XII

Oxides	RTA	Metals	0.5% CO2/Air		0.5% CO2 (pure)		
			Air		N2		
			dry	50% RH	dry	50% RH	85% RH
3%Mg-1%Al-ZnO	400 C, 300s, 2K Ar	Bare	R<1%	R<1%	-- 1%<R<5%	-- 5%<R<10%	R<1%
		Pd-Ag	R<1%	R<1%	-- 5%<R<10%	-- R>10%	R<1%
		Pd	R<1%	R<1%	-- 5%<R<10%	-- 5%<R<10%	R<1%
		Cu	R<1%	R<1%	R=0	Y	R<1%
	400 C, 300s, 1.8K Ar + 200 O2	Pt	R<1%	R<1%	R<1%	R<1%	R<1%
In2O3	400 C, 300s, 1.8K Ar + 200 O2	Pd-Ag	-- R>10%	-- R>10%	R<1%	R<1%	R<1%
		Pd	-- @RT +@80C R>10%	-- R>10%	R<1%	--	R<1%
		Ag	-- @RT +@80C	--	R=0	R=0	R<1%
		Au	+@75C	+@75C	R<1%	R<1%	R<1%
		Pt	-- R>10%	-- R>10%	--	-- 1%<R<5%	R<1%
		Ni	+	+@75C	R<1%	R<1%	R<1%
		Cu	+	+	R<1%	R<1%	R<1%
10% Pd-SnO2	700 C, 60s, 2K Ar	Bare	R<1%	R<1%	R=0	-- 5%<R<10%	-- 1%<R<5%
		Pd-Ag	R<1%	R<1%	R<1%	-- 1%<R<5%	--
		Pd	R<1%	R<1%	R<1%	-- 1%<R<5%	--
		Cu	R<1%	R<1%	R<1%	R<1%	R<1%
3%Ca-1%Al-ZnO	400 C, 300s, 2K Ar	Bare	R<1%	R<1%	R=0	R=0	R<1%
		Pd-Ag	R<1%	R<1%	R=0	R=0	R<1%
		Pd	R<1%	R<1%	R=0	R=0	R<1%
		Cu	R<1%	R<1%	R=0	R=0	R<1%

Table XIII

Legend for Tables XII and XIII

--- = response is a decrease in current relative to baseline

+ = response is an increase in current relative to baseline

Bare = no metal deposited with oxide

C= Celsius

R= Response

RH = Relative Humidity

RT = Room Temperature

[00239] Tables XII and XIII provide information about various oxide/metal combinations which Applicants tested for use as the C02 adsorbing particles deposited on a target substrate of the sensor 4407 according to various embodiments. Starting from the lefthand side of Table XII, the first column (Oxides) indicates the various (primary) oxides which were deposited on a target substrate of the sensor 4407, i.e., zinc oxide (ZnO), indium oxide (IN203), and tin oxide (SnO2). Note that although reference here is made to Table XII, similar comments apply to Table XIII which is essentially an extension of Table XII. In some cases, the oxides were doped with different elements, primarily metals. For example, in the first row of Table XII the ZnO was doped with 3% magnesium (Mn) and 1% aluminum (Al), percentages by atomic weight.

[00240] The second column of Table XII (Rapid Thermal Annealing (RTA)) indicates certain parameters which are used to anneal the target substrate after the oxide particles have been deposited thereon. For example, for the first four metals (column 3), the doped ZnO in the first row is annealed at 400 degrees C for 300 seconds while being subjected to a flow of argon gas at a flow rate of 2000 standard cubic centimeter/minute. By reviewing the second column of Tables XII and XIII, it will be appreciated that Applicants have also discovered that different annealing conditions have been determined to be optimal to create sensors for detecting carbon dioxide for different oxides used in sensors according to these embodiments. After annealing, different target substrates with the ZnO particles also have various metals (or metal oxides) deposited thereon (Metal column). The first entry in this row, “Bare”, indicates that this particular target substrate did not have any metal deposited thereon. However four other ZnO target substrates each were tested with different metal particles deposited thereon, i.e., Palladium (Pd) and Silver (Ag) particles, Palladium

particles, Copper (Cu) particles and Platinum (Pt) particles. Thus, each row in the Tables is associated with a target substrate used in a sensor 4407 having primary oxide particles deposited on the target substrate, followed by an annealing process, followed by deposition of secondary metal (or metal oxide particles) which are then tested as described below.

[00241] At the top of the fourth and fifth columns (i.e., "dry" and "50% RH), a first analyte (gas mixture) is identified, i.e., 0.5% CO2/20% O2/N2. This means that the target substrates having the oxide/metal combinations indicated in the first and third columns of Table XII were each exposed to a gas mixture having 0.5% carbon dioxide and 20% each of oxygen and nitrogen in order to determine how well the target substrate in the sensor was able to respond to the presence of the carbon dioxide. The fourth column indicates results for the different target substrates exposed to this analyte under dry condition, while the fifth column indicates results for the different target substrates exposed to this analyte under damper conditions, i.e., 50% relative humidity.

[00242] Each of the blocks in Table XII under the fourth column thus indicate certain results or characterizations of a target substrate having a particular combination of oxide particles and metal particles (except for the "bare" blocks) associated with the sensor's response (R) to the presence of carbon dioxide in the 20% O2/N2 gas mixture under dry conditions. In this context, a response R of a target substrate refers to a change in current (signal) passing through the sensor due to the presence of carbon dioxide relative to a baseline current (i.e., the current passing through the sensor when it is exposed to air without any carbon dioxide). For example, in the first block in the "dry" row, the target substrate having 3%Mg-1%AlZnO oxide particles with no metal particles, exhibited a response R to the carbon dioxide that was 0 (i.e., no response) for a gas mixture containing 20% oxygen, however when the amount of oxygen in the mixture was reduced to 10%, the sensor did generate a minor response (R<1%) to the presence of the 0.5% carbon dioxide in the gas mixture to which that particular target substrate was exposed.

[00243] Similar indications of responses (R values) are provided throughout Tables XII and XIII for target substrates having different combinations of oxide particles, annealing parameters, and metal particles, as well as different analytes and humidity condition. Reading across the top row of Tables XII and XIII, one can see that the various target substrates were tested against four different analytes: (1) 0.5% Co2/20% O2/N2, (2) 0.5% CO2/30% O2/N2, (3) 0.5% CO2/Air and 0.5% CO2 (pure). For brevity, not every block in

these tables will be discussed here with a few noteworthy exceptions. First of all, it will be appreciated by those skilled in the art, reviewing Tables XII and XIII, that Applicants found that the best carbon dioxide sensors in terms of sensor response to the presence of carbon dioxide are those which exhibited a response R of more than 10% to the presence of CO2, i.e., blocks in the tables having R>10%. Two such blocks can be seen in Table XIII for the In2O3 oxide/Pd metal particle target substrate when exposed to an analyte mixture of 0.5% CO2 in a "normal" air mixture under either dry or moist (50% RH) conditions.

[00244] Two other parameters indicated in Tables XII and XIII warrant a brief discussion. First, Applicants have found that for some oxide/metal particle combinations, the sensor performs differently (in some cases better) in terms of its ability to sense/detect CO2 when the sensing element(s) is heated which is the reason why, in some embodiments, a heating element is provided for the sensor block. For example, in Table XII, for the sensor using a target substrate with the combination of In2O3 oxide particles and Ag metal particles, it was found that the sensor had no response to carbon dioxide at room temperature (RT), but when the sensor was heated to 70 degrees C, the same sensor combination exhibited a minor response (R<1%) to carbon dioxide.

[00245] Secondly, Applicants have noted that the response (change in sensor current) to various gases for various oxide particle/metal particle combinations and test parameters can also vary in its direction relative to the baseline current, i.e., some sensors exhibit a positive (+) change relative to baseline in the presence of the target analyte (in these embodiments CO2), whereas some sensors exhibit a negative change (--) relative to baseline in the presence of the target analyte. Some examples of this are seen in Tables XII and XIII where blocks contain either the + or --- symbols. For example, looking at Table XIII, for the results block associated with the combination of In203 oxide particles and Pd metal particles, exposed to an analyte gas mixture of 0.5% carbon dioxide and air under dry conditions, Applicants discovered that this sensor exhibited a negative current response at room temperature (--@RT) of greater than 10% but a positive current response when the sensor was heated to 80C (+@80C) of greater than 10%.). This positive/negative response quality may prove useful in embodiments where an array of sensors is used to generate a signature associated with the gases sensed by the sensor array. In this context if there are a plurality of sensing elements (which are unique) and a complex gas mixture that they are exposed to, then by comparing the signs of the sensor responses

along with magnitude of the responses of different sensing elements, embodiments can obtain a better pattern recognition capability, than if the outputs of the sensors were just signal magnitude.

[00246] Although not provided as an example in Tables XII or XIII, Applicants additionally note that WO3 can be used as a primary metal oxide for a CO2 sensor in accordance with these embodiments.

[00247] Thus, according to another embodiment, a method 5500 for sensing carbon dioxide gas concentration is illustrated in Figure 55. Therein, at step 5502, an ambient gas mixture is filtered through a filter membrane into a cavity. At step 5504, light is generated (and transmitted) onto a sensor disposed in the cavity. At step 5506, carbon dioxide in the ambient gas mixture is sensed using the sensor, wherein the sensor is configured with first particles functionalizing an outer surface thereof to adsorb a target analyte in a presence of light, wherein the target analyte is carbon dioxide, and further configured to output data associated with a concentration of carbon dioxide sensed by the sensor.

[00248] All publications and patents mentioned in this specification are herein incorporated by reference to the same extent as if each individual publication or patent application was specifically and individually indicated to be incorporated by reference in its entirety. While the invention has been described in connection with specific embodiments thereof, it will be understood that it is capable of further modifications and this application is intended to cover any variations, uses, or adaptations of the invention following, in general, the principles of the invention and including such departures from the present disclosure as come within known or customary practice within the art to which the invention pertains and as may be applied to the essential features hereinbefore set forth.

[00249] Although the features and elements of the present embodiments are described in the embodiments in particular combinations, each feature or element can be used alone without the other features and elements of the embodiments or in various combinations with or without other features and elements disclosed herein. The methods or flow charts provided in the present application may be implemented in a computer program, software, or firmware tangibly embodied in a computer-readable storage medium for execution by a general purpose computer or a processor.

[00250] This written description uses examples of the subject matter disclosed to enable any person skilled in the art to practice the same, including making and using any devices or systems and performing any incorporated methods. The patentable scope of the subject matter is defined by the claims, and may include other examples that occur to those skilled in the art. Such other examples are intended to be within the scope of the claims.

WHAT IS CLAIMED IS:

1. A sensor package (4400) comprising:

a housing (4402, 4404) including an opening;

a filter membrane (4406) mounted in the opening of the housing (4402, 4404);

a sensor (4407) disposed within a cavity (4500) in the housing (4402, 4404), the cavity (4500) being disposed beneath the opening, wherein the sensor (4407) is configured with first particles functionalizing an outer surface thereof to adsorb a target analyte in a presence of ultraviolet (UV) light, wherein the target analyte is carbon dioxide, and further configured to output data associated with a concentration of carbon dioxide sensed by said sensor (4407);

an application specific integrated circuit (ASIC, 4409) disposed within the housing (4402, 4404) and configured to process data from the sensor (4407) and output processed data associated with the concentration of carbon dioxide; and

a UV light source (4405) disposed within the housing (4402, 4404) and configured to generate the UV light.

2. The sensor package of claim 1, further comprising a substrate suitable for interconnecting integrated circuits disposed within the housing and upon which the sensor, ASIC and UV light source are mounted.

3. The sensor package of claims 1 or 2, wherein the sensor further comprises second particles functionalizing said outer surface of said sensor, wherein an interfering analyte adsorbs on said second particles.

4. The sensor package of claim 3, wherein said interfering analyte is carbon monoxide.

5. The sensor package of any of claims 1-4, wherein the filter membrane is a membrane made from one or more of a plurality of materials including Polytetrafluoroethylene (PTFE), silicone, polyamide, ion-track etched membranes, metal mesh, and wherein the membrane has a plurality of pores through which ambient air can enter the cavity.

6. The sensor package of any of claims 1-5, wherein the filter membrane is configured to permit C02 to substantially pass through the filter membrane into the cavity and to inhibit passage of at least one of: water droplets, water vapor, and organic vapors.

7. The sensor package of any of claims 1-6, further comprising:
one or more heating elements for heating the sensor.

8. The sensor package of claim 7, wherein the one or more heating elements heat the sensor to a temperature within a range of 60 degrees C to 100 degrees C.

9. The sensor package of any of claims 1-8, wherein the ASIC processes the data to remove effects associated with interfering signals and/or sensor drift.

10. The sensor package of any of claims 1-9, wherein the first particles include one of: Zn0, In203, WO3 or SN02 particles.

11. The sensor package of claim 10, wherein the first particles also include one of: Pd-Ag, Pd, Cu, Pt, Ag, Au or Ni particles.

12. A method (5500) for sensing carbon dioxide gas concentration, the method comprising:
filtering (5502) an ambient gas mixture through a filter membrane into a cavity;
generating (5504) light onto a sensor disposed in said cavity; and
sensing (5506) carbon dioxide in the ambient gas mixture using the sensor, wherein the sensor is configured with first particles functionalizing an outer surface thereof to adsorb a target analyte in a presence of light, wherein the target analyte is carbon dioxide, and further configured to output data associated with a concentration of carbon dioxide sensed by said sensor.

13. The method of claim 12, further comprising providing, with said sensor, an application specific integrated circuit (ASIC) disposed within a housing and configured to

process data from the sensor and output processed data associated with the concentration of carbon dioxide.

14. The method of claims 12 or 13, wherein the sensor further comprises second particles functionalizing said outer surface of said sensor, wherein an interfering analyte adsorbs on said second particles.

15. The method of claim 14, wherein said interfering analyte is carbon monoxide.

16. The method of any of claims 12-15, wherein the filter membrane is a membrane made from one or more of a plurality of materials including Polytetrafluoroethylene (PTFE), silicone, polyamide, ion-track etched membranes, metal mesh, and wherein the membrane has a plurality of pores through which ambient air can enter the cavity.

17. The method of any of claims 12-16, wherein the filter membrane is configured to permit C02 to substantially pass through the filter membrane into the cavity and to inhibit passage of at least one of: water droplets, water vapor, and organic vapors.

18. The method of any of claims 12-17, further comprising: heating the sensor.

19. The method of claim 17, wherein the one or more heating elements heat the sensor to a temperature within a range of 60 degrees C to 100 degrees C.

20. The method of any of claims 13-19, wherein the ASIC processes the data to remove effects associated with interfering signals and/or sensor drift.

21. The method of any of claims 12-20, wherein the first particles include one of: Zn0, In203, WO3 or SN02 particles.

22. The method of claim 21, wherein the first particles also include one of: Pd-Ag, Pd, Cu, Pt, Ag, Au or Ni particles.

23. A carbon dioxide sensor (4400) comprising:

a substrate (4407) on which oxide particles are deposited, wherein said oxide particles include one of: ZnO, In203, WO3 or Sn02 particles, and wherein said carbon dioxide sensor (4400) exhibits a response to a presence of carbon dioxide proximate the substrate.

24. The carbon dioxide sensor of claim 23 wherein the substrate also has metal particles deposited thereon, said metal particles including one of Pd-Ag, Pd, Cu, Pt, Ag, Au or Ni particles.

25. The carbon dioxide sensor of claim 23 or 24, further comprising:

an application specific integrated circuit (ASIC) disposed within the housing and configured to process data from the sensor and output processed data associated with the concentration of carbon dioxide.

26. The carbon dioxide sensor of any of claims 23-25, further comprising:

an ultraviolet (UV) light source configured to generate and direct UV light onto said substrate.

FIGURE 1A

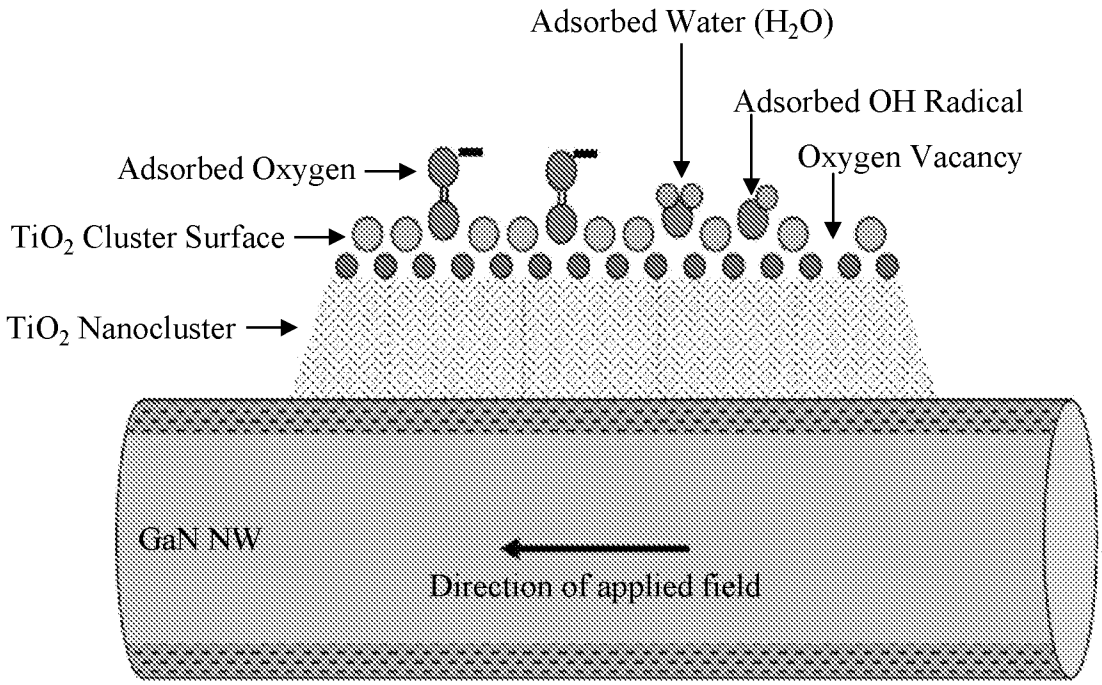
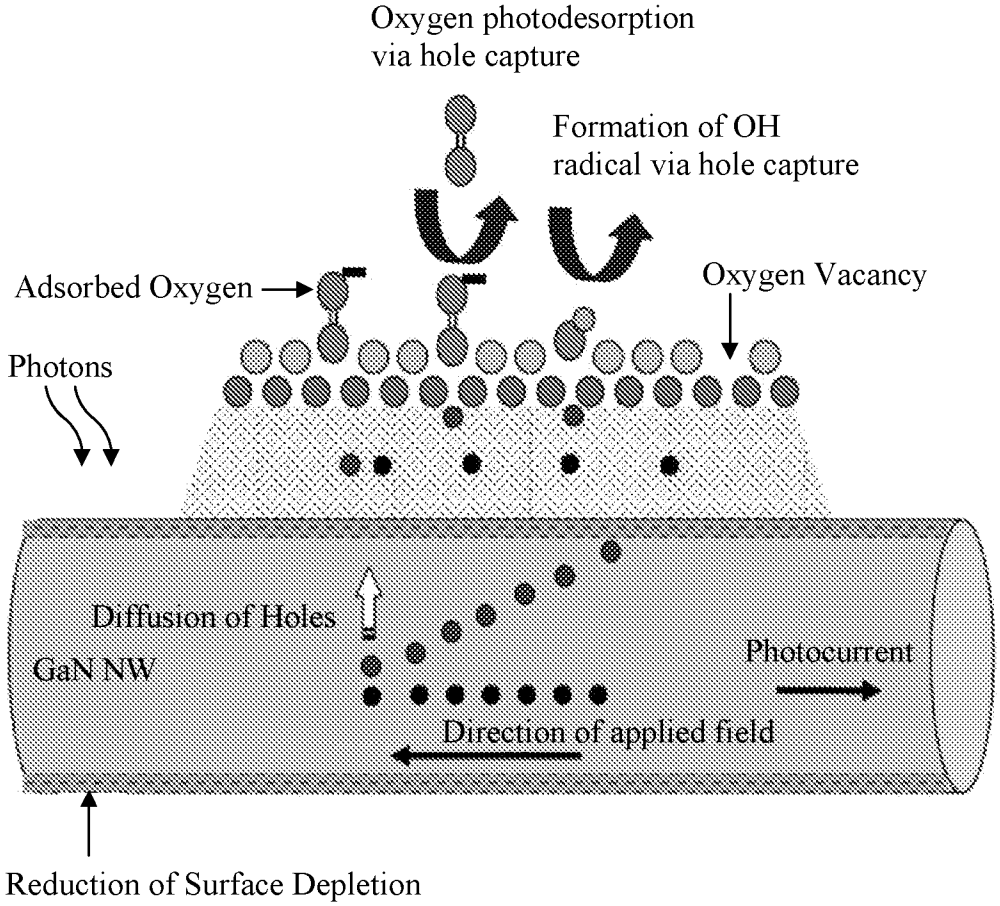


FIGURE 1B



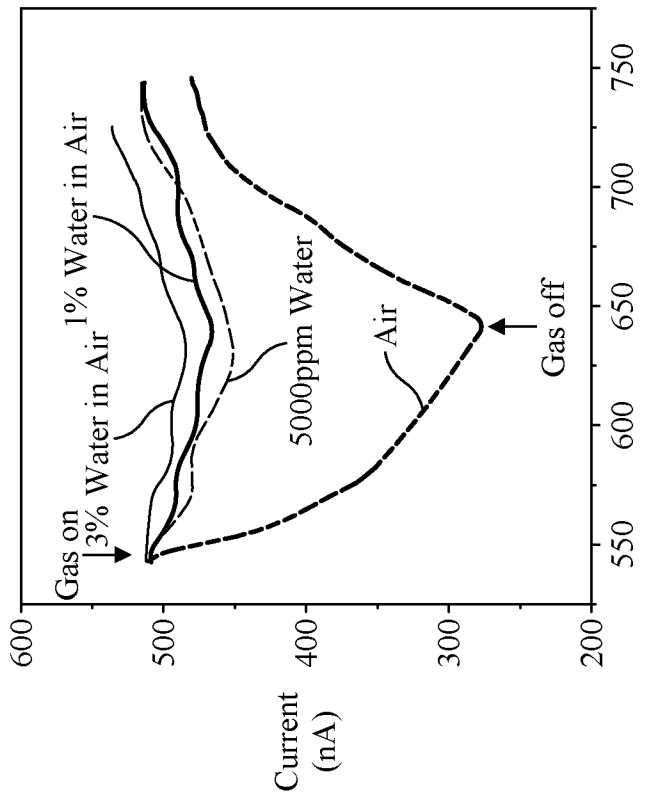


FIGURE 2B

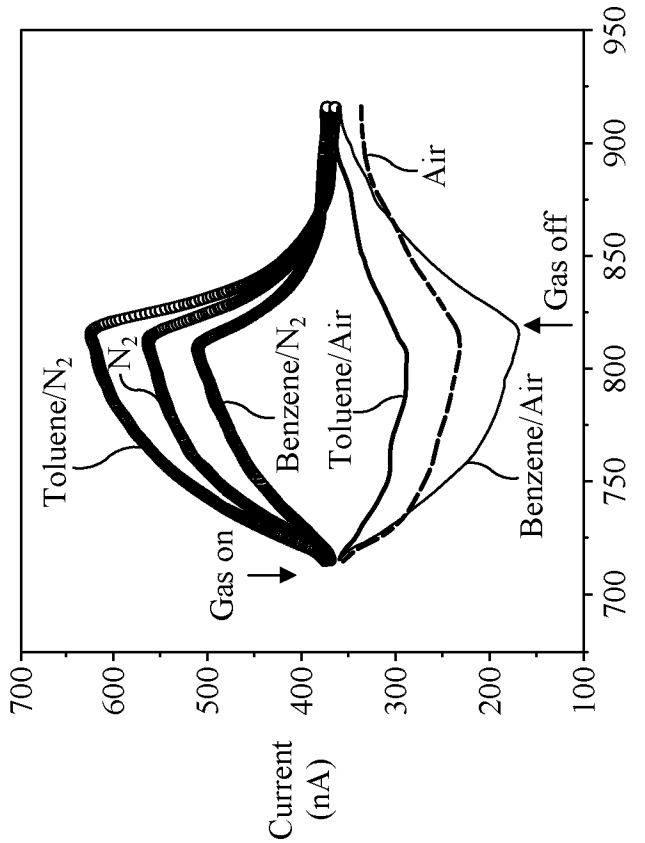
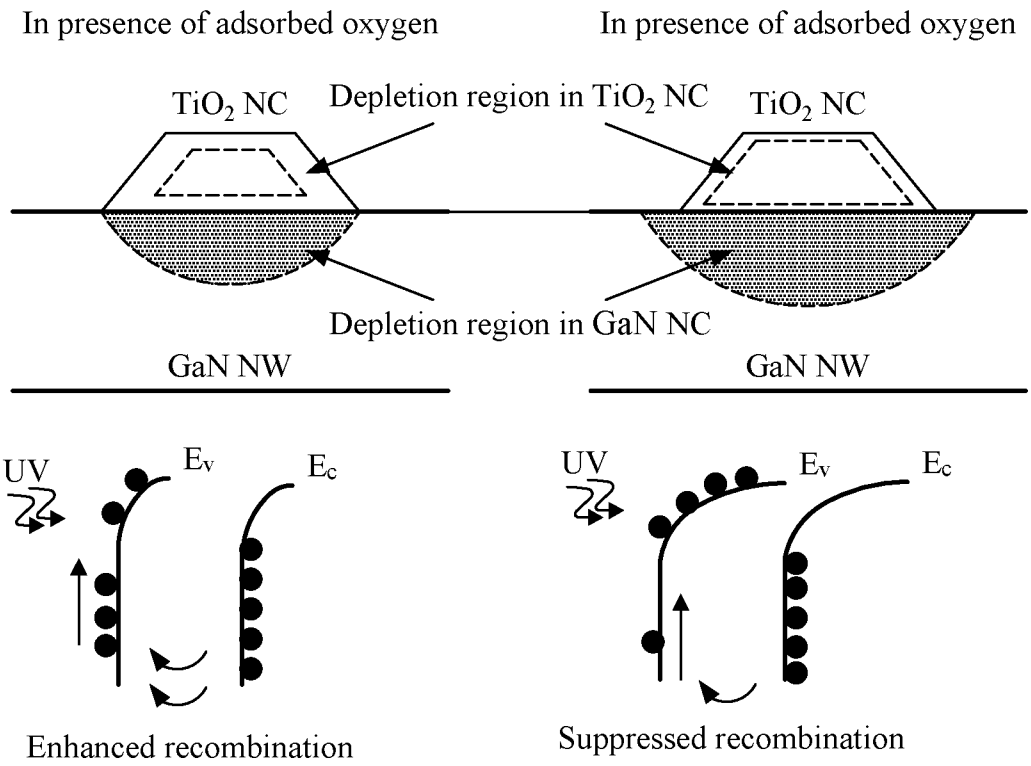


FIGURE 2A

FIGURE 3



Surface band-bending in GaN NW under the TiO_2 NC

E_c is conduction band-edge with photogenerated electrons
E_v is valance band-edge with photogenerated holes
O are photogenerated charge carriers

FIGURE 4

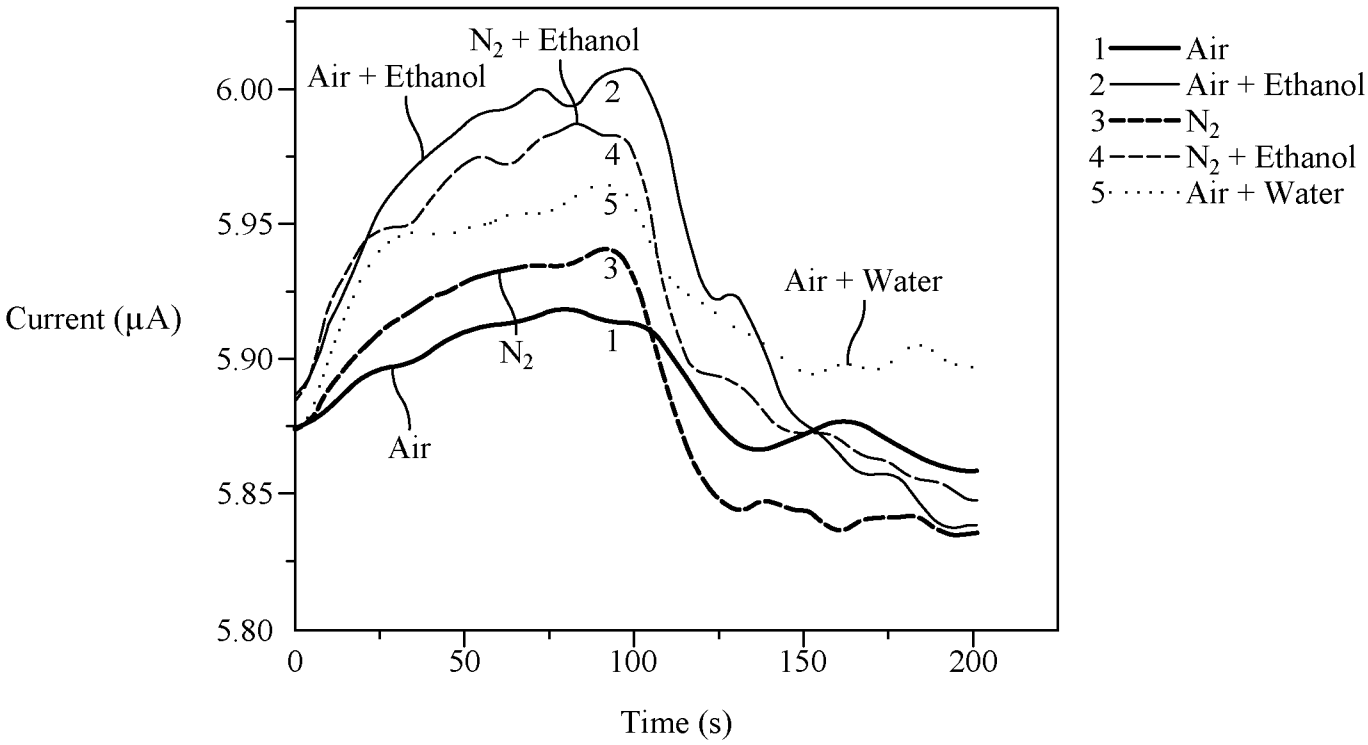

Current (μA)
6.00
5.95
5.90
5.85
5.80
0
50
100
150
200
Time (s)
N2 + Ethanol
Air + Ethanol
Air + Water
N2
Air
1
2
3
4
5
1 Air
2 Air + Ethanol
3 N2
4 N2 + Ethanol
5 Air + Water

FIGURE 5A

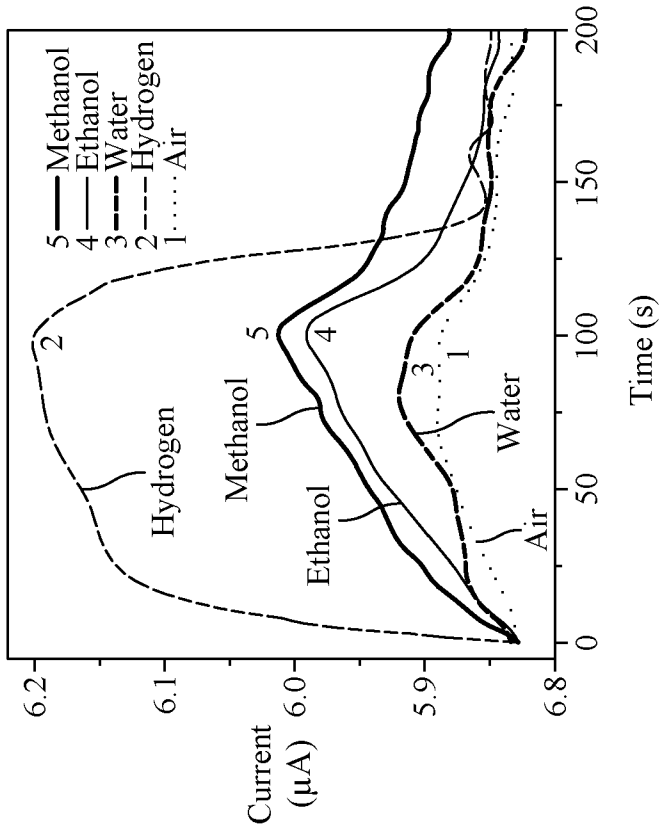


FIGURE 5B

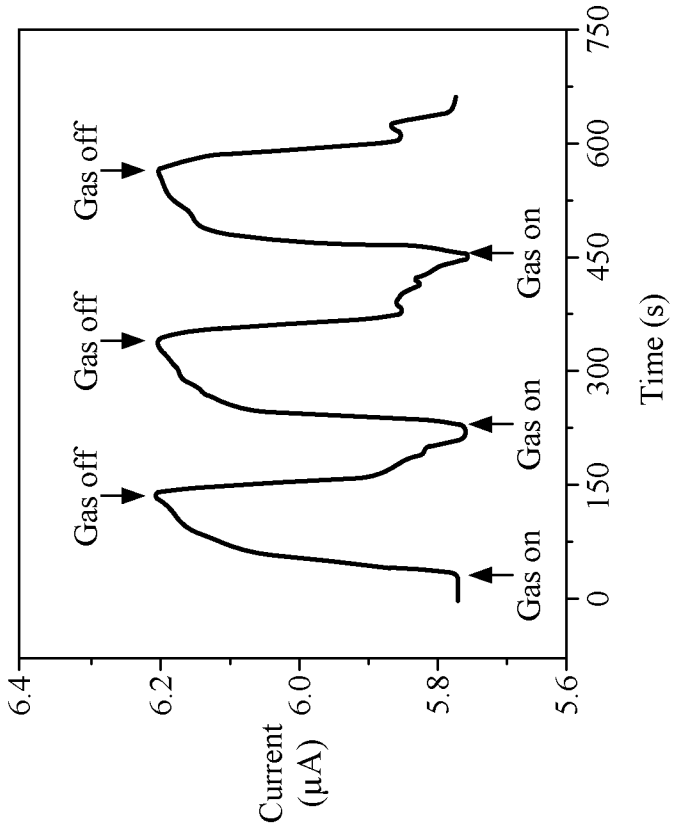


FIGURE 6A

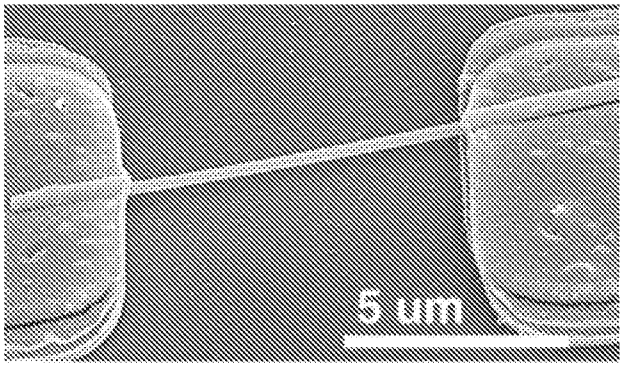


FIGURE 6B

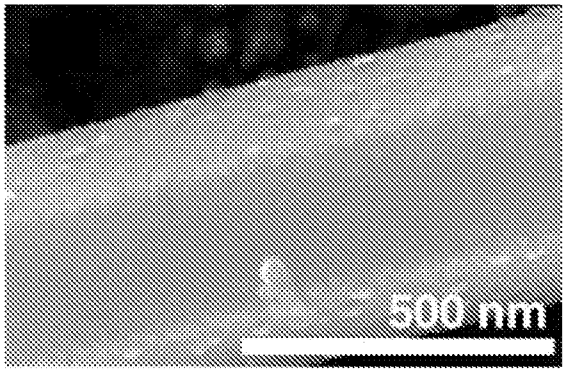


FIGURE 6C

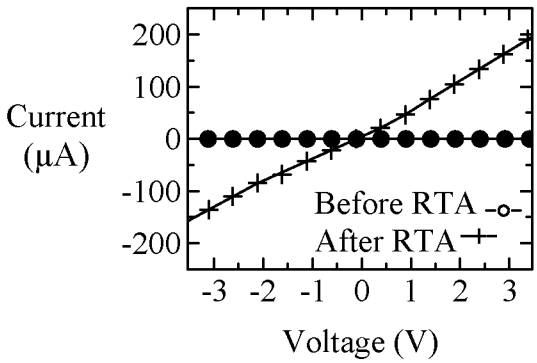


FIGURE 6D

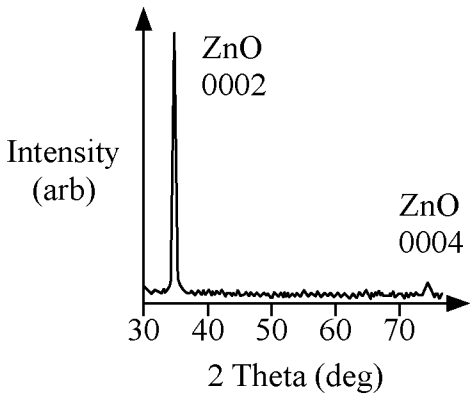
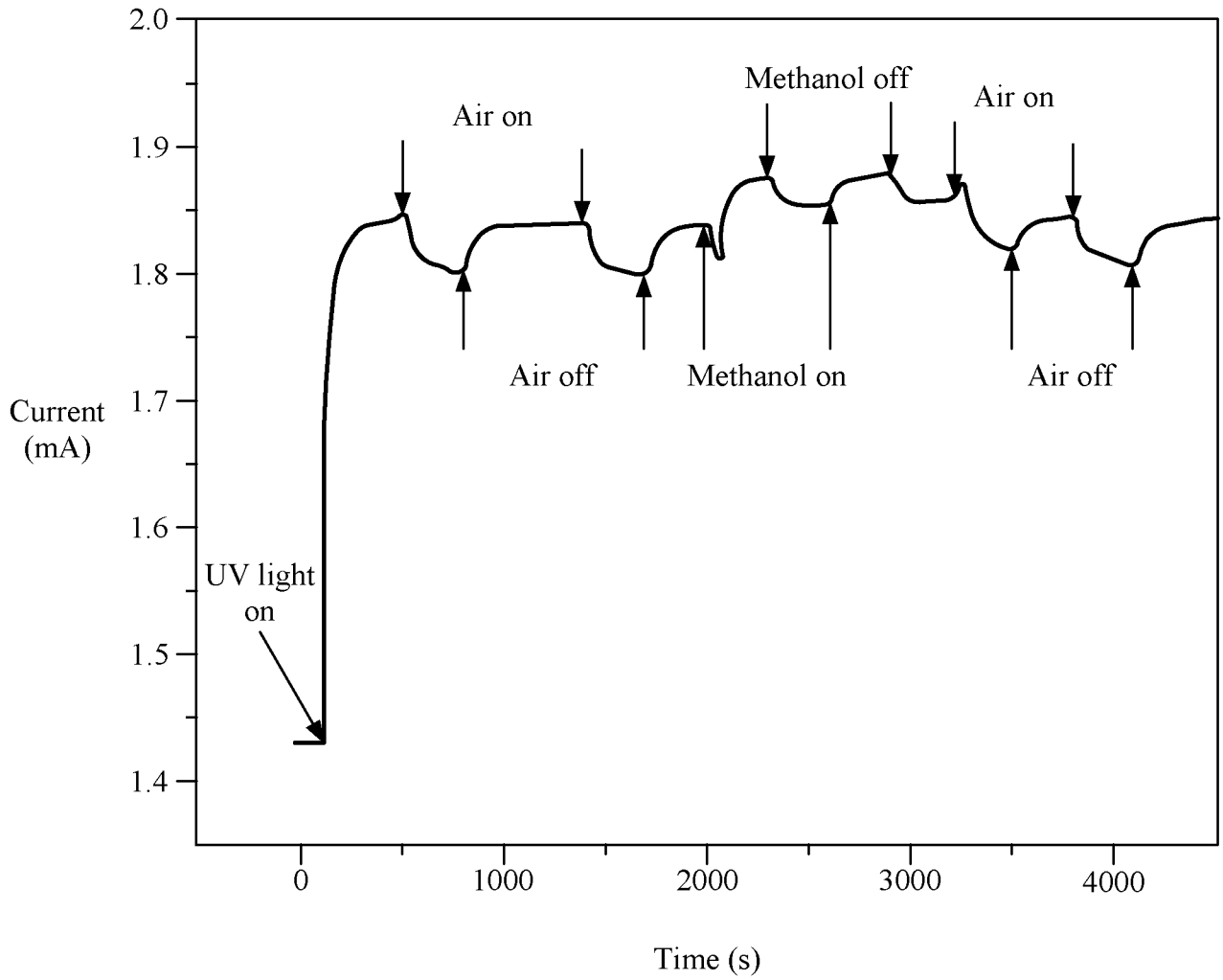
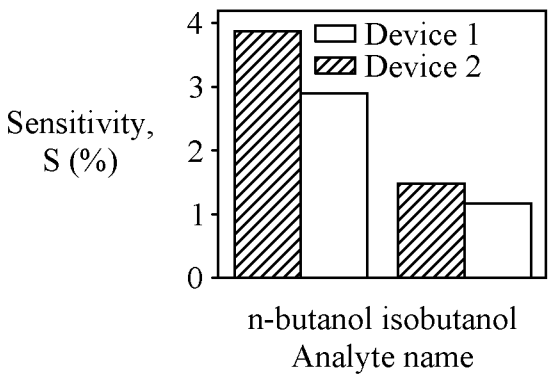


FIGURE 7


2.0
1.9
1.8
1.7
1.6
1.5
1.4
Current (mA)
UV light on
Air on
Air off
Methanol off
Methanol on
Air on
Air off
0
1000
2000
3000
4000
Time (s)


Sensitivity, S (%)
Device 1
Device 2
0
1
2
3
4
n-butanol
isobutanol
Analyte name

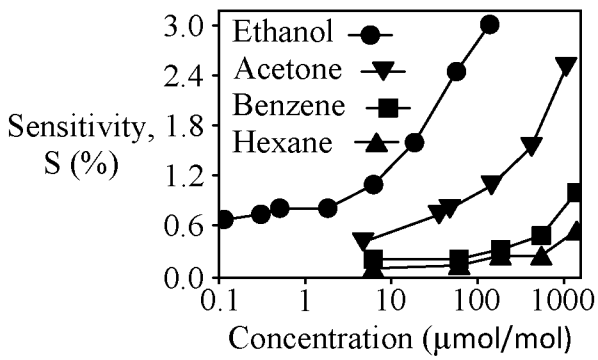

Sensitivity, S (%)
Ethanol
Acetone
Benzene
Hexane
0.0
0.6
1.2
1.8
2.4
3.0
0.1
1
10
100
1000
Concentration (µmol/mol)

FIGURE 8A

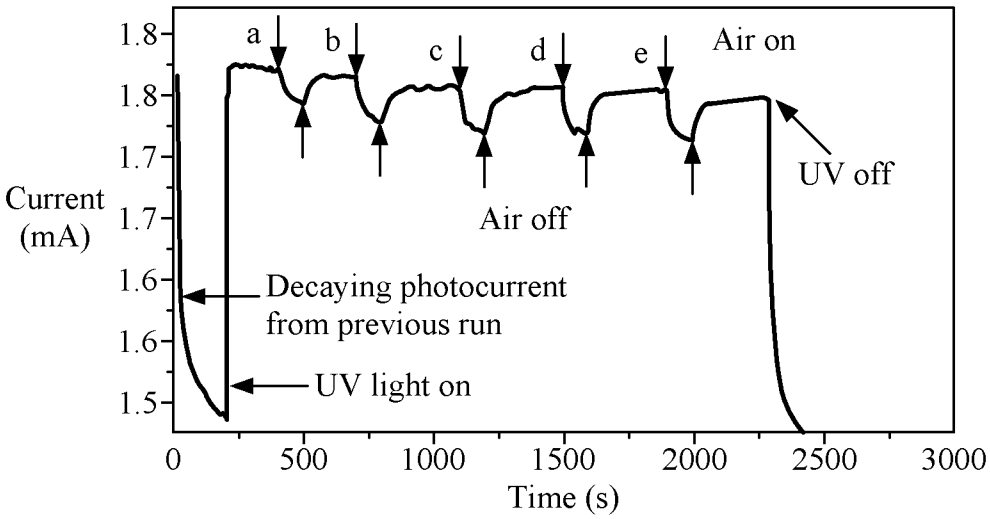


FIGURE 8B

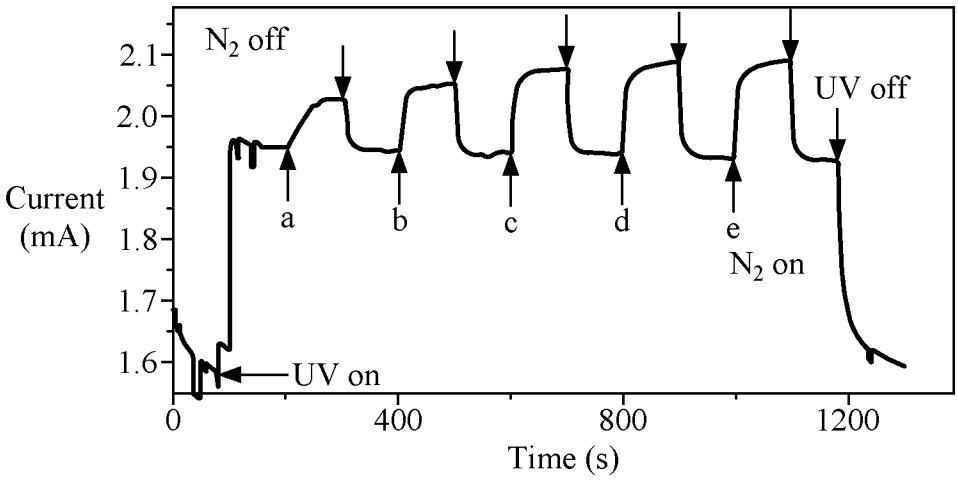


FIGURE 9A

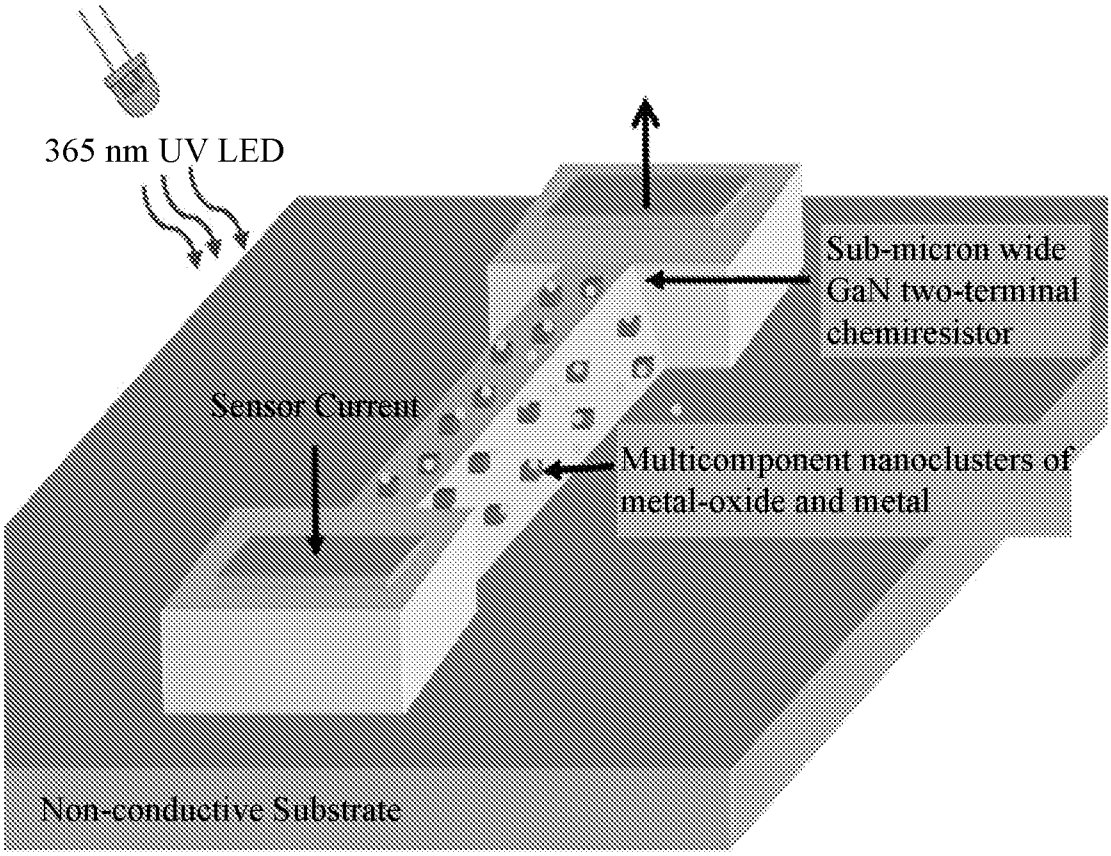


FIGURE 9B

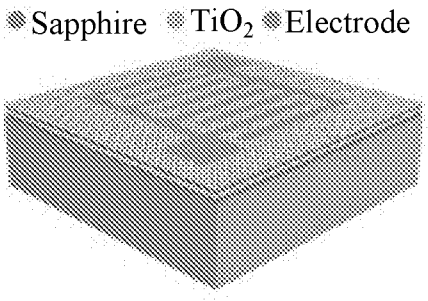


FIGURE 9C

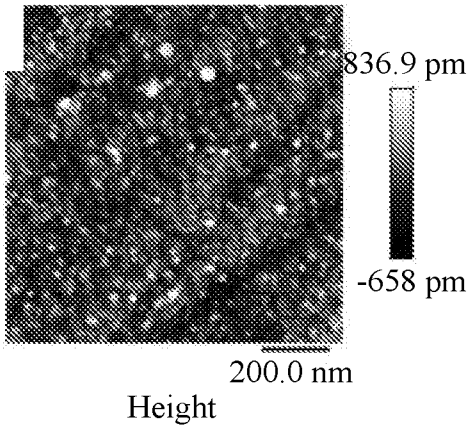


FIGURE 9D

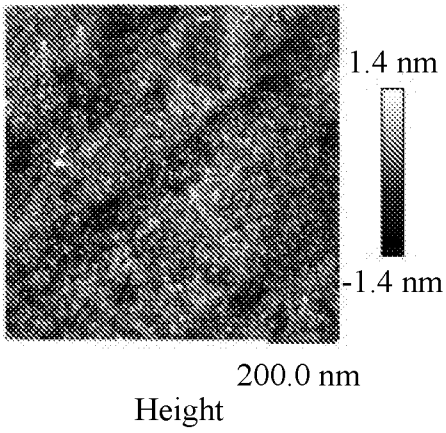


FIGURE 10

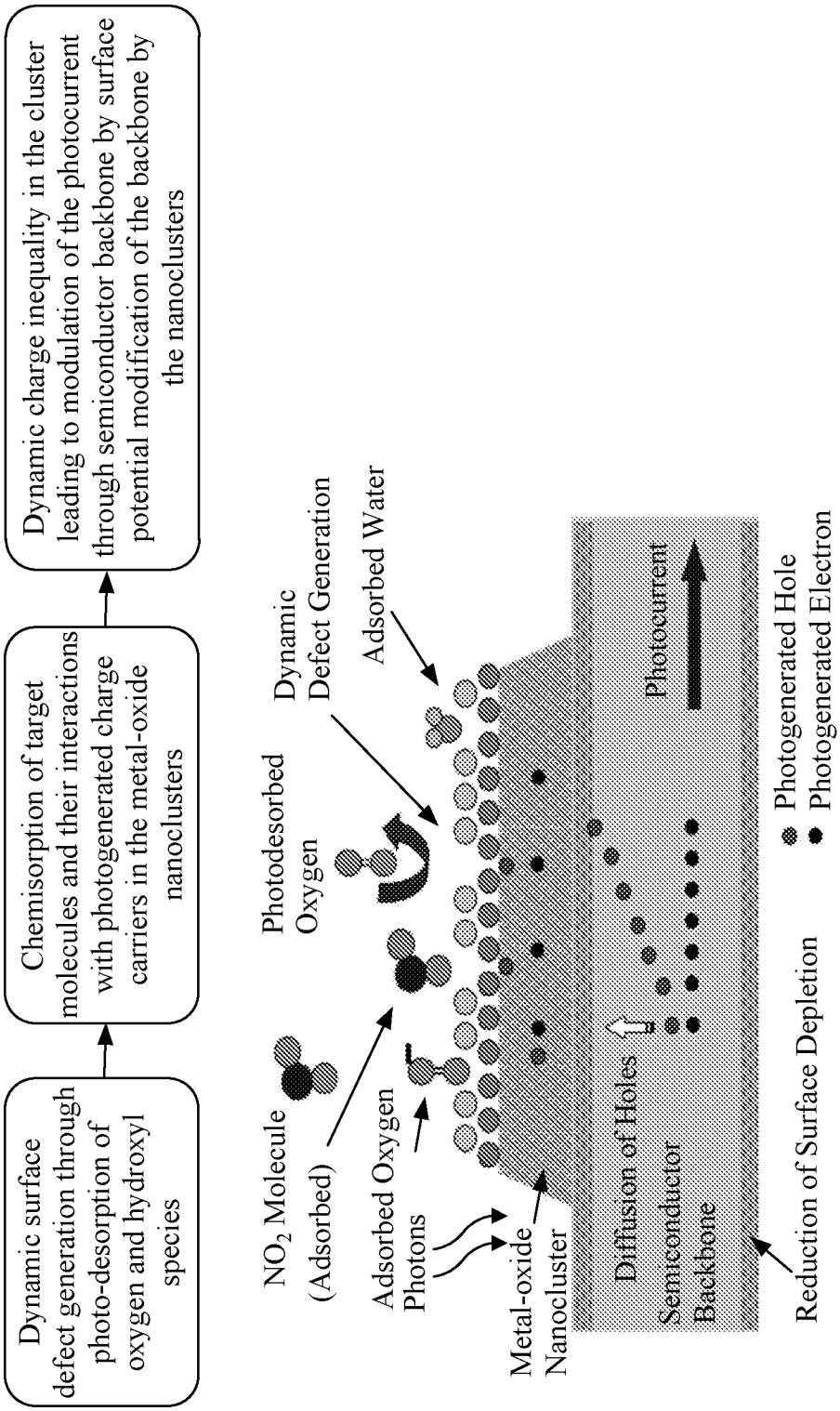

Dynamic surface defect generation through photo-desorption of oxygen and hydroxyl species
Chemisorption of target molecules and their interactions with photogenerated charge carriers in the metal-oxide nanoclusters
Dynamic charge inequality in the cluster leading to modulation of the photocurrent through semiconductor backbone by surface potential modification of the backbone by the nanoclusters
NO_2 Molecule (Adsorbed)
Photodesorbed Oxygen
Dynamic Defect Generation
Adsorbed Water
Adsorbed Oxygen
Photons
Metal-oxide Nanocluster
Diffusion of Holes
Semiconductor Backbone
Photocurrent
Reduction of Surface Depletion
Photogenerated Hole
Photogenerated Electron

FIGURE 11

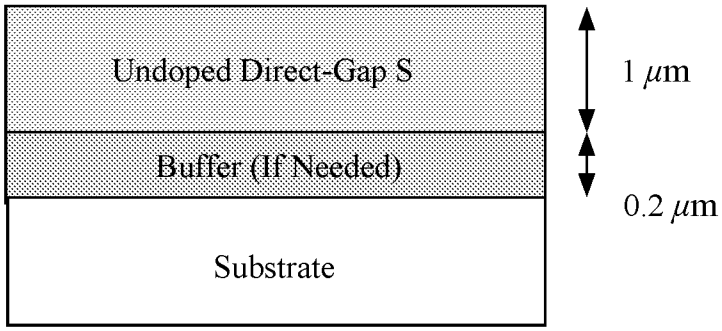
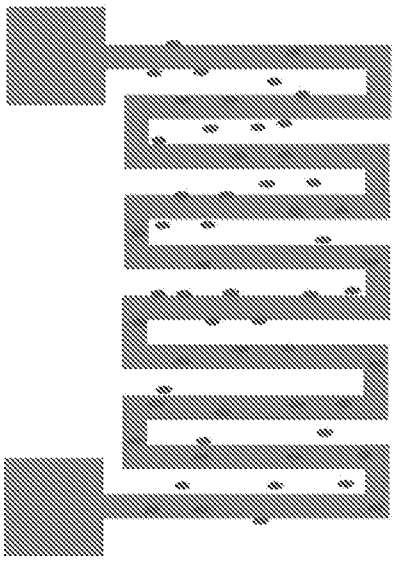
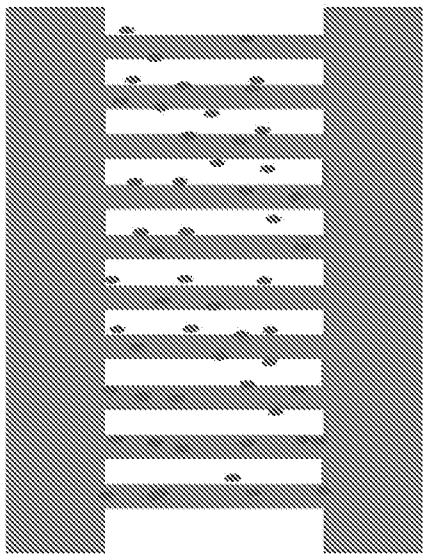


FIGURE 12A



Serial Architecture

FIGURE 12B



Parallel Architecture

FIGURE 13A

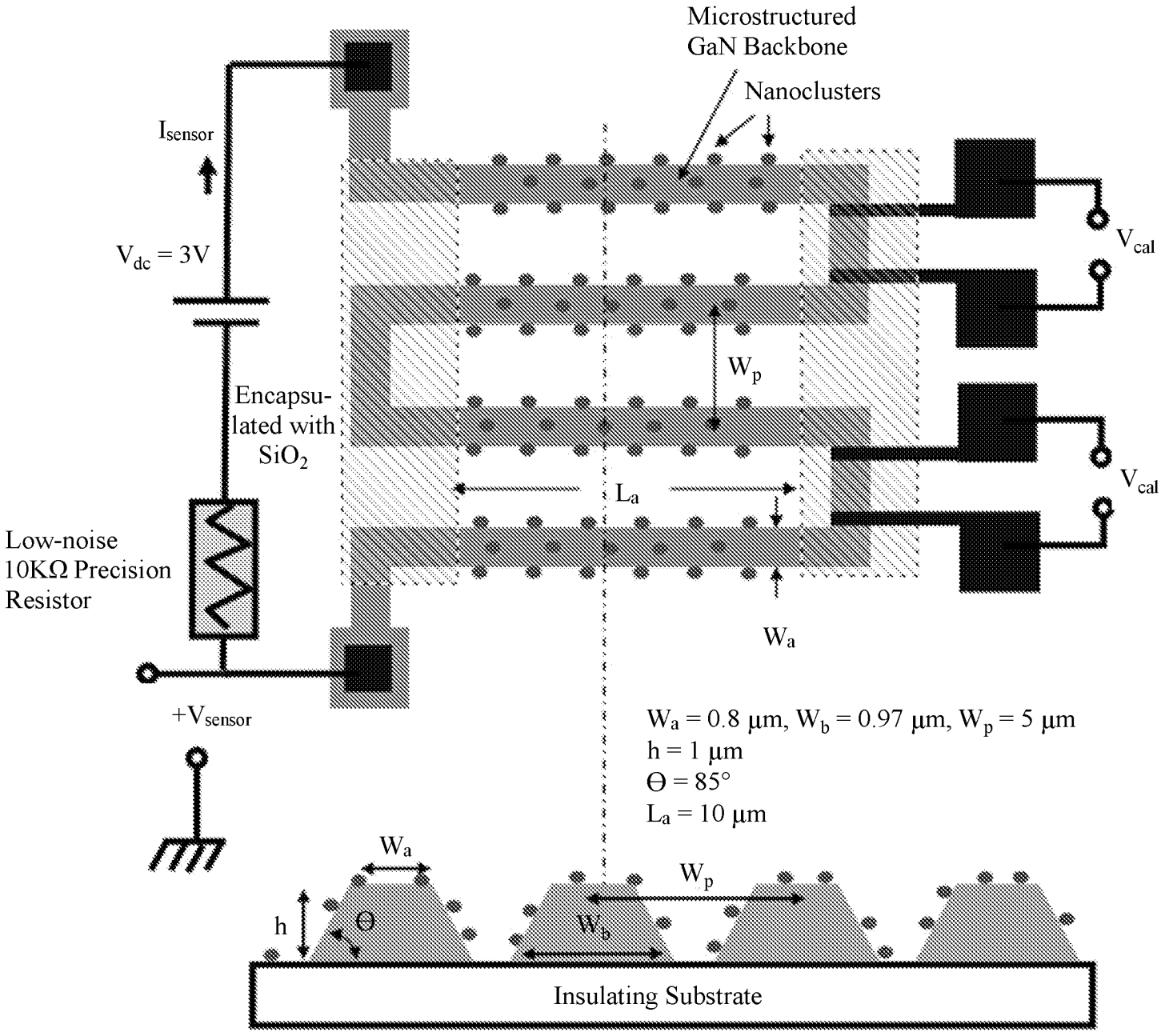


FIGURE 13B

FIGURE 14

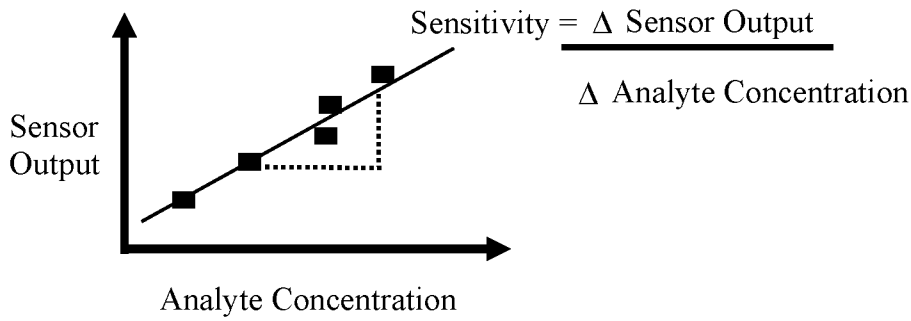


FIGURE 15

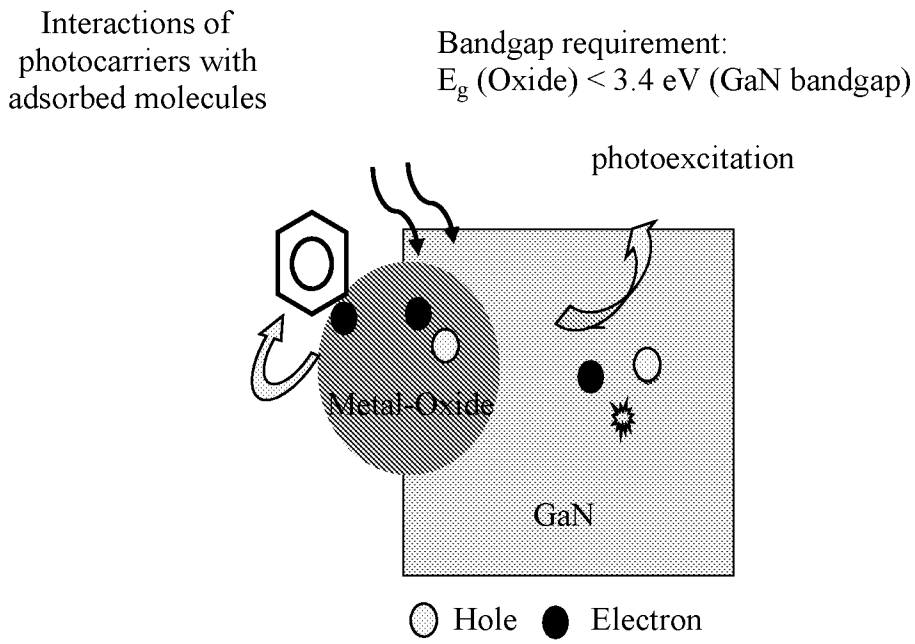


FIGURE 16

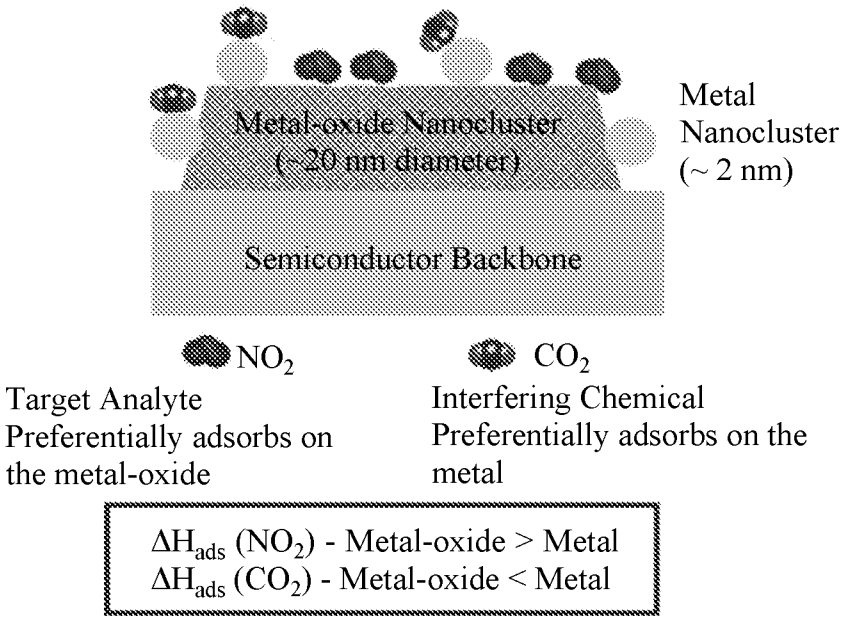


FIGURE 17

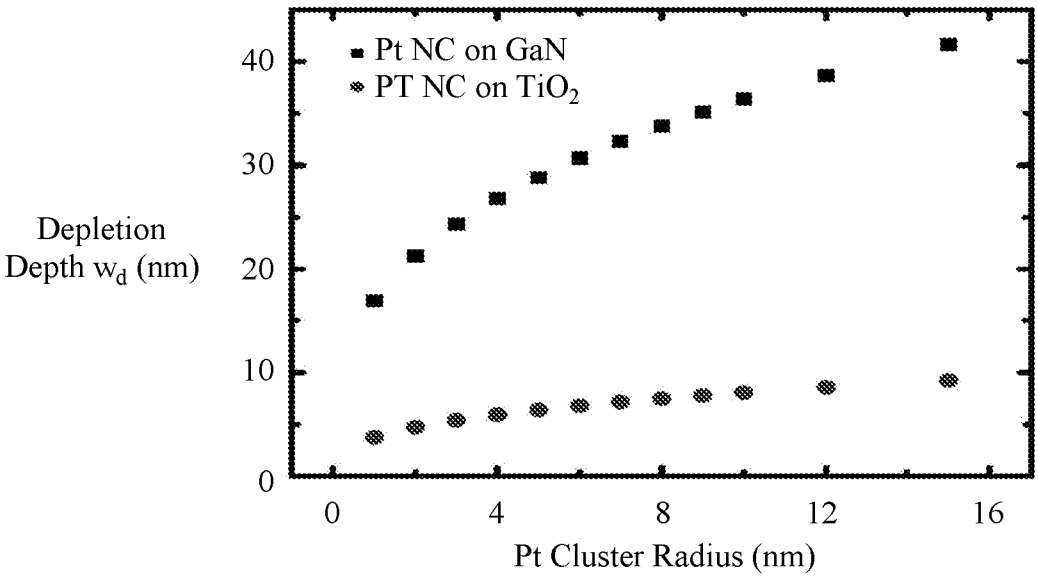


FIGURE 18

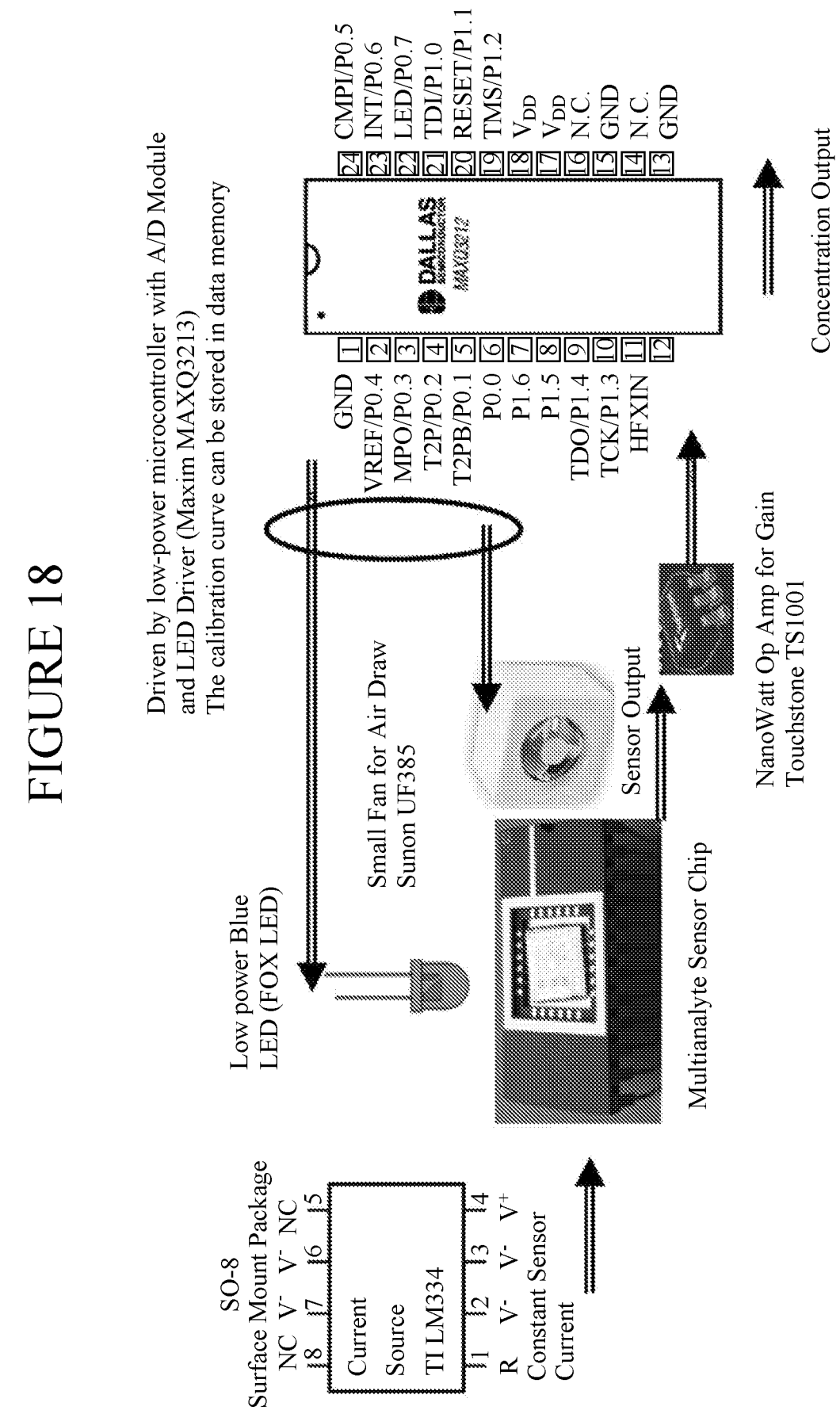

Driven by low-power microcontroller with A/D Module
and LED Driver (Maxim MAXQ3213)
The calibration curve can be stored in data memory
Low power Blue
LED (FOX LED)
Small Fan for Air Draw
Sunon UF385
Sensor Output
Multianalyte Sensor Chip
NanoWatt Op Amp for Gain
Touchstone TS1001
Concentration Output
SO-8
Surface Mount Package
NC V- V- NC
18 17 16 15
Current
Source
TI LM334
11 12 13 14
R V- V- V+
Constant Sensor
Current
GND 1
VREF/P0.4 2
MPO/P0.3 3
T2P/P0.2 4
T2PB/P0.1 5
P0.0 6
P1.6 7
P1.5 8
TDO/P1.4 9
TCK/P1.3 10
HFXIN 11
12
24 CMPI/P0.5
23 INT/P0.6
22 LED/P0.7
21 TDI/P1.0
20 RESET/P1.1
19 TMS/P1.2
18 V_{DD}
17 V_{DD}
16 N.C.
15 GND
14 N.C.
13 GND
DALLAS
MAXQ3213

FIGURE 19

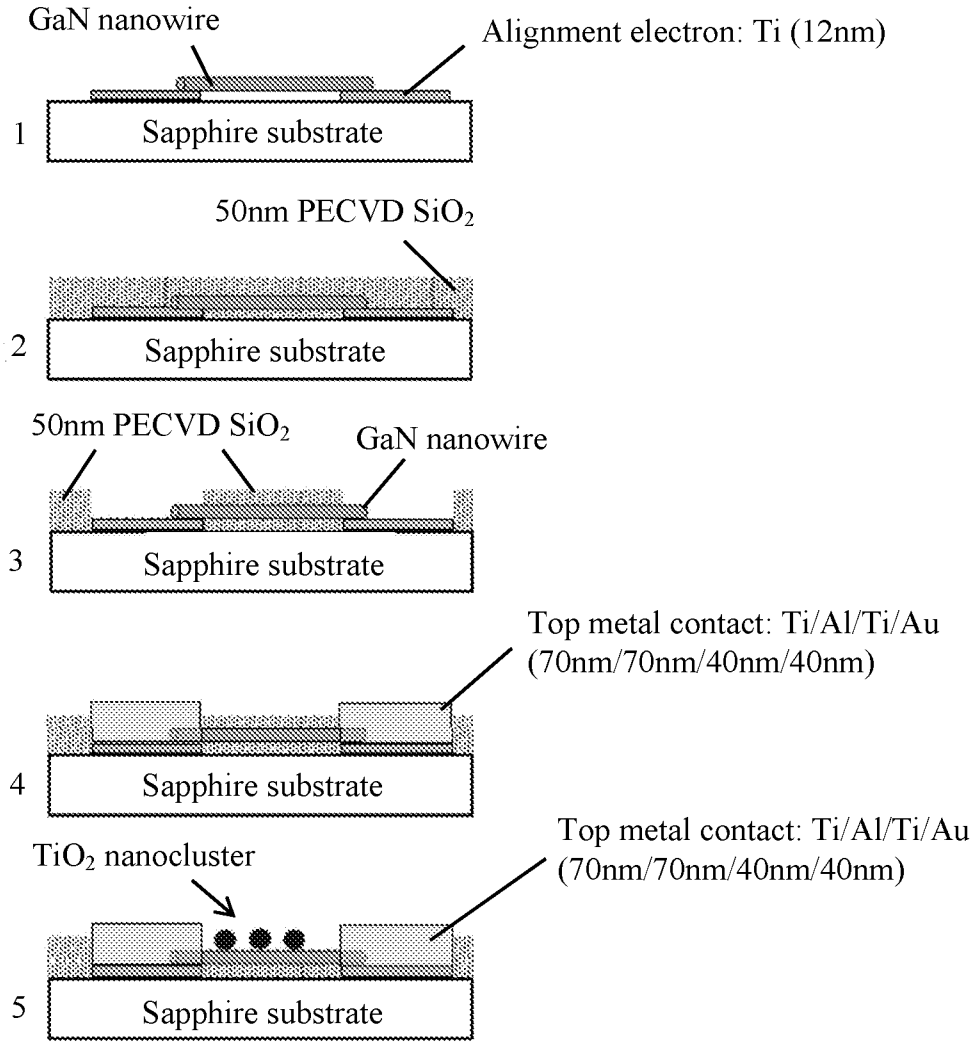

GaN nanowire
Alignment electron: Ti (12nm)
1
Sapphire substrate
50nm PECVD SiO_2
2
Sapphire substrate
50nm PECVD SiO_2
GaN nanowire
3
Sapphire substrate
Top metal contact: Ti/Al/Ti/Au
(70nm/70nm/40nm/40nm)
4
Sapphire substrate
TiO_2 nanocluster
Top metal contact: Ti/Al/Ti/Au
(70nm/70nm/40nm/40nm)
5
Sapphire substrate

FIGURE 20A

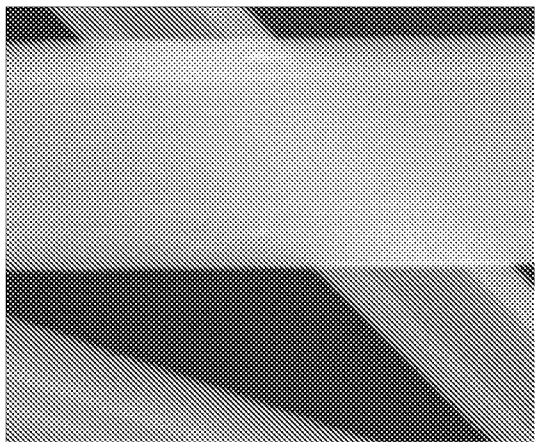


FIGURE 20B

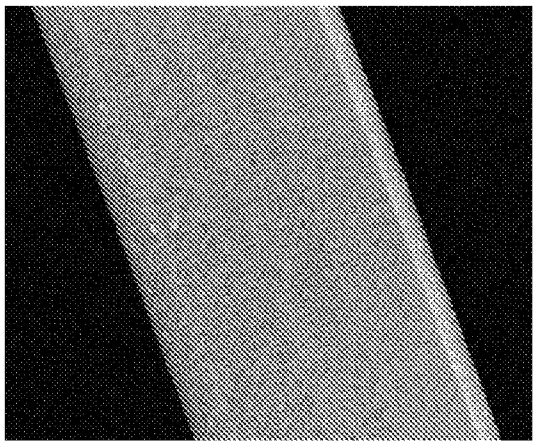


FIGURE 20C

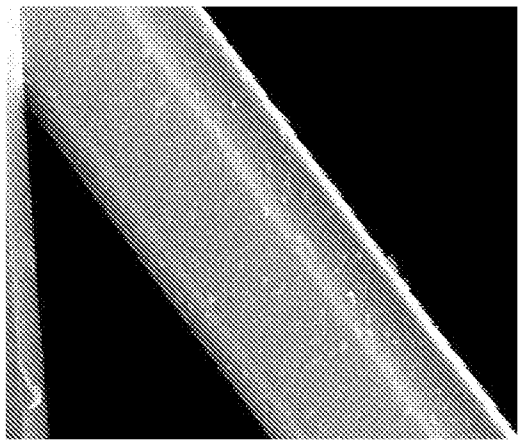


FIGURE 21

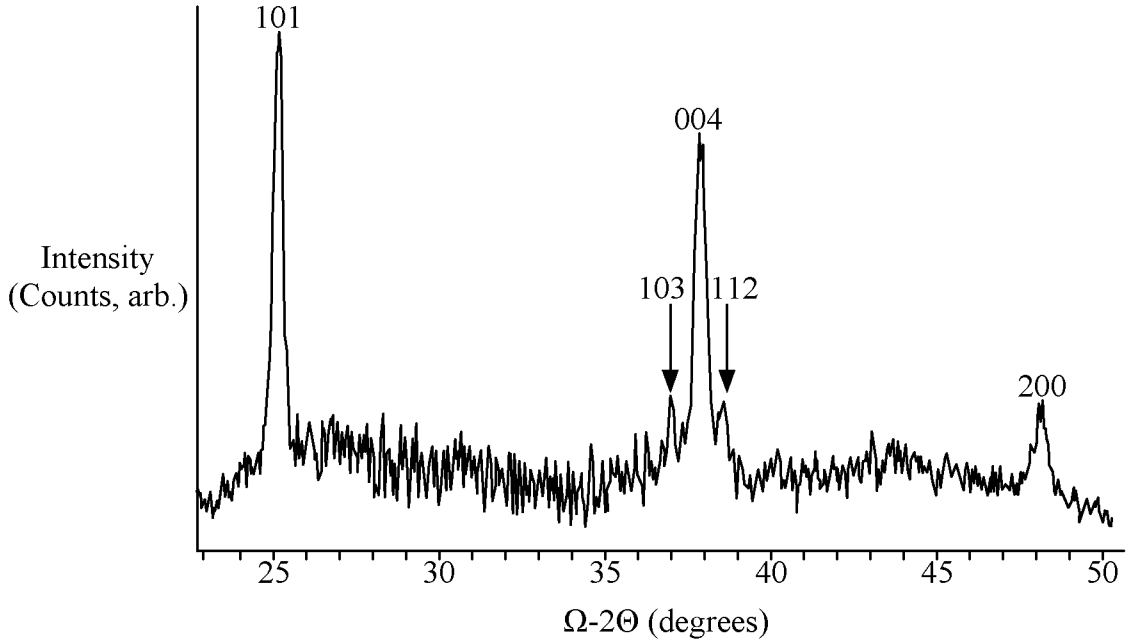

101
004
103
112
200
Intensity
(Counts, arb.)
25
30
35
40
45
50
Ω-2Θ (degrees)

FIGURE 22A

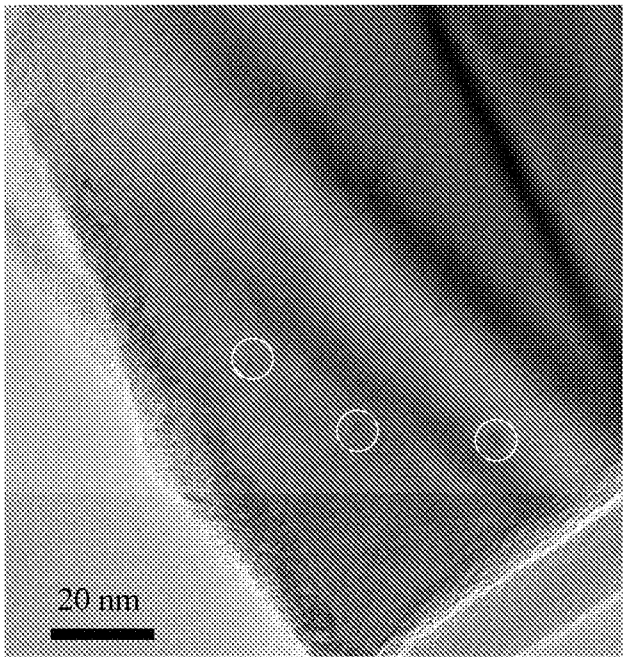


FIGURE 22B

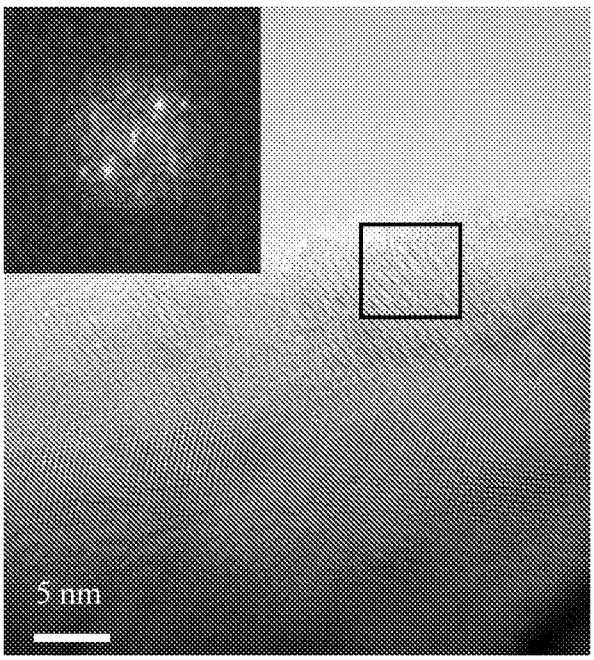
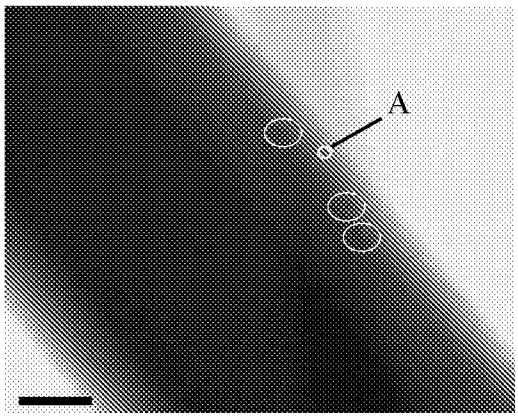
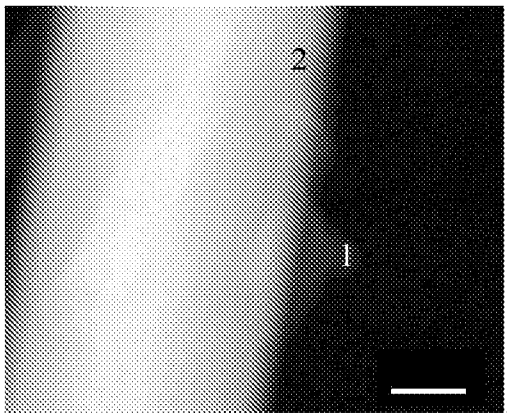


FIGURE 23A



50 nm

FIGURE 23B



20 nm

FIGURE 23C

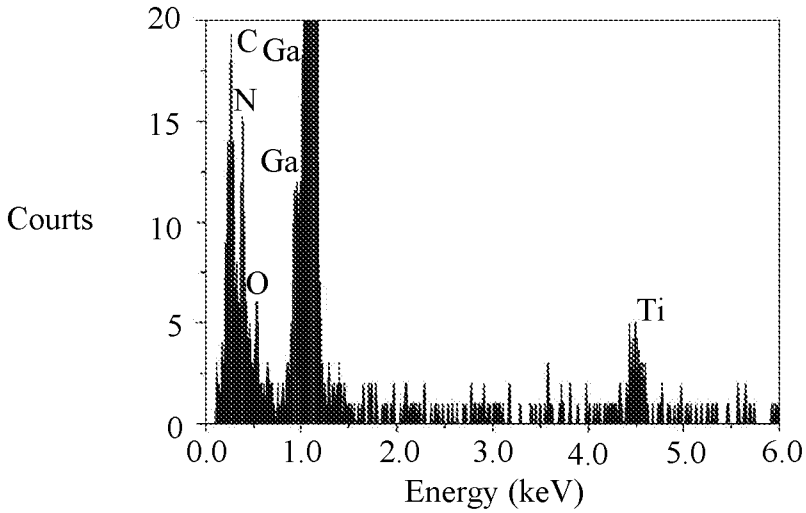


FIGURE 23D

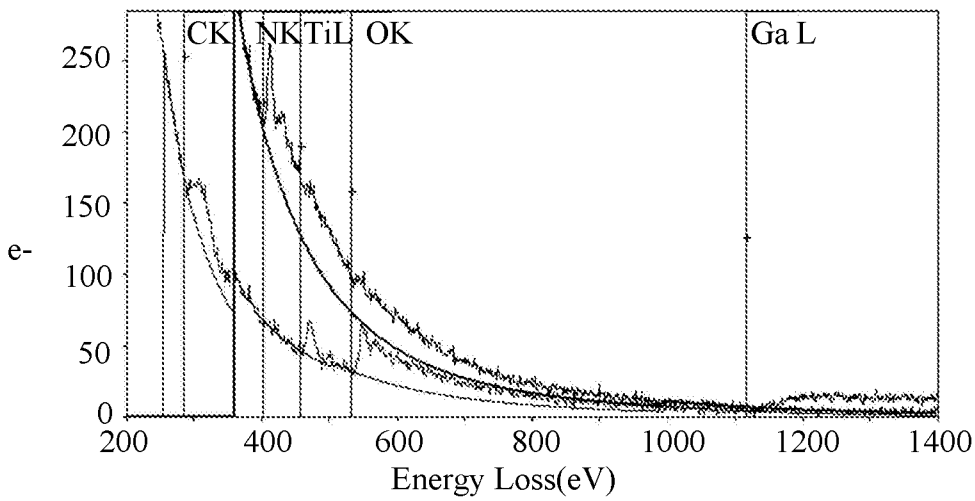


FIGURE 24

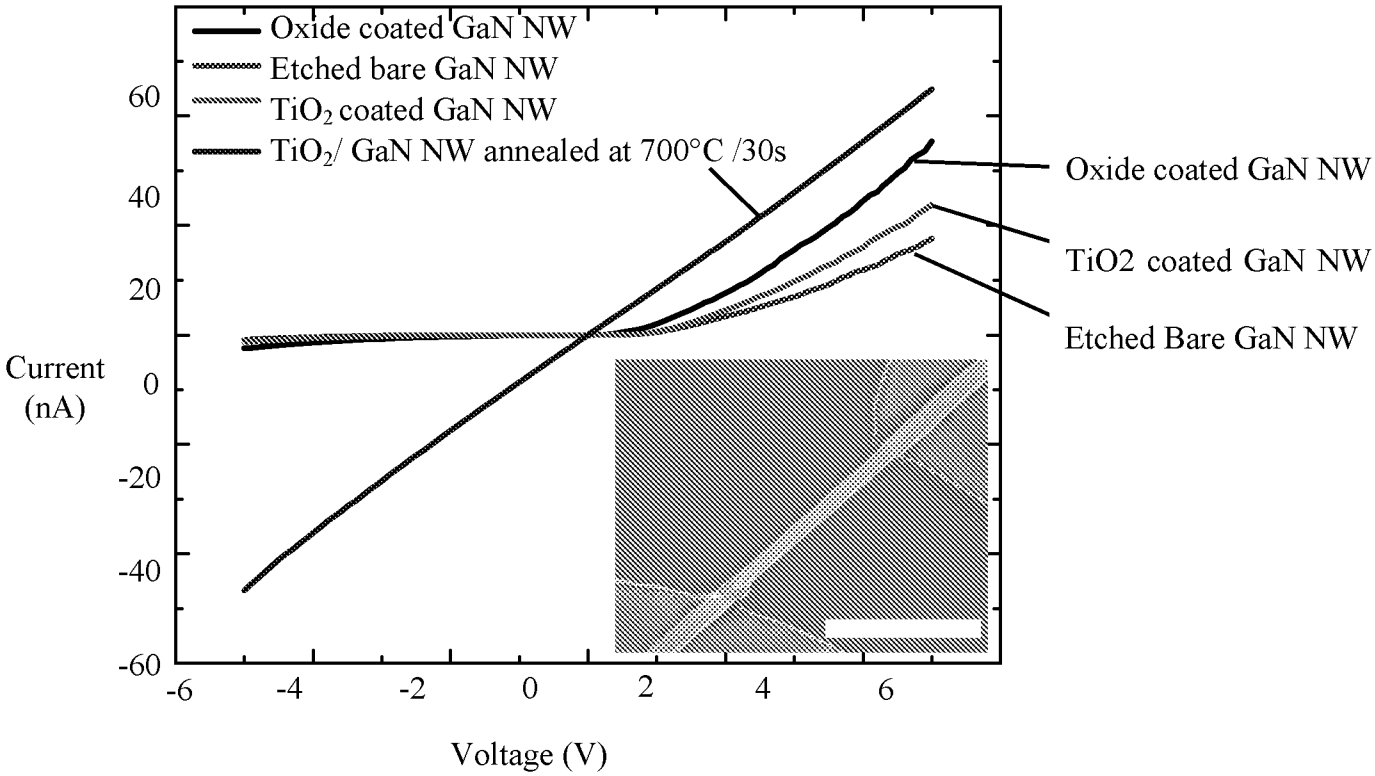

Oxide coated GaN NW
Etched bare GaN NW
TiO2 coated GaN NW
TiO2/ GaN NW annealed at 700°C /30s
Oxide coated GaN NW
TiO2 coated GaN NW
Etched Bare GaN NW
Current (nA)
60
40
20
0
-20
-40
-60
-6
-4
-2
0
2
4
6
Voltage (V)

FIGURE 25A

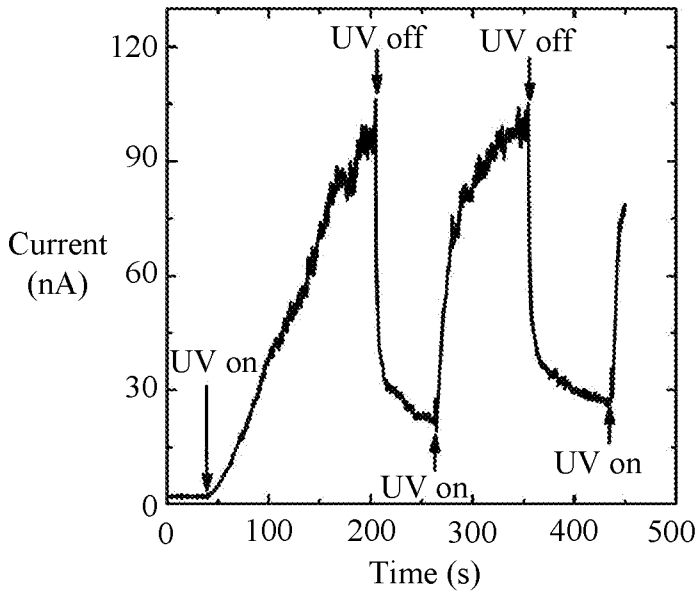


FIGURE 25B

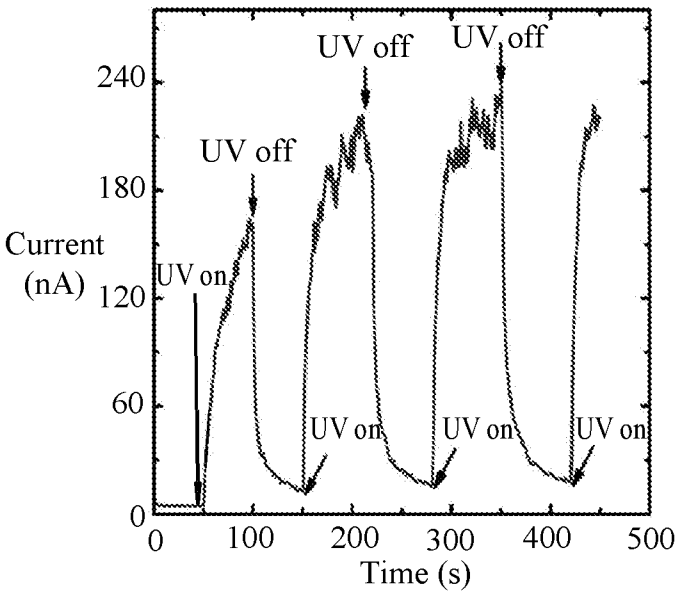


FIGURE 26

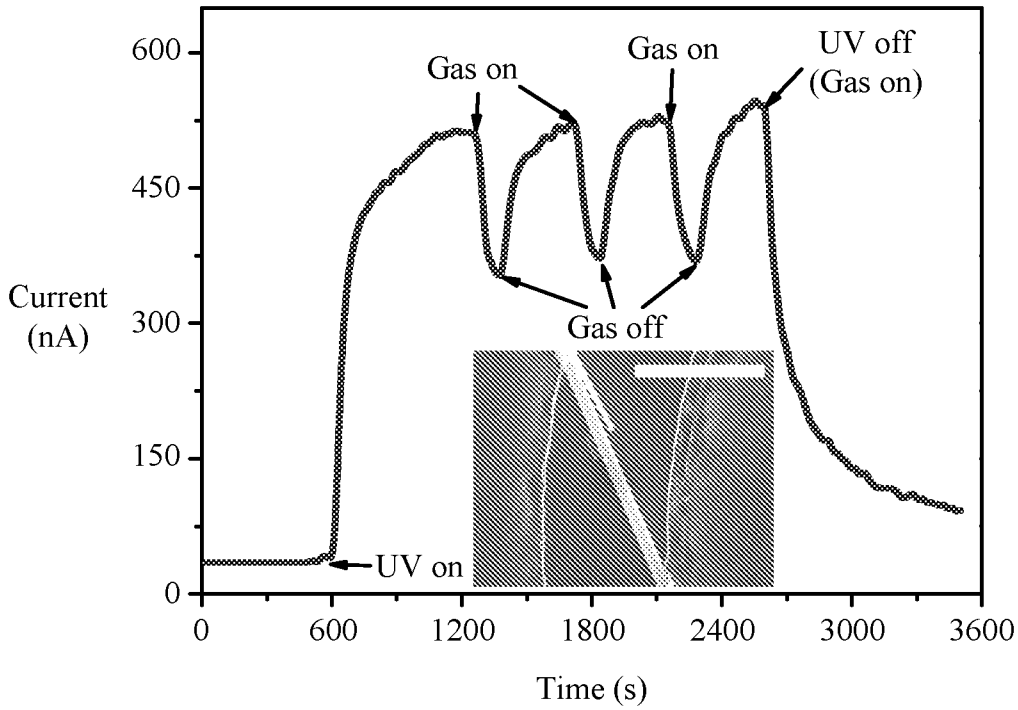


FIGURE 27A

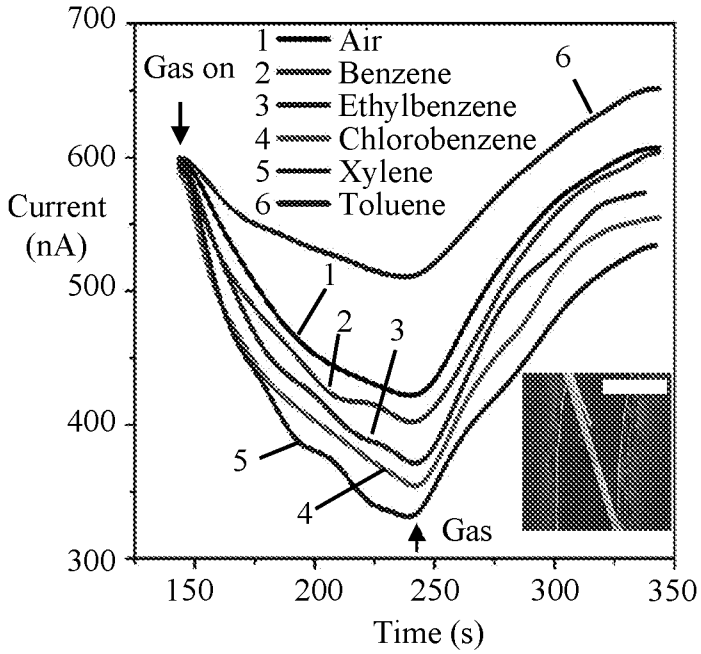


FIGURE 27B

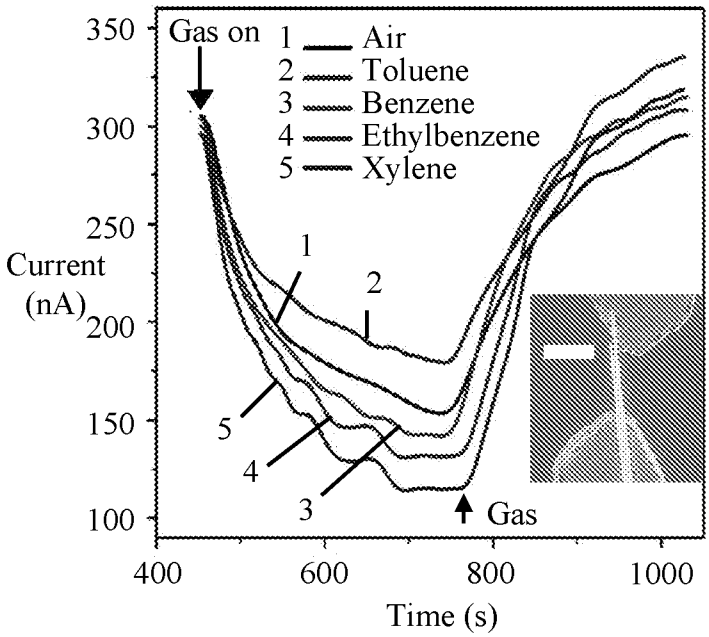


FIGURE 28A

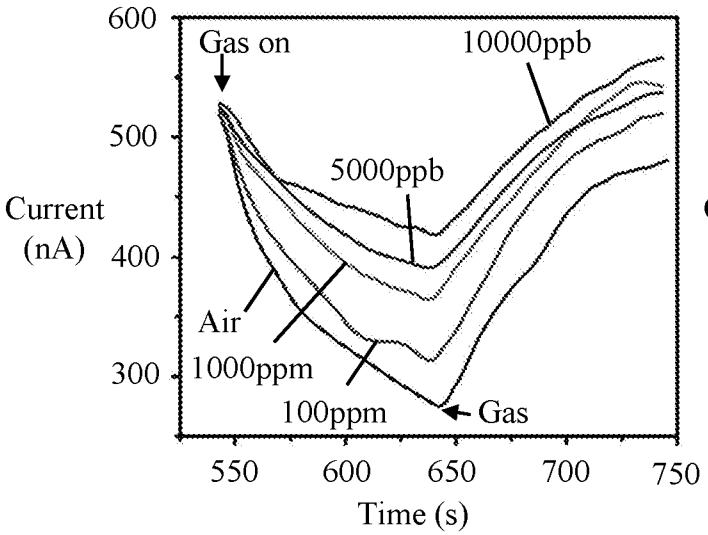


FIGURE 28B

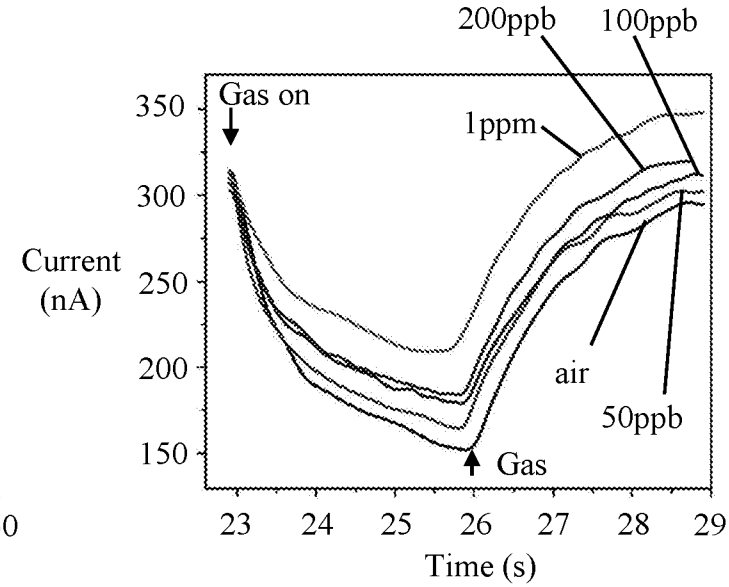


FIGURE 29

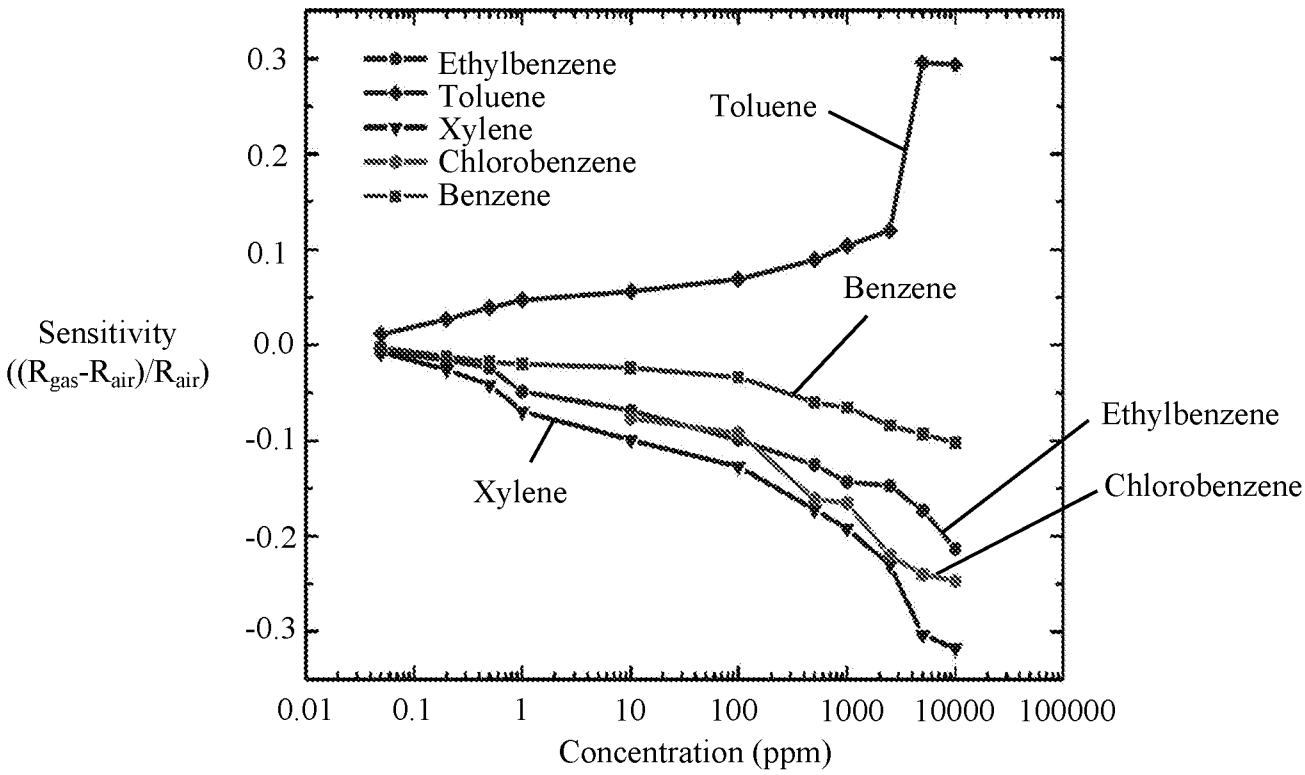

Ethylbenzene
Toluene
Xylene
Chlorobenzene
Benzene
Toluene
Benzene
Ethylbenzene
Chlorobenzene
Xylene
Sensitivity
((Rgas-Rair)/Rair)
0.3
0.2
0.1
0.0
-0.1
-0.2
-0.3
0.01
0.1
1
10
100
1000
10000
100000
Concentration (ppm)

FIGURE 30A

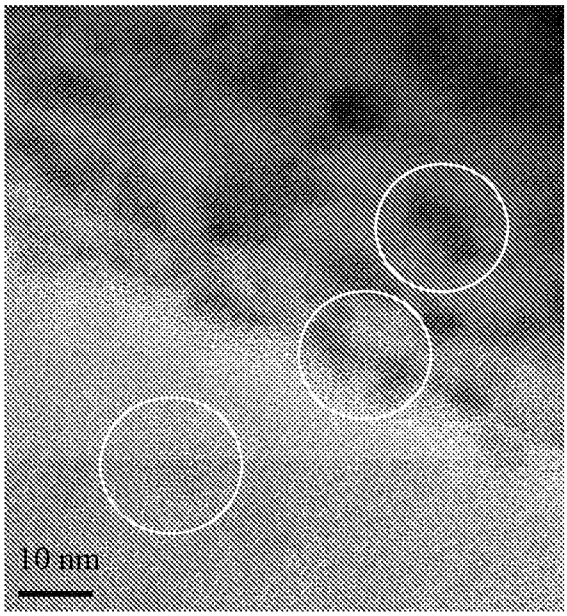


FIGURE 30B

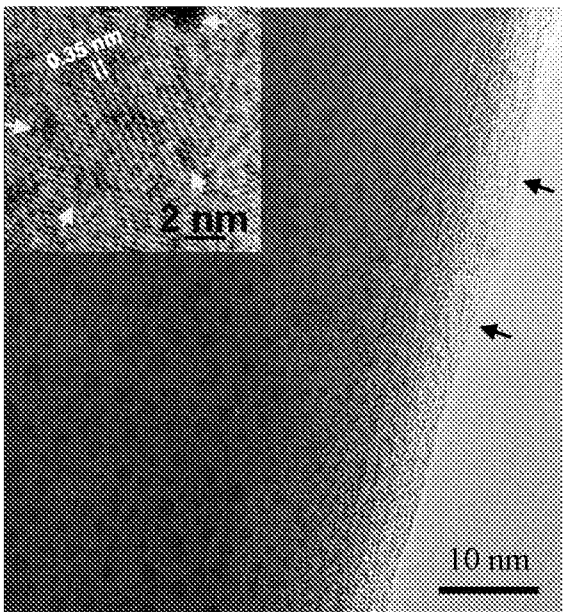
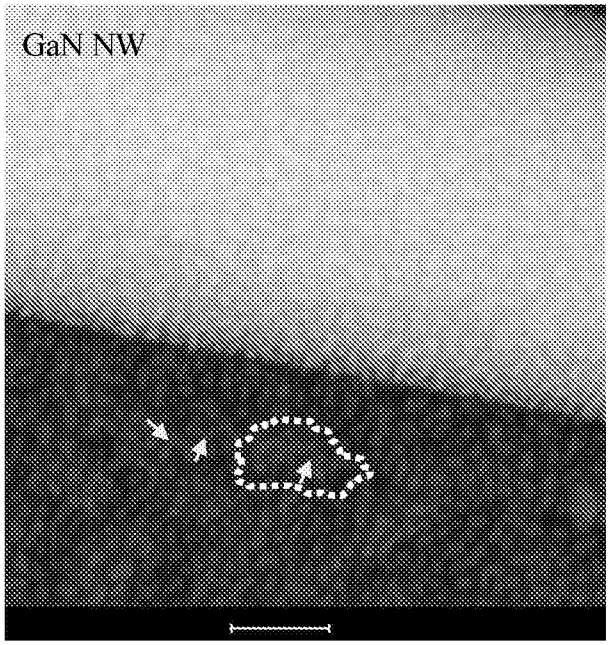
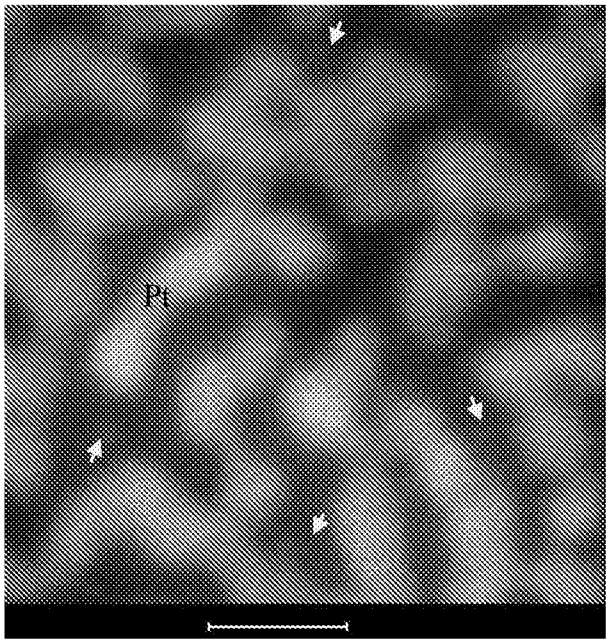


FIGURE 31A



20 nm

FIGURE 31B



5 nm

FIGURE 32A

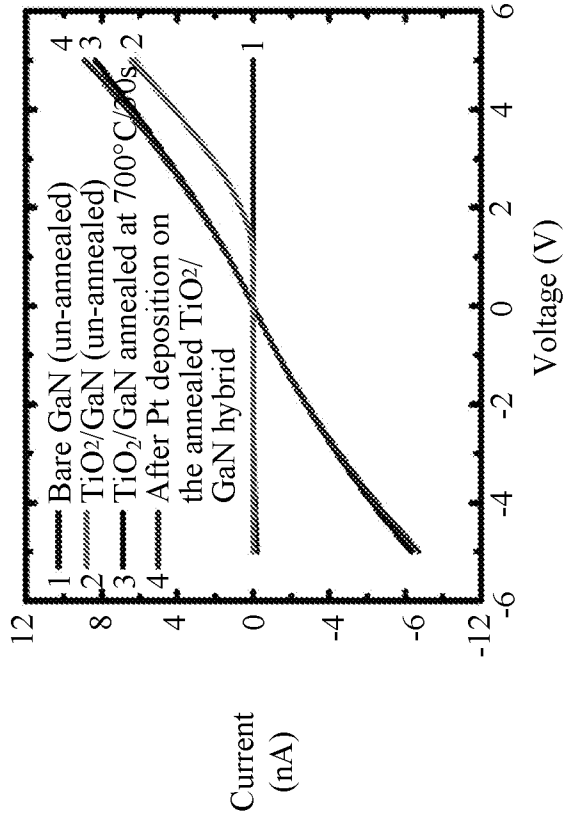


FIGURE 32B

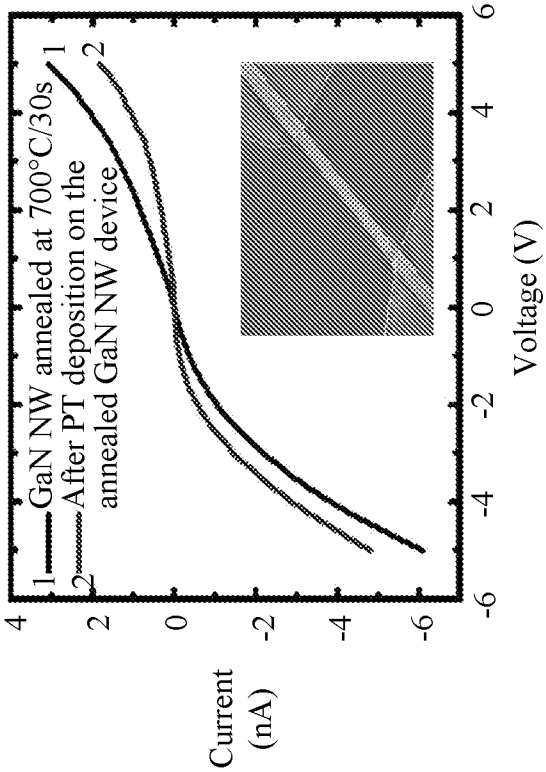


FIGURE 33

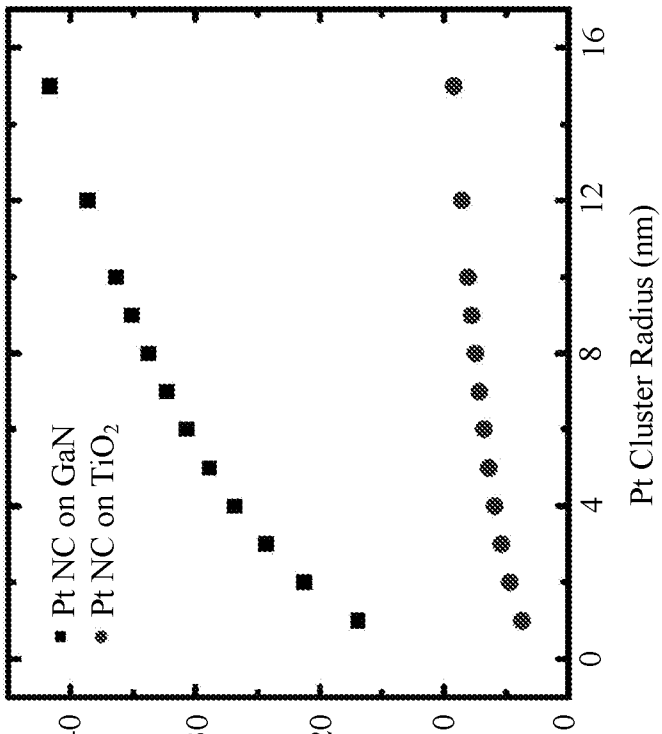


FIGURE 34

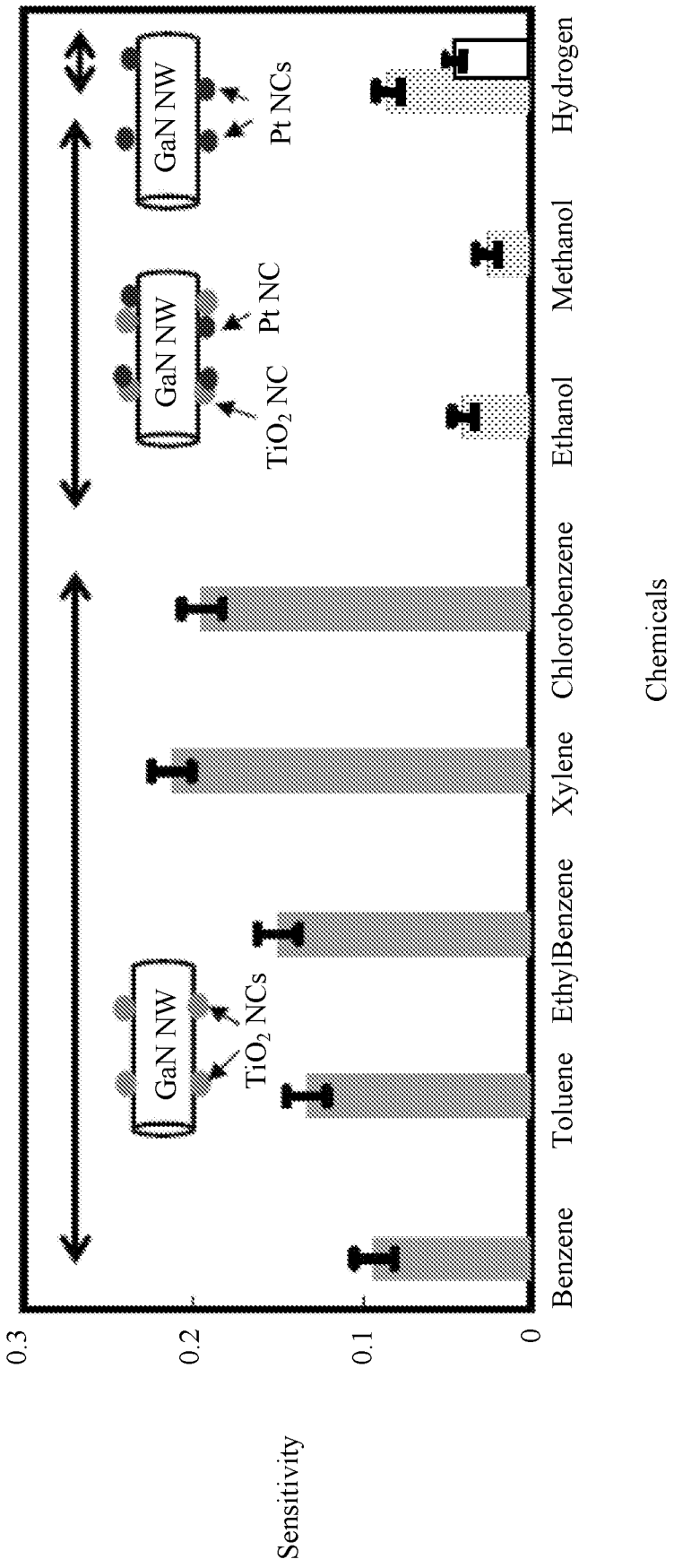

GaN NW
TiO_2 NCs
GaN NW
TiO_2 NC
Pt NC
GaN NW
Pt NCs
Benzene
Toluene
EthylBenzene
Xylene
Chlorobenzene
Ethanol
Methanol
Hydrogen
Chemicals
Sensitivity
0
0.1
0.2
0.3

FIGURE 35A

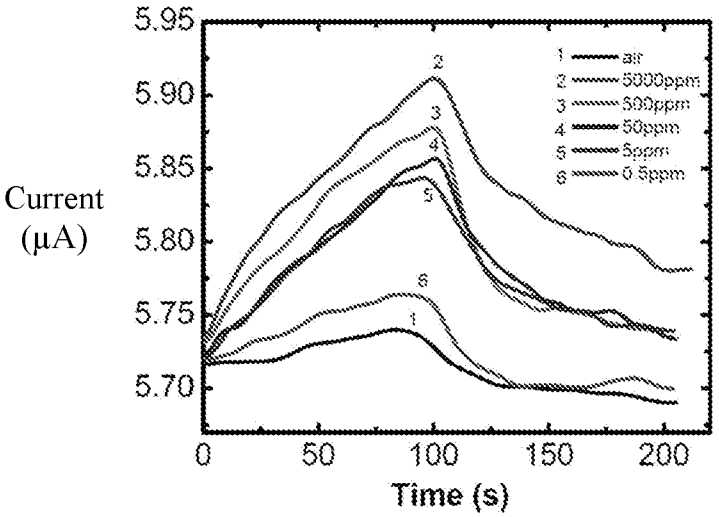


FIGURE 35B

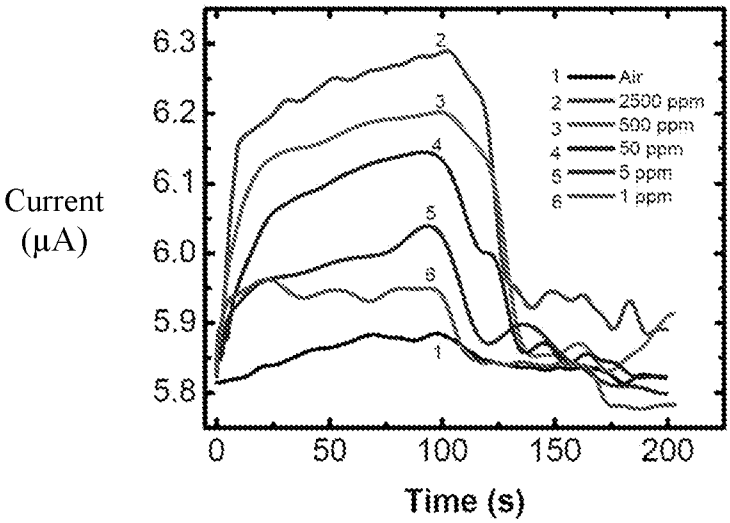


FIGURE 36A

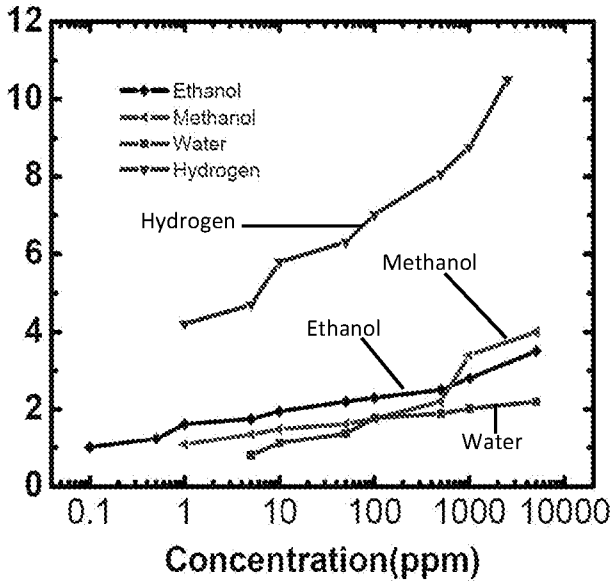


FIGURE 36B

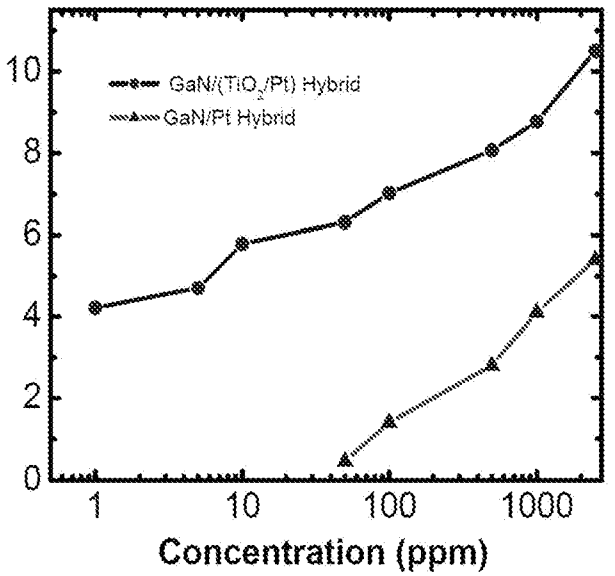
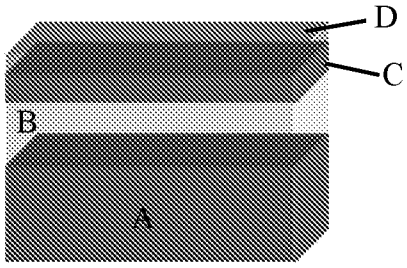


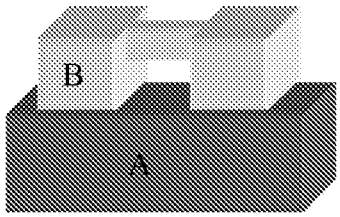
FIGURE 37

Deep UV Lithography



1

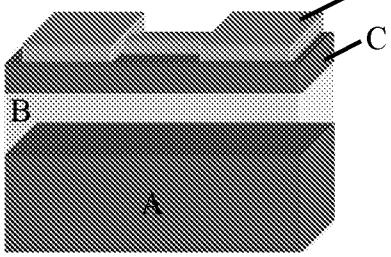
Removal of Plasma Damage Using Wet Etching



5

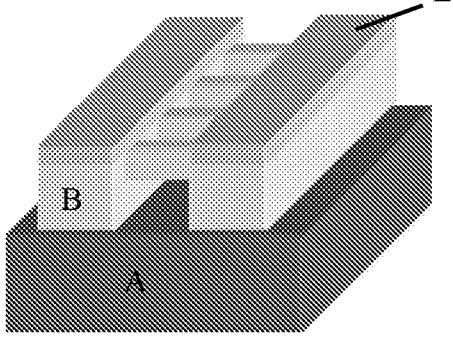
A -Si/Sapphire substrate
B -Direct-gap semiconductor (e.g.GaN) epilayer (1-1.5 microns thick)
C -Plasma-enhanced chemical deposition silicon dioxide
D -Ni mask for dry etch (suitable for nitrides composite with PECVD silicon dioxide)
E -Contact Electrodes Stack
F -Nanoclusters (Oxide and Metals)

Negative Resist Profile



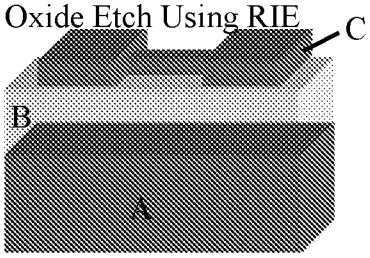
2

Ohmic Contract Deposition



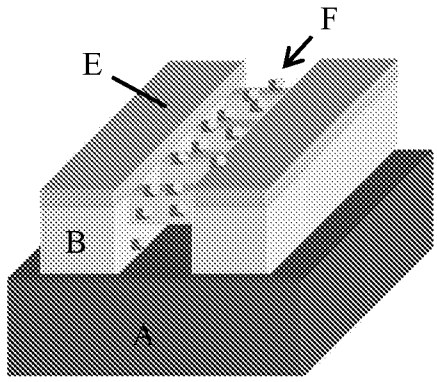
6

Pattern Transfer to Oxide Using Oxide Etch Using RIE



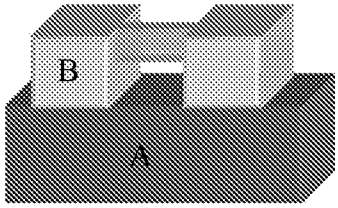
3

Multicomponent Nanocluster Deposition



7

Pattern Transfer to Semiconductor Epilayer Using ICP



4

FIGURE 38A

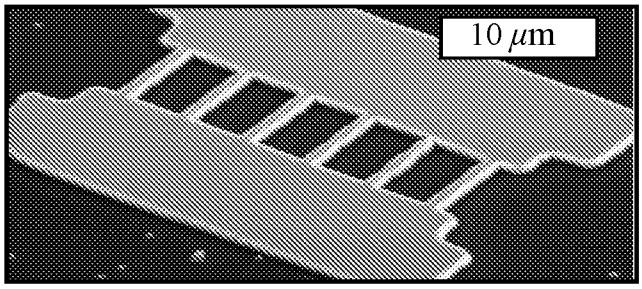


FIGURE 38B

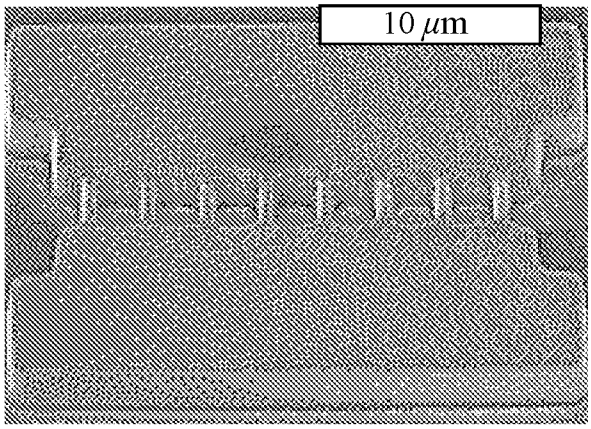


FIGURE 39

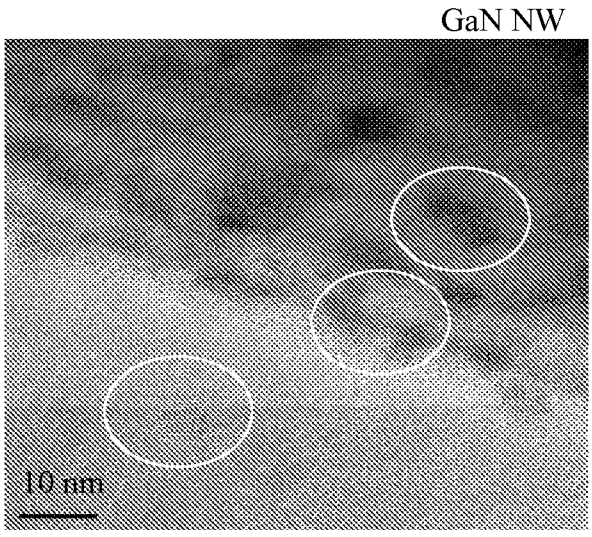


FIGURE 40

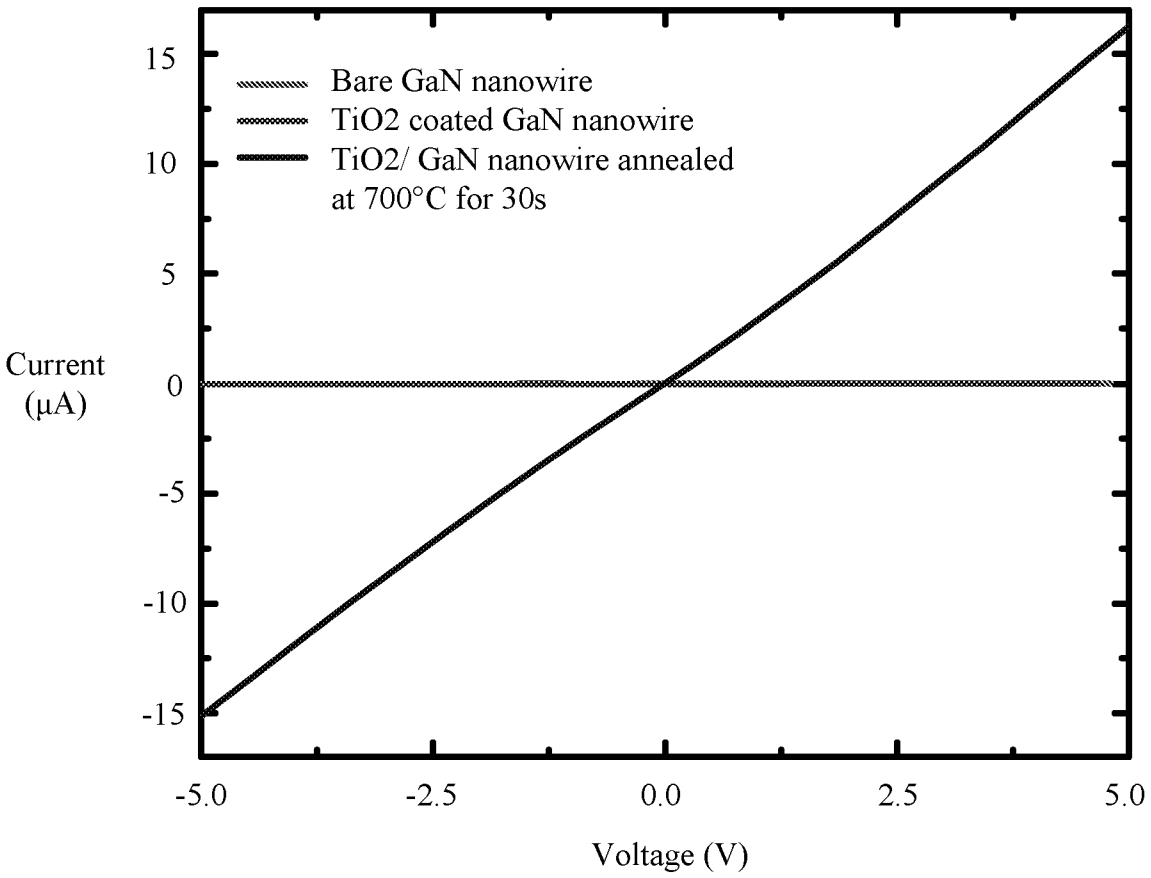

Bare GaN nanowire
TiO2 coated GaN nanowire
TiO2/ GaN nanowire annealed at 700°C for 30s
Current (μA)
15
10
5
0
-5
-10
-15
-5.0
-2.5
0.0
2.5
5.0
Voltage (V)

FIGURE 41A

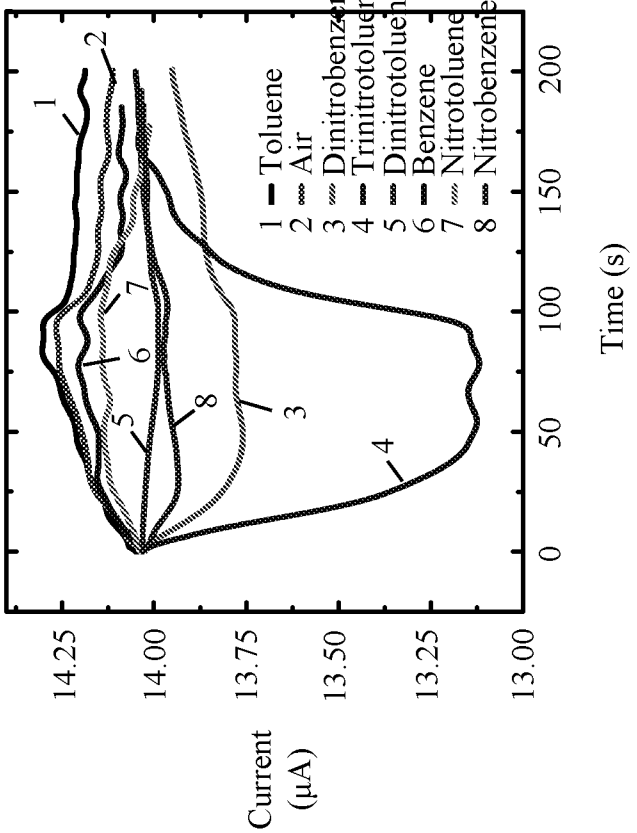


FIGURE 41B

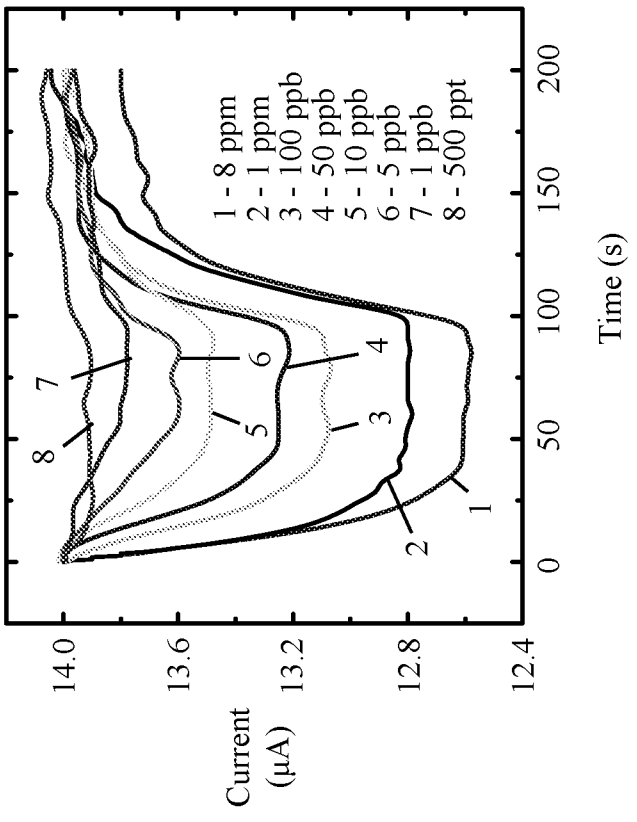


FIGURE 42

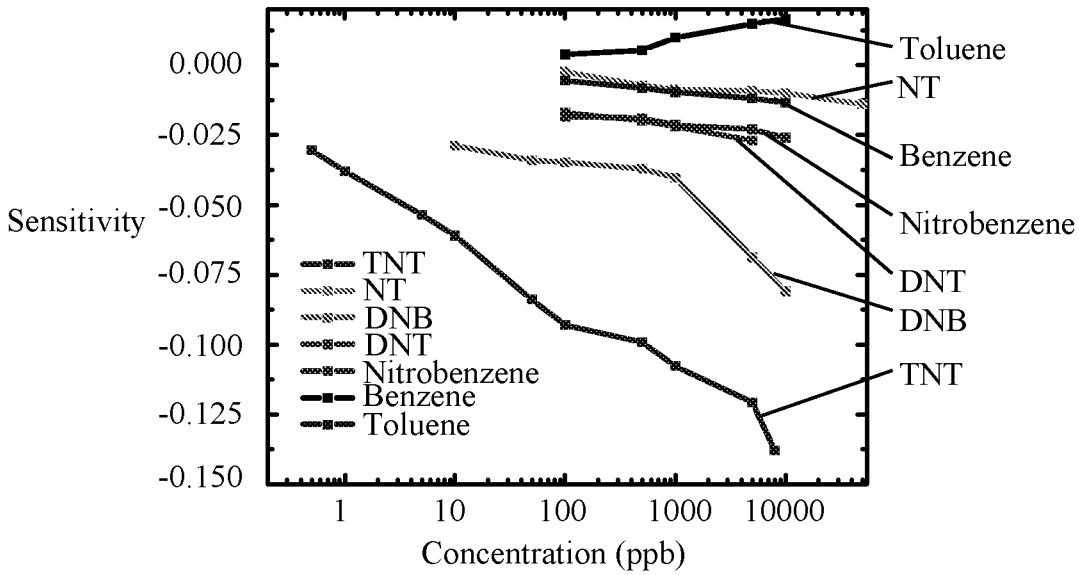


FIGURE 43

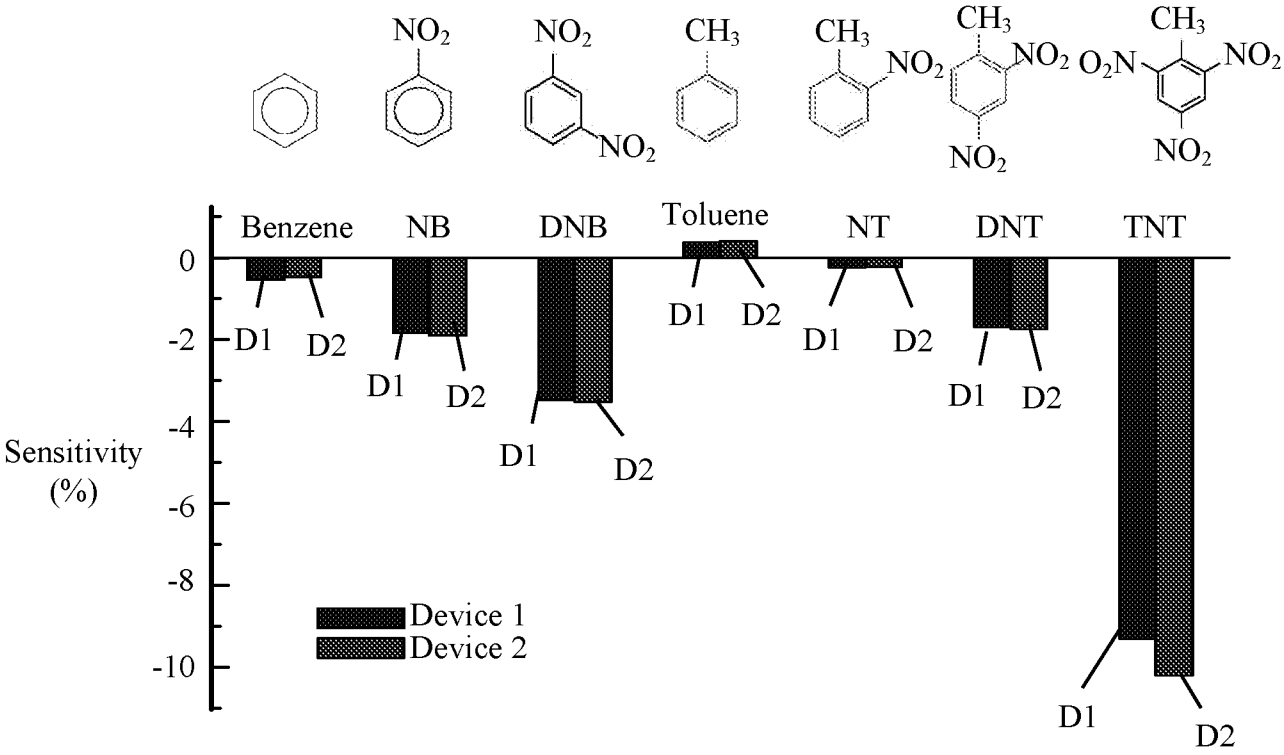


FIGURE 44

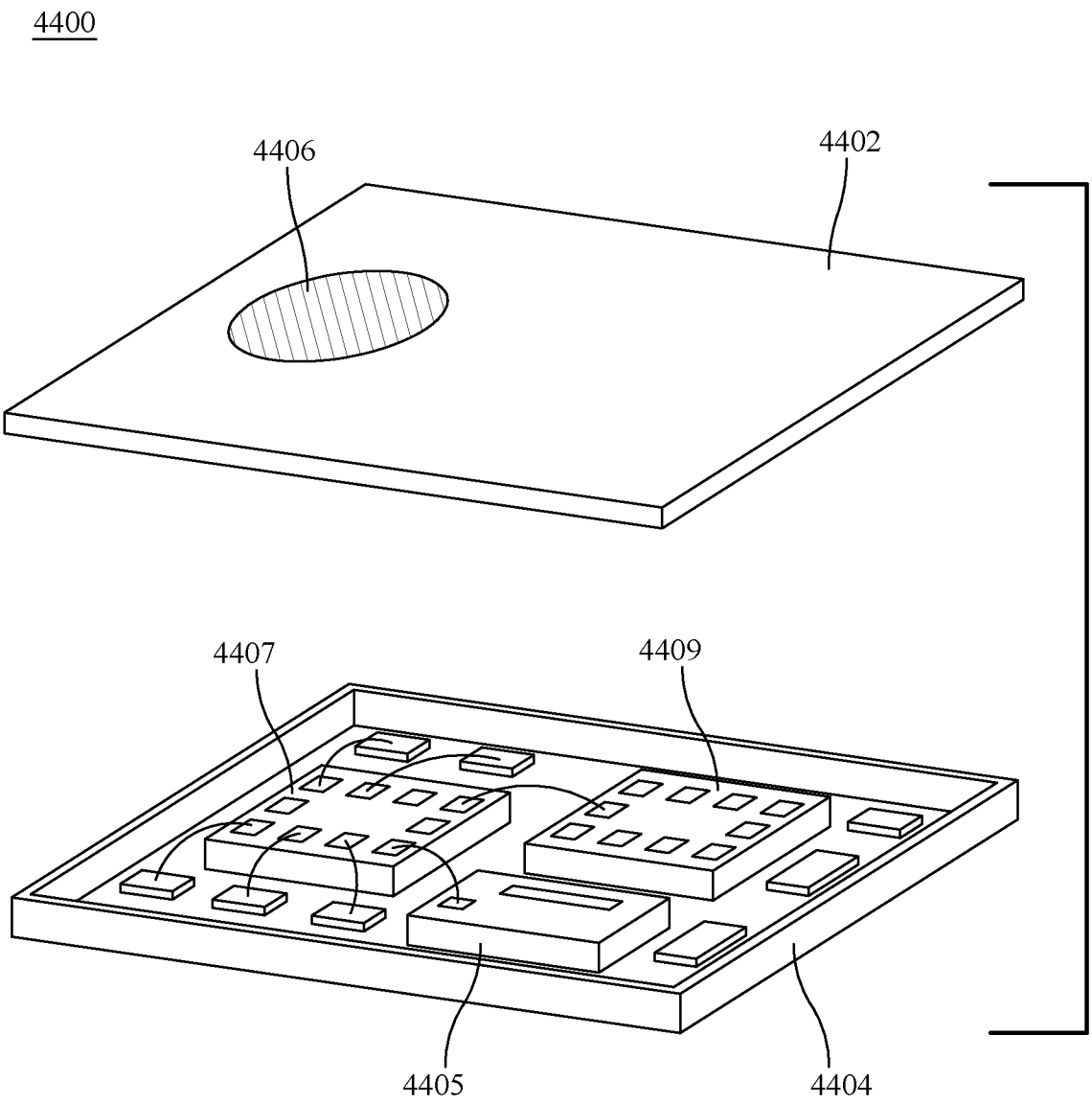


FIGURE 45

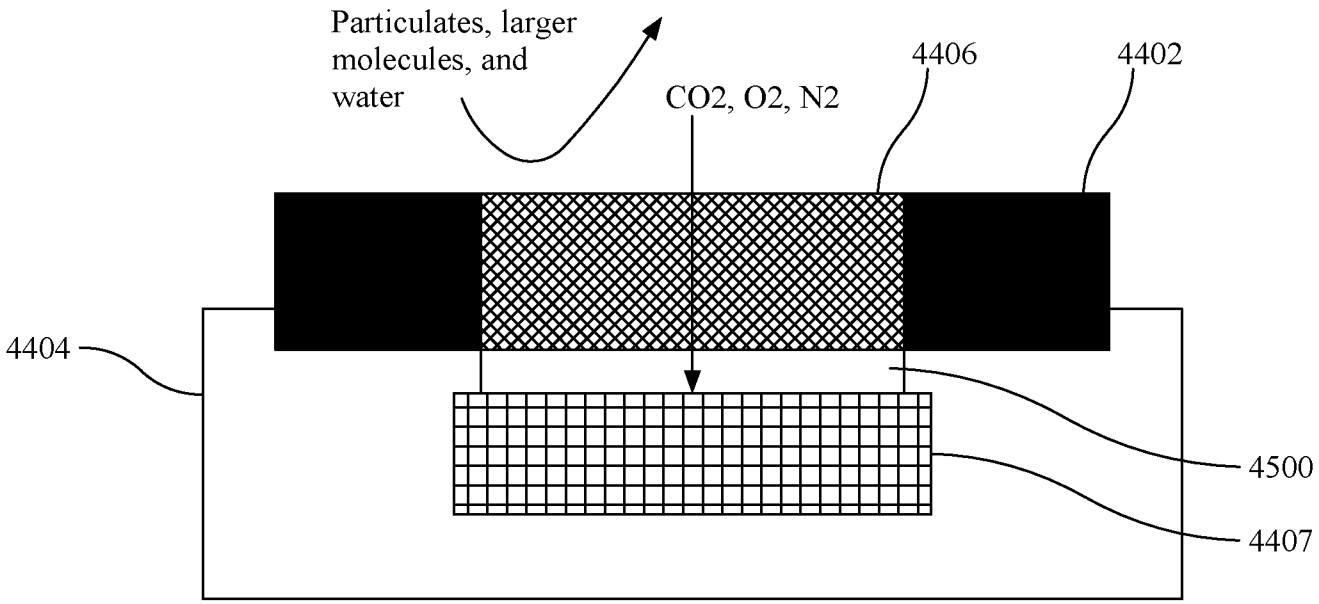

Particulates, larger molecules, and water
CO2, O2, N2
4406
4402
4404
4500
4407

FIGURE 46

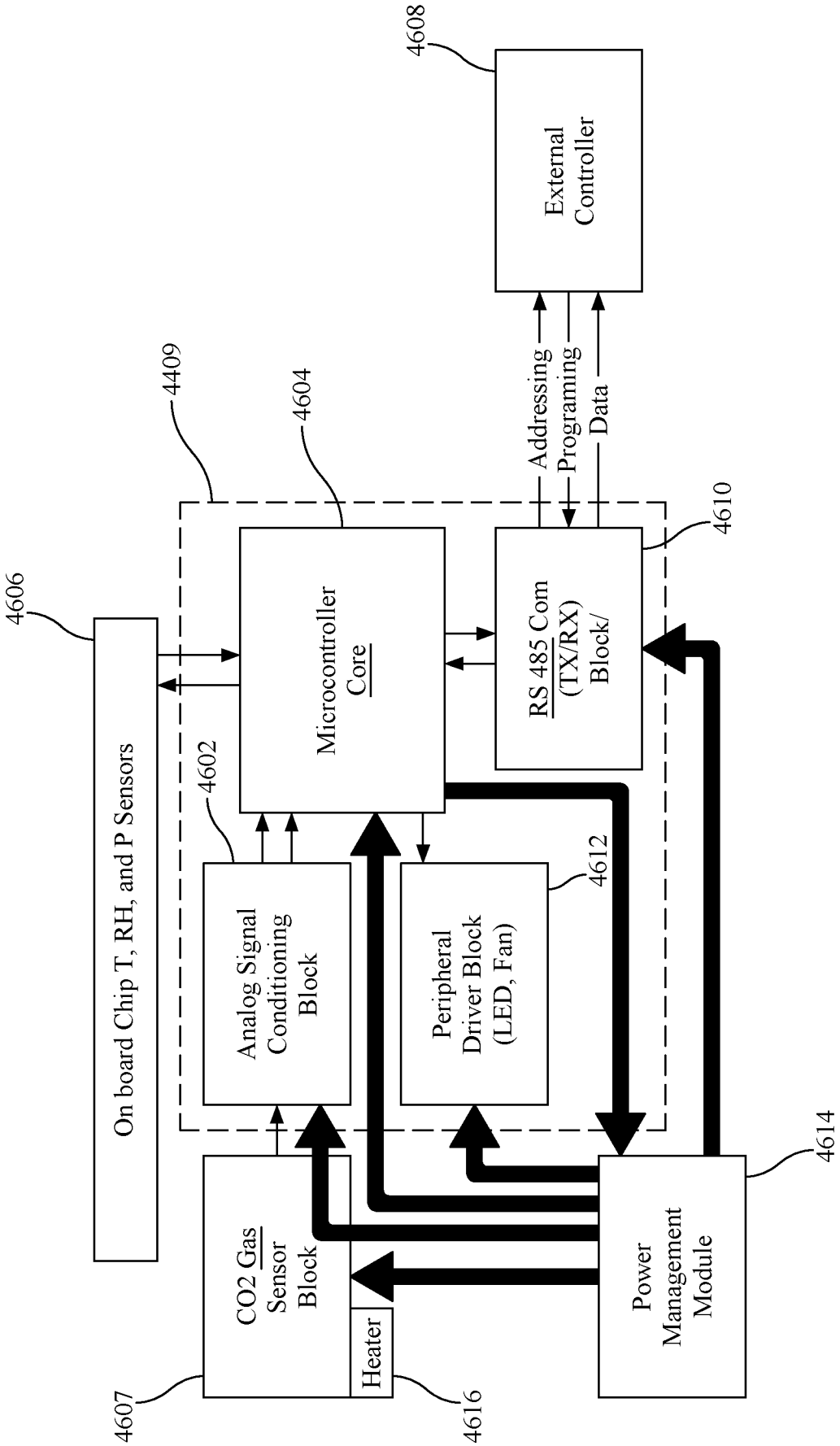

4608
External Controller
Addressing
Programing
Data
4409
4604
4610
4606
Microcontroller Core
RS 485 Com (TX/RX) Block/
On board Chip T, RH, and P Sensors
4602
Analog Signal Conditioning Block
Peripheral Driver Block (LED, Fan)
4612
4614
CO2 Gas Sensor Block
Heater
Power Management Module
4607
4616

FIGURE 47

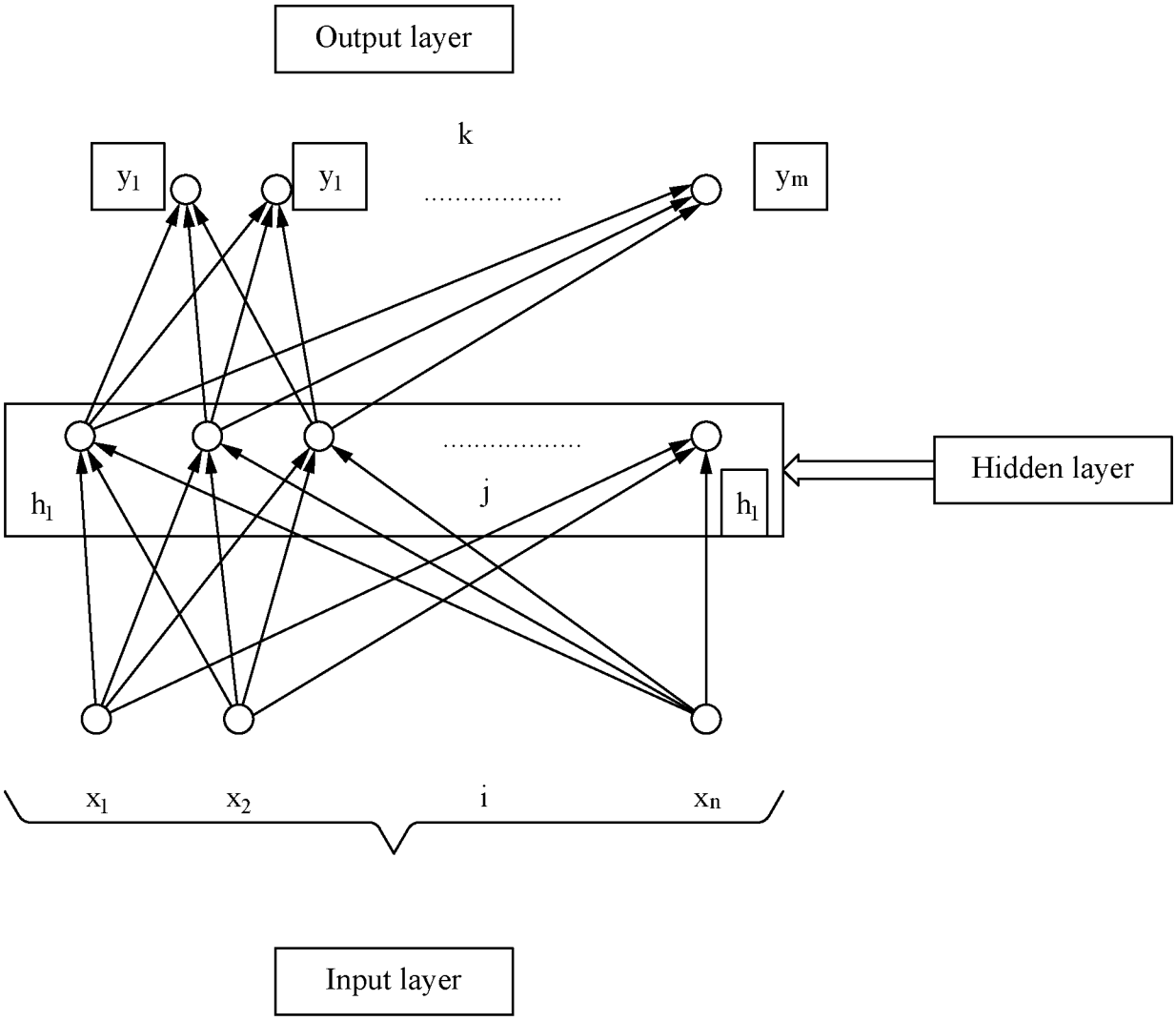
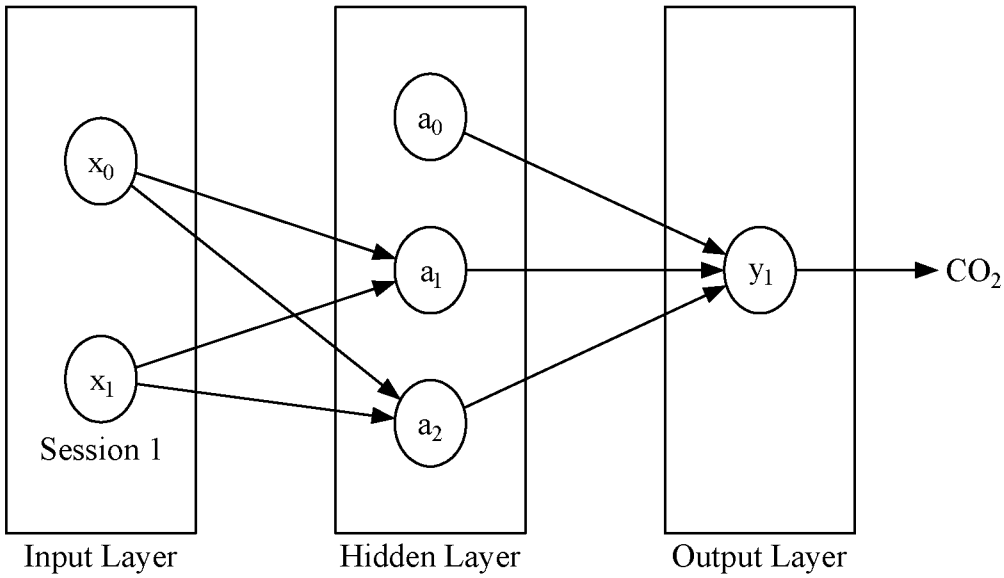

Output layer
k
y1
y1
.....
ym
.....
h1
j
h1
Hidden layer
x1
x2
i
xn
Input layer

FIGURE 48


x_0
x_1
Session 1
a_0
a_1
a_2
y_1
CO_2
Input Layer
Hidden Layer
Output Layer

4900

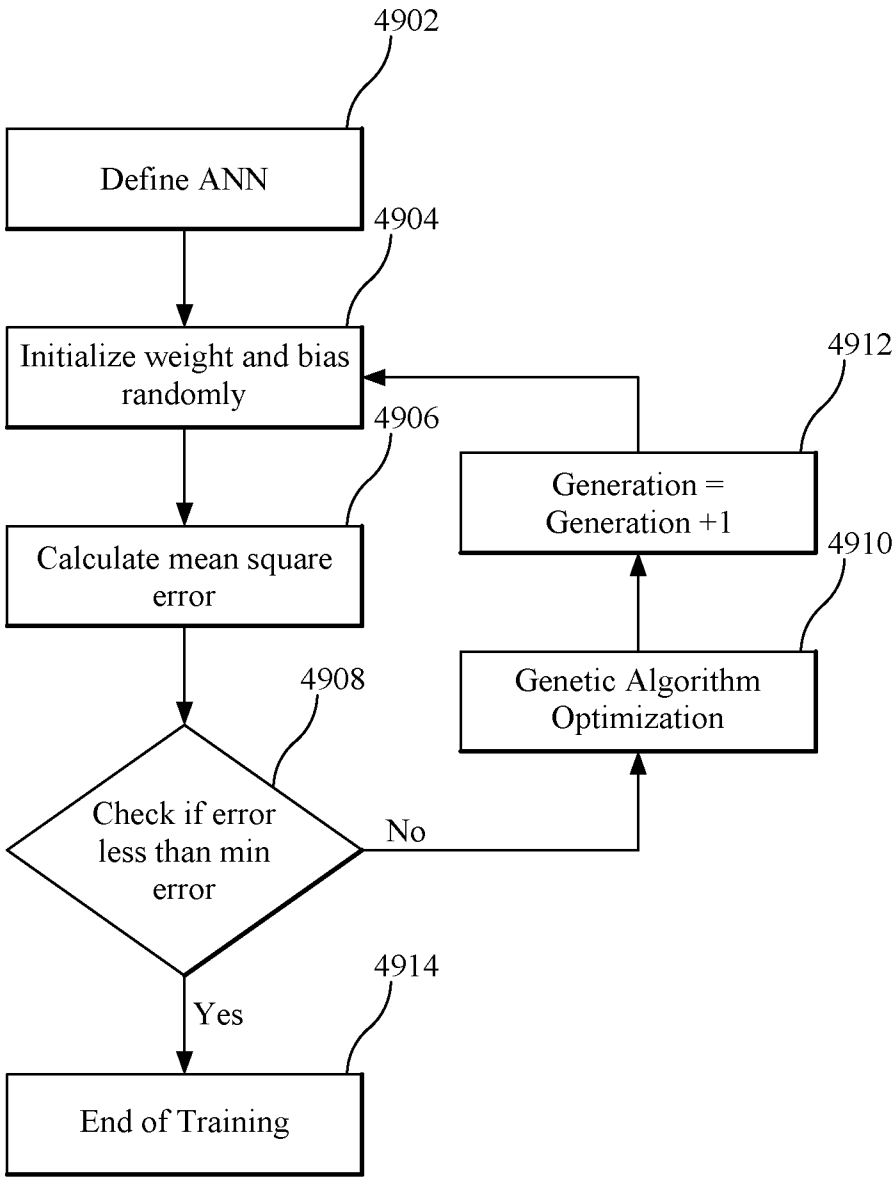

4902
Define ANN
4904
Initialize weight and bias randomly
4906
Calculate mean square error
4908
Check if error less than min error
No
Yes
4910
Genetic Algorithm Optimization
4912
Generation = Generation +1
4914
End of Training

FIGURE 50

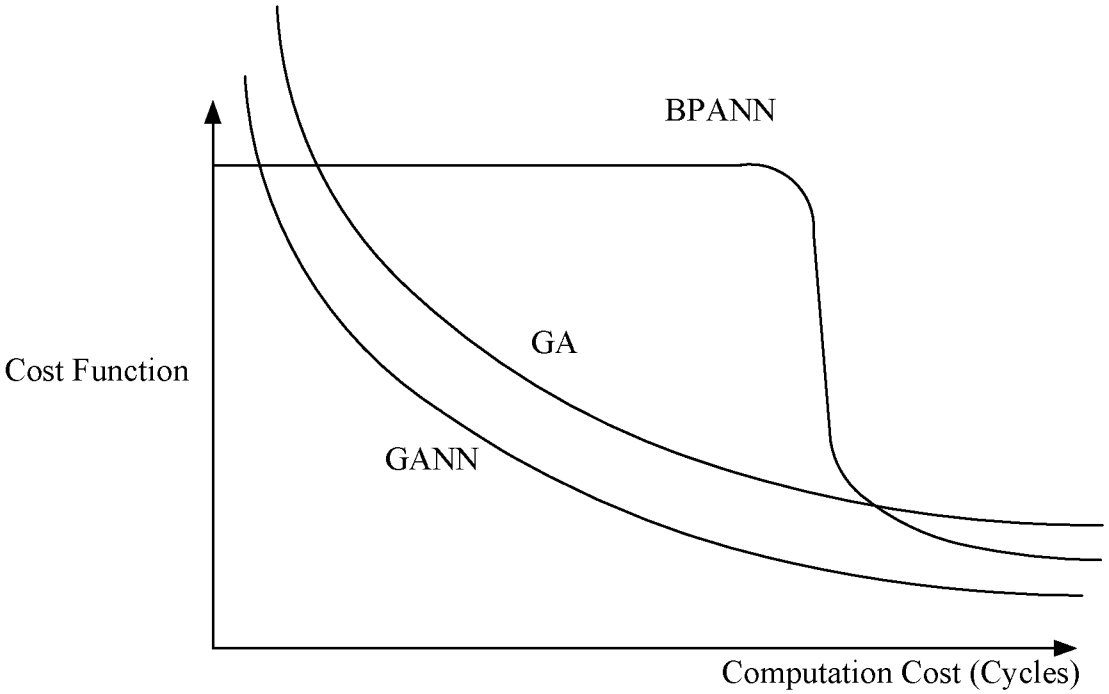


FIGURE 51

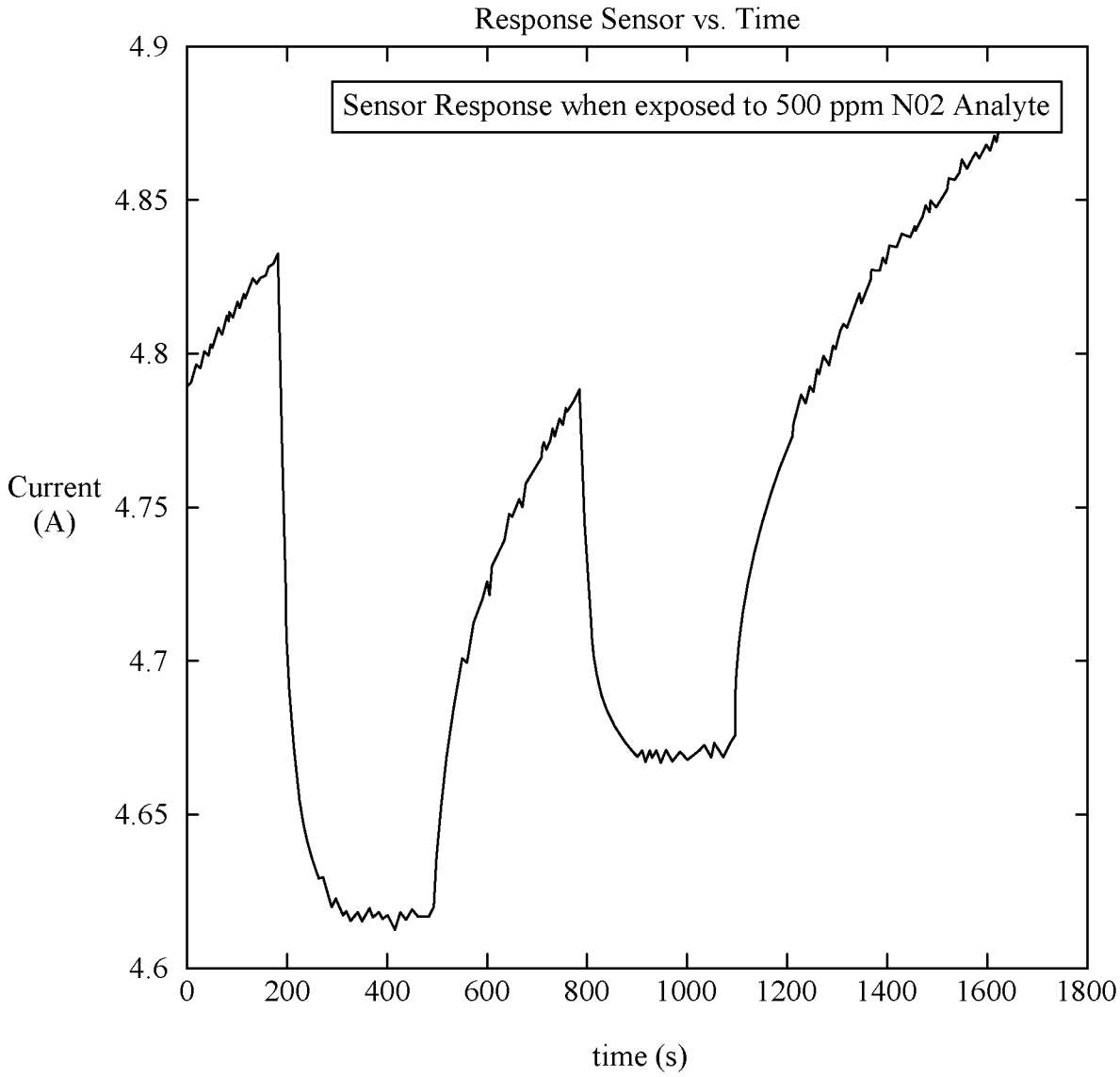

Response Sensor vs. Time
Sensor Response when exposed to 500 ppm N02 Analyte
Current (A)
4.9
4.85
4.8
4.75
4.7
4.65
4.6
0
200
400
600
800
1000
1200
1400
1600
1800
time (s)

FIGURE 52

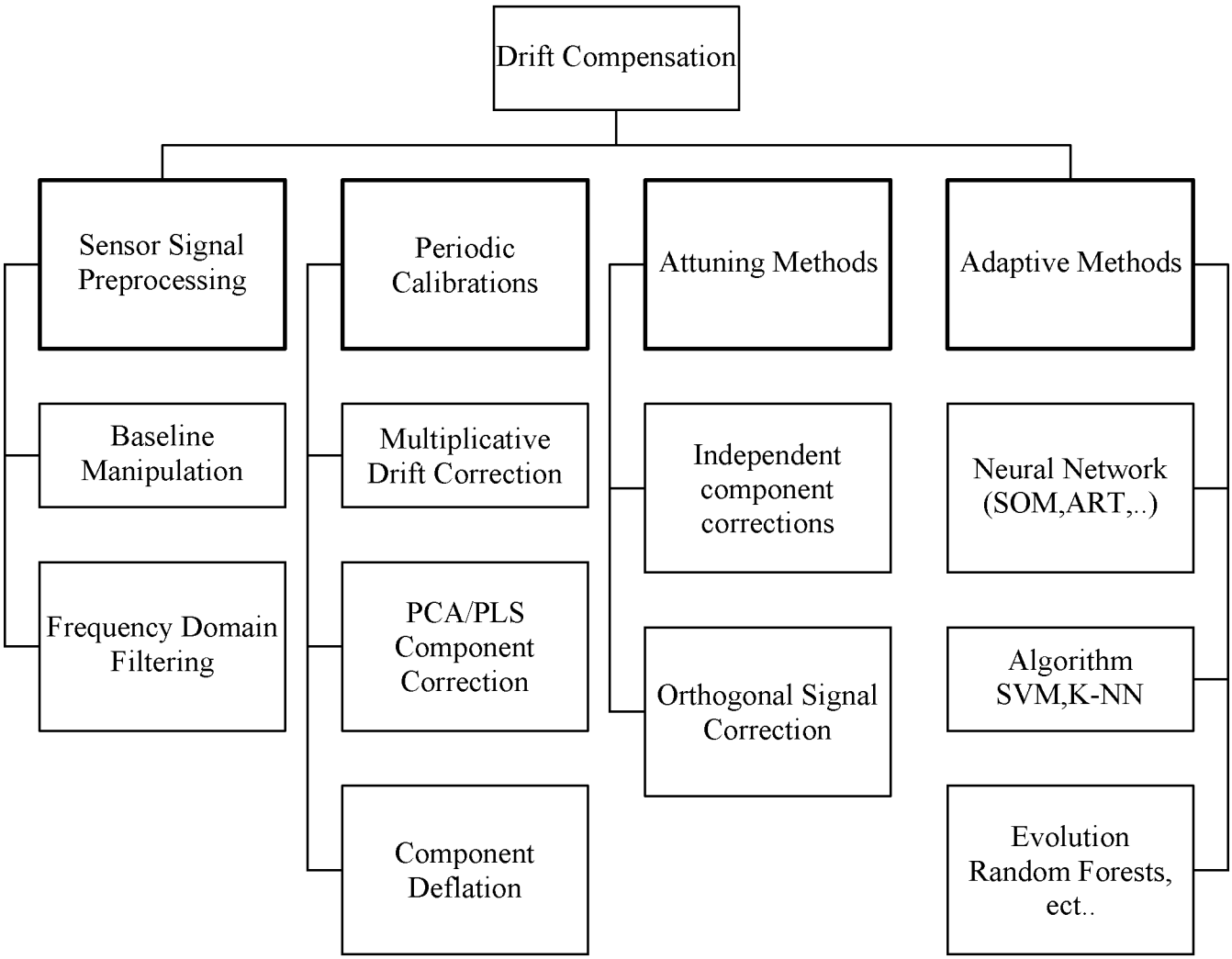

Drift Compensation
Sensor Signal Preprocessing
Periodic Calibrations
Attuning Methods
Adaptive Methods
Baseline Manipulation
Multiplicative Drift Correction
Independent component corrections
Neural Network (SOM,ART,..)
Frequency Domain Filtering
PCA/PLS Component Correction
Orthogonal Signal Correction
Algorithm SVM,K-NN
Component Deflation
Evolution Random Forests, ect..

FIGURE 53

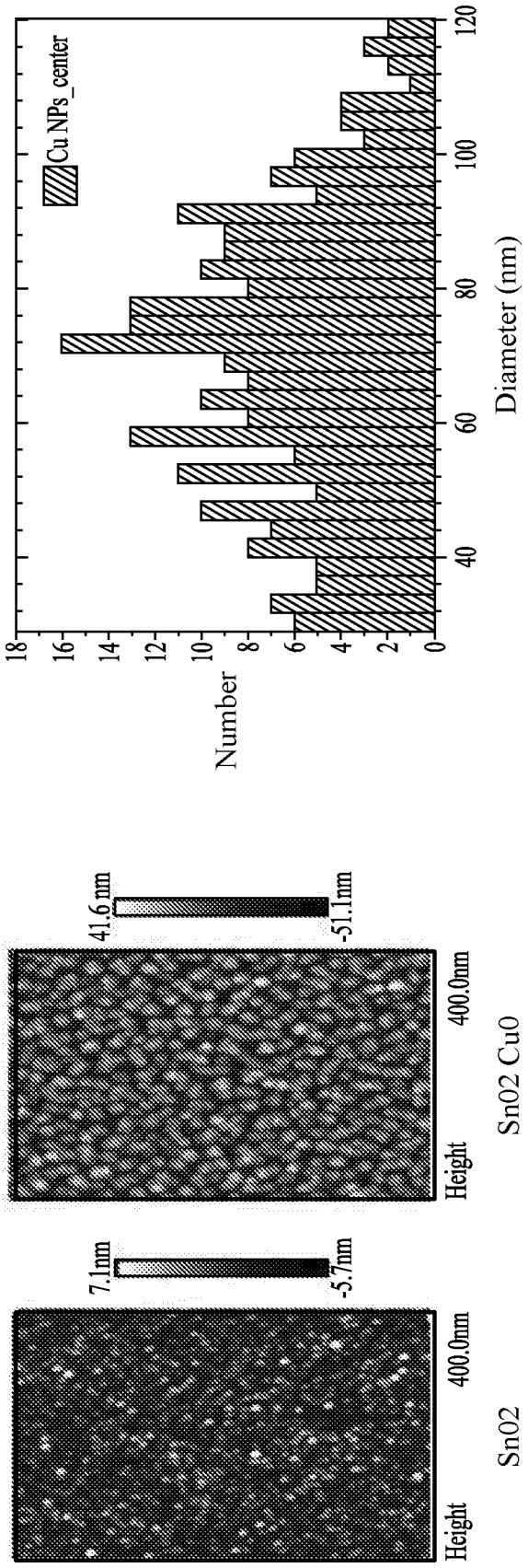

Cu NPs_center
Number
Diameter (nm)
0
2
4
6
8
10
12
14
16
18
40
60
80
100
120
41.6 nm
-51.1nm
Height
400.0nm
Sn02 Cu0
7.1nm
-5.7nm
Height
400.0nm
Sn02

FIGURE 54

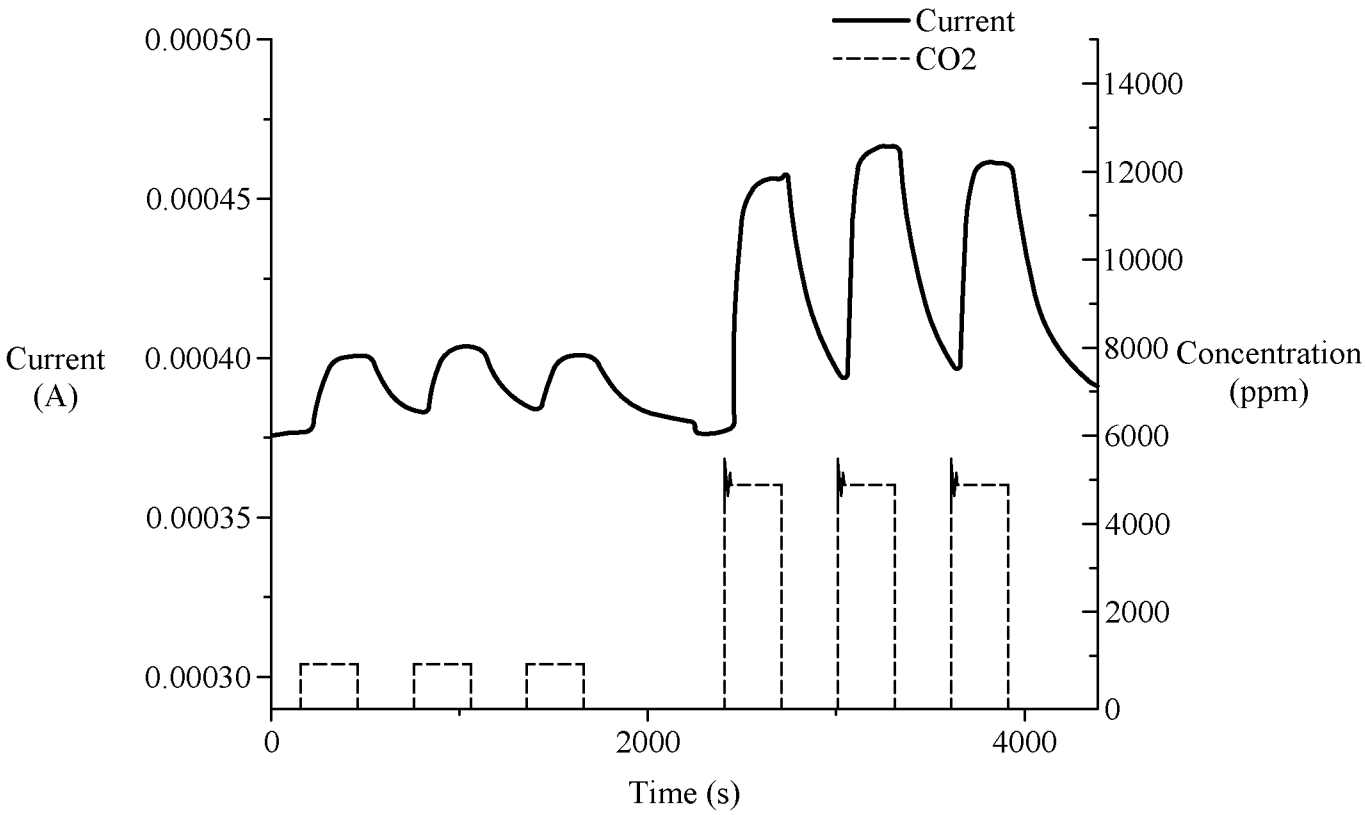
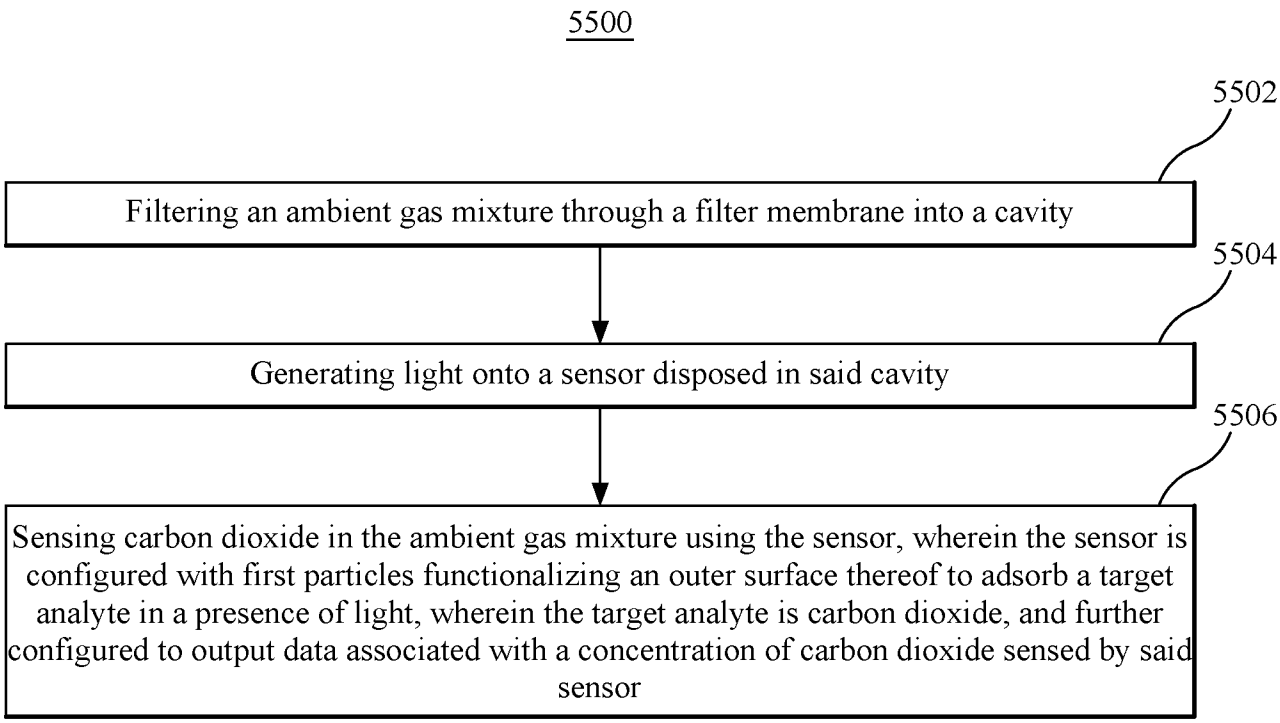

Current
CO2
0.00050
0.00045
0.00040
0.00035
0.00030
Current (A)
14000
12000
10000
8000
6000
4000
2000
0
Concentration (ppm)
0
2000
4000
Time (s)

FIGURE 55


5500
5502
Filtering an ambient gas mixture through a filter membrane into a cavity
5504
Generating light onto a sensor disposed in said cavity
5506
Sensing carbon dioxide in the ambient gas mixture using the sensor, wherein the sensor is configured with first particles functionalizing an outer surface thereof to adsorb a target analyte in a presence of light, wherein the target analyte is carbon dioxide, and further configured to output data associated with a concentration of carbon dioxide sensed by said sensor

INTERNATIONAL SEARCH REPORT

International application No.
PCT/US 19/36335

A. CLASSIFICATION OF SUBJECT MATTER
IPC(8) - G01N 21/33 (2019.01)
CPC - G01N 21/33; G01N 31/223; G01N 33/004

According to International Patent Classification (IPC) or to both national classification and IPC

B. FIELDS SEARCHED

Minimum documentation searched (classification system followed by classification symbols)
See Search History Document

Documentation searched other than minimum documentation to the extent that such documents are included in the fields searched
See Search History Document

Electronic data base consulted during the international search (name of data base and, where practicable, search terms used)
See Search History Document

C. DOCUMENTS CONSIDERED TO BE RELEVANT

Category*	Citation of document, with indication, where appropriate, of the relevant passages	Relevant to claim No.
Y --- A	US 2017/0363594 A1 (CARRIER CORPORATION) 21 December 2017 (21.12.2017) Fig 1, abstract, para [0033]-[0042]	1, 2, 12, 13 --- 3, 4, 14, 15
Y --- A	US 7,186,979 B1 (WONG) 06 March 2007 (06.03.2007) Fig 4, abstract, col 9, ln 33-37	1, 2, 12, 13 --- 3, 4, 14, 15
Y --- A	US 9,851,250 B1 (MAXIM INTEGRATED PRODUCTS, INC.) 26 December 2017 (26.12.2017) Fig 1A, 1B, abstract, col 4, ln 8-col 5, ln 19	1, 2, 13 --- 3, 4, 14, 15
A	US 2017/0038326 A1 (MOTAYED et al.) 09 February 2017 (09.02.2017) Fig 16, abstract, para [0155], [0156]	3, 4, 14, 15
A	US 2006/0257094 A1 (MCEVOY et al.) 16 November 2006 (16.11.2006) Fig 3, abstract, para [0098]-[0100]	3, 4, 14, 15
A	US 2015/0377824 A1 (INFINEON TECHNOLOGIES AG) 31 December 2015 (31.12.2015) Fig 3, abstract, para [0086]	3, 4, 14, 15
A	WO 2017/134247 A1 (FRAUNHOFER-GESELLSCHAFT ZUR FORDERUNG DER ANGEWANDTEN FORSCHUNG E.V.) 10 August 2017 (10.08.2017) Fig 1a, abstract, pg 4, ln 31-pg 5, ln 4	3, 4, 14, 15

☐ Further documents are listed in the continuation of Box C. ☐ See patent family annex.

* Special categories of cited documents:
"A" document defining the general state of the art which is not considered to be of particular relevance
"E" earlier application or patent but published on or after the international filing date
"L" document which may throw doubts on priority claim(s) or which is cited to establish the publication date of another citation or other special reason (as specified)
"O" document referring to an oral disclosure, use, exhibition or other means
"P" document published prior to the international filing date but later than the priority date claimed
"T" later document published after the international filing date or priority date and not in conflict with the application but cited to understand the principle or theory underlying the invention
"X" document of particular relevance; the claimed invention cannot be considered novel or cannot be considered to involve an inventive step when the document is taken alone
"Y" document of particular relevance; the claimed invention cannot be considered to involve an inventive step when the document is combined with one or more other such documents, such combination being obvious to a person skilled in the art
"&" document member of the same patent family

Date of the actual completion of the international search	Date of mailing of the international search report
25 September 2019	14 NOV 2019
Name and mailing address of the ISA/US Mail Stop PCT, Attn: ISA/US, Commissioner for Patents P.O. Box 1450, Alexandria, Virginia 22313-1450 Facsimile No. 571-273-8300	Authorized officer: Lee W. Young PCT Helpdesk: 571-272-4300 PCT OSP: 571-272-7774

INTERNATIONAL SEARCH REPORT

International application No.
PCT/US 19/36335

Box No. II Observations where certain claims were found unsearchable (Continuation of item 2 of first sheet)

This international search report has not been established in respect of certain claims under Article 17(2)(a) for the following reasons:

1. ☐ Claims Nos.:
because they relate to subject matter not required to be searched by this Authority, namely:

2. ☐ Claims Nos.:
because they relate to parts of the international application that do not comply with the prescribed requirements to such an extent that no meaningful international search can be carried out, specifically:

3. ☒ Claims Nos.: 5-11, 16-22, 26
because they are dependent claims and are not drafted in accordance with the second and third sentences of Rule 6.4(a).

Box No. III Observations where unity of invention is lacking (Continuation of item 3 of first sheet)

This International Searching Authority found multiple inventions in this international application, as follows:

This application contains the following inventions or groups of inventions which are not so linked as to form a single general inventive concept under PCT Rule 13.1. In order for all inventions to be searched, the appropriate additional search fees must be paid.

Group I: Claims 1-4 and 12-15 drawn to a sensor package or a method for sensing carbon dioxide gas concentration.

Group II: Claims 23-25 drawn to a carbon dioxide sensor including oxide particles.

--see extra sheet

1. ☐ As all required additional search fees were timely paid by the applicant, this international search report covers all searchable claims.

2. ☐ As all searchable claims could be searched without effort justifying additional fees, this Authority did not invite payment of additional fees.

3. ☐ As only some of the required additional search fees were timely paid by the applicant, this international search report covers only those claims for which fees were paid, specifically claims Nos.:

4. ☒ No required additional search fees were timely paid by the applicant. Consequently, this international search report is restricted to the invention first mentioned in the claims; it is covered by claims Nos.:
1-4, 12-15

Remark on Protest

☐ The additional search fees were accompanied by the applicant's protest and, where applicable, the payment of a protest fee.

☐ The additional search fees were accompanied by the applicant's protest but the applicable protest fee was not paid within the time limit specified in the invitation.

☐ No protest accompanied the payment of additional search fees.

INTERNATIONAL SEARCH REPORT

International application No.
PCT/US 19/36335

Continuation of Box No III -- Observations where unity of invention is lacking

The inventions listed as Groups I and II do not relate to a single general inventive concept under PCT Rule 13.1 because, under PCT Rule 13.2, they lack the same or corresponding special technical features for the following reasons:

Special Technical Features:
Group I includes the special technical features of a filtering membrane and light-based sensing, not included in the other group.

Group II includes the special technical feature of oxide particles include one of: ZnO, In2O3, WO3 or SnO2 particles, not included in the other group.

Common Technical Features:
The only technical features shared by Groups I and II that would otherwise unify the groups, are that they both relate to a carbon dioxide sensor including particles used in sensing. However, this shared technical feature does not represent a contribution over prior art, because the shared technical features is disclosed by US 2015/0377824 A1 to Infineon Technologies AG (hereinafter 'Infineon').

Infineon discloses a carbon dioxide sensor including copper oxide particles deposited on a substrate (Fig 3, abstract, para [0086]).

As the shared technical features were known in the art at the time of the invention, they cannot be considered special technical features that would otherwise unify the groups.

Therefore, Groups I and II lack unity under PCT Rule 13.

Note: Claims 5-11, 16-22, and 26 are determined to be unsearchable because they are dependent claims and are not drafted in accordance with the second and third sentences of Rule 6.4(a) and are, therefore, not included in any claim group.